Wind-Tunnel Investigation of Aerodynamic Efficiency of Three Planar Elliptical Wings With Curvature of Quarter-Chord Line

Raymond E. Mineck
and Paul M. H. W. Vijgen

NASA

Wind-Tunnel Investigation of Aerodynamic Efficiency of Three Planar Elliptical Wings With Curvature of Quarter-Chord Line

Raymond E. Mineck
*Langley Research Center
Hampton, Virginia*

Paul M. H. W. Vijgen
*High Technology Corporation
Hampton, Virginia*

Summary

Three planar, untwisted wings with the same elliptical chord distribution but with different curvatures of the quarter-chord line were tested in the Langley 8-Foot Transonic Pressure Tunnel (8-Ft TPT) and the Langley 7- by 10-Foot High-Speed Tunnel (7 × 10 HST). The different curvatures yielded a wing with an unswept quarter-chord line, a wing with an unswept trailing edge, and a wing with an unswept 150-percent chord (with a crescent-shaped planform). A fourth wing with a rectangular planform and the same planform area and span as the elliptical-chord-distribution wings was also tested with two tip shapes. Force and moment measurements from the 8-Ft TPT tests are presented for Mach numbers from 0.3 to 0.5 and angles of attack from $-4°$ to $7°$ for chord Reynolds numbers of 1.5×10^6 and 2.1×10^6. Sketches of the oil-flow patterns on the upper surfaces of the wings and some force and moment measurements from the 7 × 10 HST tests are presented at a Mach number of 0.5. The aerodynamic efficiency of the wings is evaluated by the lift-curve slope, the Oswald efficiency factor, and a cambered-wing efficiency factor.

Fixing the boundary-layer transition near the leading edge of a wing that uses an airfoil designed for extensive laminar flow increases the drag coefficient at zero lift and thickens the boundary layer. The thickened boundary layer decreases the effective camber of the airfoil which leads to a less-negative angle of zero lift. The reduction in the lift-curve slope and the reduction in the Oswald efficiency factor with the fixed transition indicate that the wing with the more extensive laminar boundary layer is more efficient. Increasing the Reynolds number decreases the drag coefficient at zero lift. Increases in the lift-curve slope and the Oswald efficiency factor with increasing Reynolds number indicate that the wing with the thinner boundary layer is more efficient.

Increasing the curvature of the quarter-chord line makes the angle of zero lift more negative but has little effect on the drag coefficient at zero lift. The changes in lift-curve slope and in the Oswald and cambered-wing efficiency factors with the change in curvature of the quarter-chord line (wingtip location) indicate that the elliptical wing with the unswept quarter-chord line has the lowest lifting efficiency and the elliptical wing with the unswept trailing edge has the highest lifting efficiency; the crescent-shaped-planform wing has an efficiency in between.

Flow visualization results indicate that for lifting conditions, the flow near the tip on the upper surface of the elliptical wing with the unswept quarter-chord line is swept inboard. The flow near the tip of the elliptical wing with unswept trailing edge moves streamwise at the lower angles of attack and slightly outboard at the higher angle of attack. Flow near the tip of the crescent wing is swept outboard with a significant separated flow region at the trailing edge of the tip. The flow at the tip of the elliptical wing with the straight trailing-edge and the flow at the tip of the crescent-shaped wing are probably influenced by a vortex originating at the highly swept leading edges.

Introduction

Induced drag or drag due to lift constitutes approximately one-third of the total drag of conventional subsonic transport aircraft in cruising flight and as much as one-half of the total drag in climbing flight (ref. 1). For future aircraft with possible substantial amounts of laminar flow and reduced skin-friction drag, the relative contribution of induced drag will increase. In view of this possibility, methods to decrease induced drag for given total lift require renewed attention.

Induced drag arises from rotational energy shed as vorticity into the wake of a finite-span lifting wing. The trailing vorticity induces a downwash that changes the local flow field at the wing, and this results in a component of the total force on the wing in the drag direction. Approximating the wing by a bound vortex and assuming a planar, rigid wake (parallel to the free-stream direction), Munk showed in reference 2 that induced drag for a given lift is at a minimum when the downwash is constant across the span of the wing. An elliptical circulation distribution produces a constant downwash and, according to the classical linear theory, has minimum induced drag. Also based on the linear lifting-line assumptions, Munk's stagger theorem states that induced drag does not change if a specified total circulation is redistributed in the streamwise direction.

Following the aforementioned assumptions of classical lifting-line theory, Cone showed in reference 3 that displacing the circulation distribution in the vertical direction theoretically offers large reductions in induced drag for a given total lift if an optimum circulation distribution is satisfied. The resulting concept of tip-mounted winglets, described in reference 4, has found application on some business jets and subsonic commercial transports. Reductions in drag due to lift by the addition of winglets can be as high as 10 to 20 percent, depending on the baseline configuration. (See ref. 5.) The potential induced drag benefits of winglets may be offset by

increased structural complexity, increased weight, increased skin-friction drag from the increased wetted area, and adverse viscous and compressibility interference effects.

Following Munk's stagger theorem, inplane curvature of the quarter-chord line does not affect the minimum induced drag once an elliptical chord distribution has been assumed to generate an elliptical loading. As exemplified in reference 6 (fig. 11.4, p. 201), the definition of a planform shape with an elliptical chord distribution is not unique. Using linear theory, Burkett in reference 7 and Lowson in reference 8 indicated that a wing with a swept (or curved) quarter-chord line placed at an angle of attack shows a reduction in induced drag because of a vertical displacement of the outboard portion of the wing. Using the approach outlined by Cone, a maximum reduction in induced drag of 3 to 4 percent is predicted in reference 7 for an optimum circulation distribution and large angles of attack. To generate a given lift, a larger angle of attack is required for a wing with a symmetrical airfoil section than for a wing with a cambered airfoil section. For a wing with a swept (or curved) quarter-chord line, the larger angle of attack associated with the symmetrical airfoil section leads to a larger vertical displacement of the outboard portion of the wing. Thus, the generation of lift through angle of attack using an uncambered (symmetrical) airfoil section may have a small, but essential, induced-drag advantage over a similar wing using a cambered airfoil section.

The vortex wake shed by a wing does not remain planar (rigid), as assumed by Munk, but deforms (relaxes) as it rolls up into the trailing wingtip vortices. Potential-flow computational methods have been developed that approximate the trailing-wake deformation. Drag predictions by surface-panel methods that allow an approximate relaxation of the trailing wake have indicated a reduction in induced drag for aft-swept and crescent-shaped elliptical planforms in comparison with those of the unswept elliptical wing (refs. 9 to 11). To the limit of discretization investigated, a reduction of 2 to 3 percent in induced drag is predicted for the crescent-shaped wing with an aspect ratio of 7 and a symmetrical airfoil (refs. 10 and 11). Wake relaxation reduced the Oswald efficiency factor more for the unswept wing than for the crescent wing (ref. 11). The efficiency computed for a given planform with the relaxed wake is less than the computed efficiency with the rigid-wake assumption of Munk. From the inviscid calculations with wake relaxation, the spanloading near the tip of the crescent wing appears to be greater than the spanloading near the tip of the unswept elliptical wing (refs. 10

and 11). This increased loading near the tip can better approximate an elliptical loading. Obviously, a true elliptical load distribution is an unreachable goal since the vorticity shed at the tip approaches an infinite value. Currently, work is underway to analyze the inviscid characteristics of curved elliptical planforms using Euler methods (refs. 12 and 13). Because the wake shape and location are obtained as an inherent part of the Euler solution, the need for approximating the shape of the trailing vortex wake in potential-flow methods using wake relaxation is eliminated. Available results from reference 13 indicate a 3-percent improvement in the lifting efficiency for the crescent-shaped planform.

Low-speed wind-tunnel experiments to investigate the effect of inplane modifications on the drag due to lift have been reported in the literature (e.g., ref. 14). Tests of two untwisted wings with an aspect ratio (A) of 7 with the same elliptical chord distributions, one with an unswept quarter-chord line and the other with a crescent-shaped planform, indicated an improvement in the Oswald efficiency factor of approximately 3 percent for the crescent planform at lift coefficients below 0.5 (ref. 15). The streamwise airfoil shape was the uncambered NACA 0012 section, with boundary-layer transition fixed near the leading edge. No significant flow separation occurred for lift coefficients below 0.5 for the two planforms. The maximum lift coefficient of the crescent wing was 8 percent greater than that of the unswept wing (ref. 16). An analysis of the error propagation of this experiment in a large subsonic wind tunnel indicated that the absolute uncertainty in drag is the same order as the measured improvements because of the planform shape (ref. 15). The accuracy in the angle-of-attack measurement in these experiments appeared critical for accurate induced-drag measurements, a fact also noted by others (e.g., ref. 17).

Classical, linear wing theory indicates that an elliptical span load distribution produces the minimum induced drag. Ignoring viscous effects and wake deformation, an untwisted wing with an elliptical spanwise variation of the chord has an elliptical span load distribution. Inviscid calculations with a relaxed wake indicate that increasing the curvature of the quarter-chord line will reduce the induced drag. Previous wind-tunnel experiments of two elliptical planform wings with different curvatures of the quarter-chord line (ref. 15) indicate that an induced-drag reduction occurs when the curvature of the quarter-chord line is increased. However, the uncertainty in those experimental measurements suggested that additional wind-tunnel experiments on similar wing shapes are needed with reduced

measurement uncertainty to determine if the induced-drag reduction predicted by the inviscid calculations occurs in a viscous flow.

This report presents the results from experiments designed to study the induced drag of planar, elliptical planform wings with each having a different curvature of the quarter-chord line. The measurement uncertainty was reduced to allow the small differences in the drag to be determined accurately. A cambered airfoil section was selected to provide a larger range of positive lift coefficients without any significant flow separation. An $A = 6$ wing was chosen to produce larger changes in induced drag compared with experimental results reported in reference 15. Four wings were tested in two wind tunnels. Three wings had the same elliptical, spanwise chord distributions but different curvatures of the quarter-chord line. The fourth wing had a rectangular planform with the same area and span as the three elliptical wings.

The purposes of the present investigation are as follows: (1) to study the lift and drag characteristics of elliptical chord wings with an increasing degree of curvature of the quarter-chord line and with a cambered streamwise airfoil section, (2) to determine the effect of transition location on the lift-dependent drag characteristics of the wings using a natural-laminar-flow airfoil, and (3) to assess the achievable accuracy and repeatability of induced-drag measurements using internal-force balances at medium subsonic speeds (at free-stream Mach numbers from 0.3 to 0.5) in a large transonic wind tunnel.

The wings were first tested in the Langley 8-Foot Transonic Pressure Tunnel (8-Ft TPT). Force and moment results are presented at Mach numbers of 0.3, 0.4, and 0.5 and angles of attack from about $-4°$ to $7°$. The Reynolds numbers were 1.5×10^6 and 2.1×10^6, based on the wing reference chord. The wings were subsequently tested in the Langley 7- by 10-Foot High-Speed Tunnel (7 × 10 HST) to obtain surface flow visualization photographs and to obtain tunnel-to-tunnel repeatability data. The Reynolds number varied from 1.3×10^6 to 1.9×10^6 as the Mach number varied from 0.3 to 0.5 because the 7 × 10 HST is an atmospheric tunnel. The flow visualization tests covered the same Mach number and angle-of-attack ranges.

Symbols

The longitudinal aerodynamic characteristics are presented in the stability-axes system. Results are presented in coefficient form with the model moment reference center at the quarter-chord location of the wing root. All measurements and calculations were made in the U.S. customary units, and dimensional results are presented in the U.S. customary units.

A	wing aspect ratio, $\frac{b^2}{S}$
b	wing reference span (48.00 in.)
C_D	drag coefficient, $\frac{\text{Drag}}{q_\infty S}$
$C_{D,\min}$	minimum drag coefficient
$C_{D,\min}^*$	minimum profile drag coefficient
$C_{D,0}$	drag coefficient at zero lift
C_L	lift coefficient, $\frac{\text{Lift}}{q_\infty S}$
$C_{L,\min}$	lift coefficient at minimum drag coefficient
$C_{L,\min}^*$	lift coefficient at minimum profile drag coefficient
C_{L_α}	lift-curve slope, $\deg^{-1}$
C_m	pitching-moment coefficient about wing-root quarter-chord location, $\frac{\text{Moment}}{q_\infty S \bar{c}}$
c	local chord, in.
c_{root}	wing chord at model centerline, in.
$\bar{c}$	wing reference chord (8.00 in.), $\frac{S}{b}$
D	drag, lb
e	Oswald efficiency factor, $\left(\pi A \frac{dC_D}{dC_L^2}\right)^{-1}$
e^*	cambered-wing efficiency factor, $\left[\pi A \frac{dC_D}{d(C_L - C_{L,\min})^2}\right]^{-1}$
K_i	inviscid induced-drag factor (see eq. (8))
K_p	viscous induced-drag factor (see eq. (8))
L	lift, lb
l	length of nose section (6.00 in.)
M_∞	free-stream Mach number
q_∞	free-stream dynamic pressure, psi
R_c	free-stream Reynolds number based on model reference chord
R_s	free-stream Reynolds number based on chordwise distance along surface
R_θ	local Reynolds number based on boundary-layer momentum thickness

r_l	local body radius, in.
r_{max}	maximum body radius (1.50 in.)
S	wing planform reference area (384.00 in^2)
x	streamwise distance from wing-root leading edge, in.
x_{le}	streamwise distance from wing-root leading edge to local leading edge, in.
x_{tip}	streamwise distance from wing-root leading edge to wingtip, in.
y	spanwise position, in.
z	normal position, in.
α	geometric angle of attack, deg
α_0	angle of attack at zero lift, deg
η	position on semispan, $\frac{y}{b/2}$

Abbreviations:

diam.	diameter
rms	root mean square
Sta.	station

Wind Tunnels

The Langley 8-Foot Transonic Pressure Tunnel

The majority of the experiments were conducted in the Langley 8-Foot Transonic Pressure Tunnel (8-Ft TPT). Information about this tunnel may be found in reference 18. The tunnel is a single-return, fan-driven, continuous-operation pressure tunnel. The test section is 160 in. long with an 85.5-in-square cross section and corner fillets. The top and bottom walls have four longitudinal slots yielding a porosity of about 5 percent, and the sidewalls are solid. The empty test section Mach number is continuously variable from about 0.20 to 1.30. Stagnation pressure can be varied from 0.25 to 2.00 atm. Air dryers are used to control the dew point. A heat exchanger located upstream of the settling chamber controls the stagnation temperature. The test section contraction ratio is 20.25:1, and there are five turbulence-reduction screens. An arc-sector model support system is located in the high-speed diffuser. The angle range of the arc sector is from $-12.5°$ to $12.5°$. The whole arc sector can be translated longitudinally to position the model at the desired test section station for testing.

The Langley 7- by 10-Foot High-Speed Tunnel

Flow visualization and tunnel-to-tunnel data repeatability studies were performed in the Langley 7- by 10-Foot High Speed Tunnel (7 × 10 HST). A general description of the tunnel and its support equipment is found in reference 19. It is a single-return, closed-circuit, fan-driven wind tunnel, and it operates at ambient temperature and pressure. Test section walls are solid with no divergence. Streamwise fairings on the sidewalls modify the cross-sectional area distribution to provide a uniform longitudinal Mach number distribution along the centerline of the test section. The test section is 6.58 ft high by 9.57 ft wide with a useable length of 10.83 ft. A variable-speed drive motor provides a continuous Mach number range from near 0 to 0.94. The contraction ratio is 17:1 and there are four turbulence-reduction screens. The model support system consists of a vertical strut and a variable-pitch-angle sting support system with a range from $-12°$ to $12°$. The sting support system can be translated on the vertical strut to position the model close to the test section centerline.

Models

Four wing-body models were tested. Each model consisted of a common forebody, a wing with an integral centerbody, and a common aftbody. One wing had a rectangular planform and an 8.00-in. chord. The other three wings had the same elliptical spanwise variation of chord. The physical characteristics of the wings are listed in table 1. Photographs of one of the models installed in the 8-Ft TPT are presented in figure 1. A sketch of the model with one of the wings is presented in figure 2(a). All elliptical planform wings had a span of 48.00 in. and a projected area of 384.00 in^2, which yielded a common aspect ratio of 6.00. Each wing was untwisted.

The NASA NLF(1)-0416 airfoil section was used for all four wings. This cambered airfoil is 16 percent thick and is designed for a lift coefficient of 0.4 at a Reynolds number of 4×10^6. Details of the airfoil characteristics are presented in reference 20, and the airfoil coordinates are listed in table 2. A sketch of the airfoil section is found in figure 2(b). The airfoil chord coincided with the centerline of the body. The quarter-chord location of the wing root was located 10.00 in. aft of the beginning of the forebody for all four wings.

The model forebody was 6.30 in. long with the rearmost 0.30 in. at a constant diameter of 3.00 in.

4

The forward 6.00 in. was defined by the polynomial

$$\frac{r_l}{r_{\max}} = \left[3\left(\frac{x}{l}\right) - 3\left(\frac{x}{l}\right)^2 + \left(\frac{x}{l}\right)^3\right]^{1/2} \quad (1)$$

A sketch of the model forebody is presented in figure 2(c), and the coordinates are listed in table 3. The integral centerbody was 12.70 in. long with a diameter of 3.00 in. The model aftbody was a straight cylinder with a diameter of 3.00 in. and a length of 9.00 in. The internal diameter at the downstream end of the aftbody was 2.90 in.

The three elliptical wings have the same spanwise variation of chord but different planforms because of different curvatures of the quarter-chord line. The chord at the model centerline on each of the elliptical wings was 10.19 in. The spanwise distribution of the local chord was elliptical and was determined from the chord at the model centerline (c_{root}) and the model span (b). Thus,

$$c = c_{\text{root}}\sqrt{1 - \left(\frac{y}{b/2}\right)^2} = c_{\text{root}}\sqrt{1 - \eta^2} \quad (2)$$

The planform view of the leading-edge shape was also chosen to be elliptical:

$$x_{le} = x_{\text{tip}}\left[1 - \sqrt{1 - \left(\frac{y}{b/2}\right)^2}\right] = x_{\text{tip}}\left(1 - \sqrt{1 - \eta^2}\right) \quad (3)$$

The streamwise position of a point relative to the wing-root leading edge (x) on the wing at a specified fraction of the local chord ($(x/c)_{\text{local}}$) is obtained from equations (2) and (3) as follows:

$$
\begin{aligned}
x(\eta) &= x_{le}(\eta) + \left(\frac{x}{c}\right)_{\text{local}} c(\eta) \\
&= x_{\text{tip}}\left(1 - \sqrt{1 - \eta^2}\right) + \left(\frac{x}{c}\right)_{\text{local}} c_{\text{root}}\sqrt{1 - \eta^2} \\
&= c_{\text{root}}\left\{\left[\left(\frac{x}{c}\right)_{\text{local}} - \frac{x_{\text{tip}}}{c_{\text{root}}}\right]\sqrt{1 - \eta^2} + \frac{x_{\text{tip}}}{c_{\text{root}}}\right\} \quad (4)
\end{aligned}
$$

The streamwise position of a point ($x(\eta)$) at a constant nondimensional chordwise position ($(x/c)_{\text{local}}$) at a spanwise station (η) is determined by the nondimensional location of the wingtip ($x_{\text{tip}}/c_{\text{root}}$). Therefore, assuming the above expressions for the elliptical distributions for the chord and for the leading edge, the elliptical wing planform shape is determined by the nondimensional location of the wingtip. Equation (4) can be used to determine the line defined by a constant fraction of the local chord, such as the quarter-chord line. Note that $x(\eta)$ is a constant (equal to x_{tip}) if the selected fraction of the local chord ($(x/c)_{\text{local}}$) is equal to the nondimensional location of the wingtip ($x_{\text{tip}}/c_{\text{root}}$). For this case, the curve defining the constant fraction of the local chord is a straight line in the spanwise direction passing through the tip.

The three nondimensional locations selected for the wingtip ($x_{\text{tip}}/c_{\text{root}}$) for this study were 0.25, 1.00, and 1.50. Sketches of the three elliptical wings are presented in figure 3. The wing with the nondimensional wingtip location of 0.25 has an unswept quarter-chord line and will be referred to as *wing A*. The wing with the nondimensional wingtip location of 1.00 has an unswept trailing edge and will be referred to as *wing B*. The wing with the nondimensional wingtip location of 1.50 has a crescent-shaped planform and will be referred to as *wing C*. The curvature of the quarter-chord line increases as the nondimensional tip location increases from 0.25 to 1.50.

A fourth wing was tested as a baseline planform. This wing, referred to as *wing D*, had a rectangular planform. A comparison of wings A and D is presented in figure 4. Wing D had two sets of interchangeable tips. The wing with the square tip had the same span, area, and aspect ratio as the elliptical planform wings. The wing with the round tip had a span of 49.28 in. and a projected area of 390.34 in². The resulting aspect ratio was 6.22. The rounded end of the tip was formed by revolving one-half of the airfoil section local thickness about the camber line. A sketch of the round tip superimposed on the square tip is presented in figure 5. Photographs of the rectangular wing with the square tips and with the rounded tips are shown in figure 6. A brief summary of the four wings is presented in chart A.

Chart A

Wing	Nondimensional wingtip location, $x_{\text{tip}}/c_{\text{root}}$	Description
A	0.25	Unswept quarter-chord line (elliptical chord distribution)
B	1.00	Unswept trailing edge (elliptical chord distribution)
C	1.50	Crescent-shaped planform (elliptical chord distribution)
D	N/A	Rectangular planform (round tip and square tip)

Instrumentation

The models were mounted on a six-component strain gauge balance supported by a straight sting as shown in figure 7. The sting was mounted directly to the model support system without any knuckles so that the model support system and the sting were aligned. This sting was used in both wind-tunnel tests. Different strain gauge balances were selected for each tunnel test to match the maximum airload on the model with the balance maximum load capacity. The measurement accuracy for each component of the strain gauge balance was determined from the calibration of the balance for the load ranges encountered in the test. For the 8-Ft TPT test, the measurement accuracies for the components of the strain gauge balance were ± 0.1 percent of the full-scale load for normal force and pitching moment and less than ± 0.3 percent of the full-scale load for axial force. These accuracies correspond to ± 0.70 lbf for normal force, ± 0.25 lbf for axial force, and ± 2.00 in-lbf for pitching moment.

To measure the model angle of attack, an accelerometer was installed inside the nose of the forebody and attached to the front surface of the balance mounting block that was common to all models. The static calibration of the accelerometer was accurate to within $\pm 0.01°$ over the range of angles of attack presented in this report. Two tubes were installed on the left and right sides of the sting extending into the aftbody to measure the chamber pressure within the model for use in computing the correction to axial force (and drag) to a condition of free-stream static pressure at the base of the model. Free-stream total and static pressures were measured with sonar mercury manometers. The accuracy of the sonar manometers was ± 0.3 psf.

Uncertainties (U) in the Mach number, lift coefficient, and drag coefficient for the test in the 8-Ft TPT are derived in the appendix. The uncertainties in the Mach number were computed at nominal values of the free-stream total and static pressures. The Mach number uncertainty was typically about ± 0.0003. The uncertainties in the lift and drag coefficients were determined for measured model loads over a range of angles of attack from $-3°$ to $3°$ because results over this range will be used to compare the efficiencies of the different wings. As expected, the uncertainties were largest at the lowest Mach number and Reynolds number where the air loads were smallest. The uncertainty became smaller as the Mach number and/or Reynolds number increased. For these small angles of attack, the accuracy of the normal-force measurement had the strongest influence on the uncertainty of the lift co-

efficient. The accuracy of the axial force and, to a lesser degree, the accuracy of the angle-of-attack measurement had the strongest influence on the uncertainty of the drag coefficient. At a Mach number of 0.5, the uncertainty in the lift coefficient was about ± 0.0009 and the uncertainty in the drag coefficient was about ± 0.0003.

Boundary-Layer Transition Strips

Changes in the location of the boundary-layer transition from laminar to turbulent flow will change the boundary-layer thickness and the viscous drag. The chordwise location of transition depends on the Reynolds number and the pressure distribution, which is a function of the angle of attack. The transition location also depends on the leading-edge sweep angle because of the crossflow and attachment-line instabilities, and hence the location will probably be different for each elliptical-planform wing model.

If the transition location changes with lift, the viscous drag and total drag will also change. Also, at the low Reynolds numbers near the tip of the elliptical planform wings, nonreattaching laminar-separation bubbles may occur. These effects complicate the analysis of the results. To minimize these effects, the location of the boundary-layer transition was fixed by applying strips of carborundum grit to the model surface. For all tests, a ring of transition grit (0.06 in. wide) was placed on the forebody at a location 0.75 in. back along the surface. For the transition-fixed tests, strips of transition grit were placed on both the upper and lower surfaces of the wing, as shown in figure 8. A constant chordwise location was selected because that is a requirement of many Computational Fluid Dynamics (CFD) codes. The $0.075c$ position was selected for the transition strips on the wing. The grit size was determined by using the essentially two-dimensional methods of Braslow and Knox in reference 21 for $R_c = 2.1 \times 10^6$, $M_\infty = 0.5$, and a free-stream Reynolds number of 600, based on a reference length equal to the grit height.

Sketches showing this baseline grit installation, used on wings A and C, are found in the upper part of figures 8(a) and 8(c). In the tip region of the elliptical wings, the most forward transition-grit location that does not violate the criterion that $R_s > 0.1 \times 10^6$ is aft of the $0.075c$ location selected. Large grit sizes, with associated nonnegligible grit drag and changes in local flow field, are necessary to promote transition for $R_s \ll 0.1 \times 10^6$ (refs. 22 and 23). The baseline grit installation maintained the $0.075c$ trip location all the way out to the wingtip. Using the sublimating-chemical, transition

visualization technique, the effectiveness of the trip was studied on wing A at $\alpha = -0.25°$, $M_\infty = 0.3$, and $R_c = 2.1 \times 10^6$. The trip strip was effective at tripping the boundary layer across the span of the wing except for the tip region. Uncertainty about the effectiveness of the trip near the wingtip led to a modification of the grit size and location in the outboard region in later phases of the experiment.

Sketches showing the modified grit installation are found in figure 8. For wings A and B, from $\eta = 0.96$ to the tip, grit was installed in a straight line. For wing C, the grit was installed in a straight line from $\eta = 0.94$ to the tip because of the larger local leading-edge sweep angle. Larger values of R_s are realized by the modification, but the chordwise grit location is no longer at a constant fraction of the local chord. A comparison of the lift and drag characteristics of wing A and wing C for the two trip locations, presented in figures 9 and 10, respectively, shows no noticeable differences in the lift and pitching-moment coefficients. The drag coefficient at a given lift coefficient for the modified grit location is slightly less than that for the baseline grit location.

Variations in spanwise and chordwise locations of transition among the wings due to the increasing degree of leading-edge sweep can result in variations in viscous drag among the wings as the angle of attack is varied. Attachment-line transition as well as crossflow instability can occur in regions where the leading-edge sweep is sufficiently large. These possible viscous drag variations among the wings can be improperly interpreted as differences in inviscid lift-dependent drag. In an attempt to further reduce the variation in transition location in the leading-edge region, a trip strip was installed in a direction normal to the leading edge on wings B and C. The strip extended back to the constant-chord grit strips on both surfaces.

A similar trip, which was also installed in the experiments made by Van Dam, Vijgen, and Holmes, was reported in reference 15. The spanwise location of this trip was chosen to coincide with a predicted attachment line at $R_\theta = 100$. If R_θ exceeds 100, the boundary layer along the attachment line will remain turbulent when a large trip is present (ref. 24). Using the dimensional leading-edge radius in the normal direction and the leading-edge sweep angle as a function of spanwise location, R_θ was estimated for a given free-stream Reynolds number by assuming an infinite swept-wing geometry and the stagnation line on the leading edge (ref. 25). Only wings B and C had sufficient leading-edge sweep to yield a value of R_θ of 100 at the Reynolds numbers used in this test; therefore, wing A did not have a leading-edge trip. The

leading-edge trip for wing B was located at $\eta = 0.90$, as shown in figure 8(b), and the leading-edge trip for wing C was located at $\eta = 0.75$, as shown in figure 8(c).

Tests and Procedures

The model was tested in the Langley 8-Foot Transonic Pressure Tunnel at Reynolds numbers of 1.5×10^6 and 2.1×10^6, based on the wing reference chord. Tests at the lower Reynolds number were conducted at $M_\infty = 0.3$, and tests at the higher Reynolds number were conducted at $M_\infty = 0.3, 0.4$, and 0.5. The angle of attack was varied from $-4°$ up to $7°$. At an angle of attack of $0°$, the nose of the model was located on the test section centerline 80 in. downstream from the start of the test section so that the model was located approximately in the middle of the useable portion of the test section. Because the center of rotation of the model support system was near the base of the sting, the model location moved slightly downstream and upward as the angle of attack was increased from $0°$. To minimize any aerodynamic hysteresis effects, all angles of attack were approached from below the desired angle. All four wings were tested with fixed transition. Only wing A was tested with free transition.

Tests of wings A and C in an upright and inverted orientation led to an average downwash of $0.037°$ for this model location and these planforms. The angularity was constant for the ranges of angles of attack and Mach numbers considered herein. This correction was applied to all the results from the 8-Ft TPT. The two model chamber pressures were averaged and used to correct the balance axial force (and drag) for the pressure at the open end of the aftbody. No corrections were applied for model blockage or jet boundary effects.

The model was subsequently tested in the 7 × 10 HST on the same sting that was used for the tests in the 8-Ft TPT. A smaller capacity balance was used for these tests because the dynamic pressure and, consequently, the airloads were reduced in the 7 × 10 HST. The models were tested at $M_\infty = 0.3, 0.4$, and 0.5 over the same angle-of-attack range. The Reynolds number varied from 1.3×10^6 to 1.9×10^6 as the Mach number varied from 0.3 to 0.5. The same test procedures were used to minimize aerodynamic hysteresis effects. Surface oil-flow visualization photographs were taken at several angles of attack on each wing at Mach numbers of 0.3 and 0.5. All tests in the 7 × 10 HST were conducted with the modified grit configurations.

Tests of wings A and D in an upright and inverted orientation led to an average downwash for these planforms at this model location that varied slightly with Mach number. The flow-angularity corrections at $M_\infty = 0.3, 0.4,$ and 0.5 were $0.025°$, $0.040°$, and $0.040°$, respectively. This correction was applied to all the results from the 7 × 10 HST. The model chamber pressures were averaged and used to correct the balance axial force (and drag) for the pressure at the open end of the aftbody. Corrections were applied for model blockage and jet boundary effects using the techniques of references 26 and 27.

Overall wing efficiency was determined by examining three parameters: the lift-curve slope (C_{L_α}), the Oswald efficiency factor (e), and the cambered-wing efficiency factor (e^*). The changes in these characteristics were expected to be small. Least-squares curves were fitted to the measured data to determine the slopes of each curve in a consistent manner. To determine the lift-curve slope, the typical linear variation of lift coefficient with angle of attack was assumed:

$$C_L = C_{L_\alpha}(\alpha - \alpha_0) \qquad (5)$$

Inspection of the lift curves with fixed transition indicated that they were fairly linear over an angle-of-attack range from $-3.1°$ to $3.1°$. A linear least-squares curve was fit to the results within this angle-of-attack range to determine the angle of zero lift (α_0) and the lift-curve slope (C_{L_α}).

To determine the Oswald efficiency factor, the drag was assumed to vary linearly with the square of the lift coefficient:

$$C_D = C_{D,0} + \frac{1}{\pi A e} C_L^2 \qquad (6)$$

Inspection of the curves showing the variation of C_D with C_L^2 indicated that the curves became nonlinear at low lift coefficients because of the airfoil camber drag. The curves also were nonlinear at lift coefficients above about 0.5, which is near the maximum value of L/D (not presented). A linear least-squares curve was fit to the results for lift coefficients between 0.15 and 0.50 to obtain the slope (dC_D/dC_L^2). The lower limit was selected to eliminate the nonlinear points near zero lift, and the upper limit was selected to eliminate the nonlinear points at the higher angles of attack where trailing-edge separation occurred. The Oswald efficiency factor (e) was computed from this slope. Because of the linear curve,

the slope of the curve and the value of the Oswald efficiency factor are constant.

Because the wing utilized a cambered airfoil section, the minimum drag did not occur at zero lift but at a small positive lift. Thus, equation (6) is not the best representation of the variation of drag coefficient with lift coefficient for a wing with camber. Inspection of the variation of C_D with C_L (not shown) revealed the expected parabolic variation centered about $C_{L,\min}$, that is, the lift coefficient associated with the minimum total drag coefficient $(C_{D,\min})$. A more representative expression for the results is

$$C_D = C_{D,\min} + \frac{1}{\pi A e^*} \left(C_L - C_{L,\min}\right)^2 \qquad (7)$$

This equation was used to determine the cambered-wing efficiency factor (e^*). A quadratic least-squares curve was fitted to the drag data for lift coefficients below 0.50, and the results were used to determine the minimum total drag $(C_{D,\min})$, the associated lift $(C_{L,\min})$, and the drag at zero lift $(C_{D,0})$. Using the computed value of $C_{L,\min}$, a linear least-squares curve was fitted to the variation of C_D with $(C_L - C_{L,\min})^2$ for lift coefficients up to 0.50 to obtain the slope $\frac{dC_D}{d(C_L - C_{L,\min})^2}$. This slope was used to determine the cambered-wing efficiency factor (e^*). Results from the curve fits, presented in table 4, will be discussed with the appropriate data.

The viscous drag is generally a weak function of the angle of attack and, hence, of the lift coefficient. As shown in reference 14, a viscous contribution occurs to the drag due to lift (the K_p term) in addition to the inviscid contribution (the K_i term):

$$C_D = C_{D,\min}^* + K_p(C_L - C_{L,\min}^*)^2 + K_i \frac{C_L^2}{\pi A} \qquad (8)$$

As outlined in reference 15, the choice of an airfoil shape that has little or no variation of airfoil drag with lift squared ($K_p \approx 0$, at least for the lower angles of attack) allows a reduction of the viscous drag contribution to the lift-dependent drag variation. As a consequence, better agreement between the inverse of the theoretical inviscid induced-drag factor $(1/K_i)$ and the experimental Oswald efficiency factor (e) can be expected. As noted above, equation (7) is a better representation of the variation of the drag coefficient with lift coefficient for a wing with a cambered

airfoil section than equation (6). By using equation (7) to compute dC_D/dC_L^2 and the definition for the Oswald efficiency factor given in the section defining the symbols, the following relationship of the Oswald efficiency factor to the cambered-wing efficiency factor is derived:

$$e = \frac{e^*}{1 - (C_{L,\min}/C_L)} \qquad (9)$$

This equation indicates that for positive values of $C_{L,\min}$, the Oswald efficiency factor is greater than the cambered-wing efficiency factor.

Presentation of Results

The aerodynamic data presented in this report are identified by a unique "run" number. Results are presented in coefficient form in the stability-axes system. The same reference area was used for all four wings, although the projected area for wing D with the round tips was slightly larger than the area of the other wings. The same wing reference chord was used to nondimensionalize all pitching-moment data. The common aspect ratio of the elliptical wings was used to determine the Oswald efficiency factor and the cambered-wing efficiency factor. All results are with the transition fixed unless specifically noted otherwise. Aerodynamic characteristics presented in the following figures were measured in the 8-Ft TPT unless otherwise noted. Flow visualization results presented herein were derived from photographs taken in the 7 × 10 HST. Parameters derived from the curve fits of the results are listed in table 4. The drag coefficient at zero lift was derived from the quadratic curve fit because it represented the data better than the linear curve fit. The results are presented as follows:

Discussion of Results

This investigation centered on the effects of different parameters on wing efficiency as quantified by the lift-curve slope (C_{L_α}), the Oswald efficiency factor (e), and the cambered-wing efficiency factor (e^*). Repeatability of the basic aerodynamic characteristics is discussed first. The effects of boundary-layer transition, Reynolds number, Mach number, and wing planform on the basic aerodynamic characteristics are then presented. Results from the flow-visualization tests are discussed next. Finally, the effects of boundary-layer transition and wing planform on the wing efficiency parameters are discussed.

Data Repeatability

Wings A and C were tested at each Mach number and Reynolds number more than once. The repeatability of the results is excellent. A sample of the lift, drag, and pitching-moment data from wing A is presented in figure 11 for a Mach number of 0.3. The results from four runs are represented quite well by a single, representative curve. Note that the data include both model upright and inverted results. The lift curve was linear over the angle-of-attack range from $-3.1°$ to $3.1°$. Linear least-squares curves were fitted to the lift data within this angle-of-attack range for each run. The average deviation of the measured lift coefficient from the curve fit was 0.0006, and the standard deviation was 0.0008; this was less than the uncertainty in the lift coefficient of 0.0013. The difference between the maximum and minimum angles of zero lift was only 0.02°, which was slightly larger than the accuracy of the angle-of-attack measurement of 0.01°. The lift-curve slopes ranged in value from 0.0816 per degree to 0.0826 per degree.

The drag coefficient varied linearly with the lift coefficient squared over the range from 0.02 to 0.25. (The lift coefficient ranged from 0.15 to 0.50.) Linear least-squares curves were fitted to the drag data over this range of lift coefficient squared. The standard deviation of the measured drag data from the curve fit was about 0.00006, which was much smaller than the computed uncertainty in drag of 0.0004. As was found with the lift results, the different runs were in very good agreement with each other. The difference between the maximum and minimum values of the drag coefficients at zero lift was 0.0003, which was about the same as the uncertainty. The slopes of these curves were also in good agreement with each other. The pitching-moment curves were very repeatable. The high quality of the results allowed small differences to be discerned in the lift and drag, thus making them suitable for studying the effects of planform on the wing efficiency parameters.

Effect of Fixing the Location of Boundary-Layer Transition

Wing A was tested with free transition and fixed transition on the wing to determine the aerodynamic characteristics with and without a long run of a laminar boundary layer. The results, presented in figure 12 for a Mach number of 0.5, are typical of those measured with free and fixed transition at all three Mach numbers. Results from curve fits of the data at the other Mach numbers can be found in table 4. The thicker turbulent boundary layer with fixed transition tends to decrease the effective camber of the airfoil more than the thinner laminar boundary layer with free transition. Thus, the angle of zero lift is about 0.33° less negative and the lift-curve slope is reduced by 0.0026 per degree for fixed transition. With free transition, the location of boundary-layer transition changes with angle of attack.

Evidence of this change is the small nonlinearity in the lift curves with free transition that is apparent by close visual inspection of the plotted curves at negative angles of attack and by the increased root-mean-square (rms) error obtained from the linear curve fits. The slopes of the lift curves with free transition become smaller at small positive angles of attack. The change in slope may be associated with changes in the location of the boundary-layer transition on the upper surface and the presence of laminar separation bubbles. Fixing transition eliminates the long run of the laminar boundary layer and should reduce the possibility of laminar separation bubbles. With fixed transition, the lift curves are more nearly linear between $-3°$ and $3°$.

The higher skin friction of the turbulent boundary layer leads to an increase in the drag coefficient at zero lift of about 0.0030. This increase in drag coefficient is similar to the measured increase in minimum airfoil section drag coefficient for the NASA NLF(1)-0416 airfoil section (ref. 20).

The pitching moment with fixed transition is less negative because the thicker turbulent boundary layer with fixed transition decreases the effective camber of the airfoil more than the thinner boundary layer with free transition. The slope of the pitching-moment curve with fixed transition is constant over most of the angle-of-attack range. At positive angles of attack, the slopes with free and fixed transition are similar. At these conditions for free transition, the location of transition on the upper surface may have moved upstream to match the fixed-transition location. These results are consistent with the change in lift-curve slope at small positive angles of attack.

Effect of Reynolds Number

Boundary-layer growth (which is dependent on the Reynolds number) and the associated viscous drag variation influence the wing efficiency. Each wing was tested at two Reynolds numbers for a Mach number of 0.3. Results are presented for wing A in figure 13 with free transition and in figure 14 with fixed transition. In general, increasing the Reynolds number decreases the boundary-layer thickness at a given location. The lift-curve slope is higher for the higher Reynolds number (with a thinner boundary layer). Increasing the Reynolds number leads to a decrease in the drag coefficient at zero lift and a decrease in the slope of the drag coefficient versus the square of the lift coefficient curves (an increase in the Oswald efficiency factor). The pitching moment becomes more negative at the higher Reynolds number because the thinner boundary layer does not reduce the effective camber as much as a thicker boundary layer. These trends in the lift-curve slope and Oswald efficiency factor going from the lower to the higher Reynolds number (with a decreasing boundary-layer thickness) are similar to the trends going from fixed transition to free transition (with a decreasing boundary-layer thickness). The effect of Reynolds number on the results from wings B, C, and D with transition fixed (which is not presented herein) is similar to the effect of Reynolds number on the results from wing A with transition fixed. The results from curve fits of the data from wings B, C, and D may be found in table 4.

Effect of Mach Number

Tests on each wing were conducted at a chord Reynolds number of 2.1×10^6 for three Mach numbers: 0.3, 0.4, and 0.5. At these Mach numbers and moderate lift coefficients, the flow should be subcritical everywhere on the wing. The effect of Mach number on the aerodynamic characteristics of each wing is presented in figures 15 to 18. Changes with Mach number are similar for all four wings. In general, for a given wing, the angle of zero lift becomes less negative and the lift-curve slope increases as the Mach number increases. Increasing the Mach number increases the drag coefficient at zero lift slightly and makes the pitching-moment coefficient more negative.

Effect of the Rectangular Wingtip Shape

Wing D, which has a rectangular planform, was tested both with tips that had square ends and with tips that had round ends. All data have been reduced by the wing reference area (384.00 in^2). The projected area of wing D with the round tips is 390.34 in^2. The aerodynamic coefficients for wing D with the round tip can be renormalized by the projected area by multiplying by 0.9838. A comparison of the results with the different tips is presented in figure 19. In spite of the increase in area of the round tip, the tip shape has little apparent effect on the lift. Results from the curve fits indicate that changing the tip shape has no measurable effect on the angle of zero lift. The lift-curve slope is slightly smaller for the wing with the round tip although it has a larger actual planform area.

Renormalizing the round tip results with the actual planform area would further reduce the lift-curve slope for the round tip. Thus, for a given angle of attack, the loading on the wing with the round tip is less than the loading with the square tip. The drag coefficient at zero lift is larger for the wing with the square tip, possibly because of the separated flow over the face of the square tip. The slope of the drag curve $(1/\pi Ae)$ is larger for the round tip in spite of the increased actual aspect ratio. The Oswald efficiency factor for the wing with the square tip is 0.974. By renormalizing the data for the round tip for actual projected planform area and the actual aspect ratio, the Oswald efficiency factor for the wing with the round tip is 0.903. Because of the possibility that higher loading can be maintained near the tip with the square end than near the tip with the round end at a given angle of attack, an elliptical load distribution can be approached more closely.

Effect of Planform Shape

The three elliptical planform wings have different span load distributions. Contributing factors are different spanwise flows in the boundary layer associated with different curvature of the quarter-chord lines and different induced downwash distributions associated with each wing planform and wake shape. The effect of planform shape on the aerodynamic characteristics is presented in figure 20 for a Mach number of 0.5. The uncertainties in the lift and drag coefficient measurements are smaller than the changes in the lift and drag coefficients between wing A and wings B and C. Results from the curve fits in table 4 indicate that the angle of attack at zero lift becomes more negative by about 0.11° to 0.14° as the wingtip is swept aft. The drag coefficient at zero lift does not change as the planform sweep changes. The effects of planform shape on the lift-curve slope and on the drag-curve slope (or wing efficiency factor) will be discussed in the subsequent section on wing efficiency. These results are typical of those

obtained at the two lower Mach numbers which are not included herein.

Tunnel-to-Tunnel Data Comparison Studies

All four wings were tested in both the 8-Ft TPT and the 7 × 10 HST at Mach numbers of 0.3, 0.4, and 0.5. A sample of the aerodynamic results from both tunnels for wing A is presented at $M_\infty = 0.5$ in figure 21. This Mach number was selected because the Reynolds number of 1.9×10^6 from the tests in the 7 × 10 HST was close to the larger Reynolds number of 2.1×10^6 from the tests in the 8-Ft TPT. The results from both tunnels showed similar trends although small differences existed. The difference between the angles of attack at zero lift was small. The lift-curve slope measured in the 7 × 10 HST was about 2 percent less than that measured in the 8-Ft TPT. The drag at zero lift was larger in the results from the 7 × 10 HST. The slope of the drag curve obtained from the curve fits was greater in the results from the 7 × 10 HST. The pitching-moment curves were similar except that a small positive shift occurred in the results from the 7 × 10 HST.

Flow Visualization Studies

Because no drastic differences exist between the aerodynamic results from the two tunnels, the flow fields should be sufficiently similar that surface oil-flow studies from the 7 × 10 HST can be used to aid in the analysis of the results from the 8-Ft TPT. Fluorescent-oil-flow visualization photographs were taken at Mach numbers of 0.3 and 0.5 at several angles of attack in the 7 × 10 HST. Sketches of the oil-flow patterns on the upper surface of each of the four wings, derived from the photographs, are presented for several angles of attack at a Mach number of 0.5 in figures 22 to 25. Flow visualization photographs obtained at a Mach number of 0.3 did not show any significant differences when compared with those obtained at a Mach number of 0.5. In general, the oil-flow patterns for the three elliptical chord wings are similar near the wing-body juncture and over the forward portion of the chord across the central portion of the wing. Significant differences generally appear near the trailing edge and near the tip. The patterns on each of the wings are discussed separately.

Sketches of the oil-flow patterns on the upper surface of wing A are presented in figure 22. The oil-flow patterns indicate that attached flow occurs across the wing with only a small isolated region of separation near the wing-root trailing edge at angles of attack of 4° or higher. Aerodynamic results

presented in figure 12(a) showed that a reduction in the lift-curve slope was observed at angles of attack of about 3° to 4° which likely corresponded to the onset of this inboard trailing-edge separation. Over most of the wing, the flow near the surface moves in a streamwise direction. Near the wing-body juncture, the flow moves outboard over the rear portion of the chord with the outward movement increasing with increasing angle of attack. Near the trailing edge, the flow generally moves inboard. The beginning of this inward flow region moves forward along the chord as the angle of attack increases. Near the tip, the flow moves inboard, with the inward movement increasing with increasing angle of attack. No flow separation was observed in the tip region of wing A for the angles of attack studied. Flow visualization results were reported in reference 16 on a wing similar to wing A that had an aspect ratio of 7, a nondimensional tip location (x_{tip}/c_{root}) of 0.25, and a symmetrical airfoil section. Those results showed that the flow pattern on the surface was very similar to that of the present test. Like the present test, no separation was detected for lift coefficients up to 0.5.

Flow visualization sketches of the oil-flow patterns (lines) on the upper surface of wing B are presented in figure 23. The flow patterns near the wing root and over the forward portion of the central part of the wing are similar to those observed for wing A. Over the central portion of the wing, the flow near the surface moves in a streamwise direction all the way back to the trailing edge. At an angle of attack of 0°, the flow near the tip is generally streamwise. As the angle increases, the oil-flow pattern changes significantly near the wingtip. The flow lines begin to move outboard and an isolated region of separation develops at the trailing edge. At the tip, the flow has wiped the oil from the surface, with the oil collecting in a separated region near the trailing edge of the tip. The leading-edge sweep angle is very large in this region, and so it is possible that a vortex has formed and is wiping the oil from the surface along its path.

Sketches derived from the flow visualization photographs of the upper surface of wing C are presented in figure 24. No significant differences were identified in the flow lines of wing C from those of wings A and B either near the wing-body juncture or over the forward portion of the chord on the central portion of the wing. Away from the wing-body juncture, the flow moves slightly outboard in the region where the trailing edge is roughly normal to the free-stream direction. Farther outboard, the outward movement of the flow increases near the trailing edge. The outward movement increases dramatically near

the wingtip. At $\alpha = 0°$, the oil has been wiped from the surface at the tip, possibly by a vortex originating at the highly swept leading edge. A similar flow pattern was found at the higher angles of attack for wing B. A small separated region appears outboard and aft of this region at $\alpha = 0°$. As the angle of attack increases, the flow over the outer portion of the wing turns spanwise toward the tip with a separated region near the trailing edge. The separated-flow region becomes much larger as the angle of attack increases. At $\alpha = 6°$, the shape of the attached-flow region on wing C is similar to that of wing B. The flow on much of the wingtip of wing C is separated, provides little benefit, and can be expected to cause a drag increase.

Flow visualization results were reported in reference 16 on a wing similar to wing C with an aspect ratio of 7, a nondimensional tip location (x_{tip}/c_{root}) of 1.50, and a symmetrical airfoil section. Those results showed the same trends found in the present tests. However, no significant flow separation was observed in reference 16 until a lift coefficient of 0.5 was reached. The difference may again be attributable to the difference in the airfoil sections and to the aspect ratios. The flow patterns in reference 16 at higher angles of attack show a large separated region near the wingtip that is similar to that found on wing C in this investigation at $\alpha = 6°$.

The oil-flow patterns on the upper surface of wing D with the square tip are presented in figure 25. No flow visualization data were obtained for wing D with the round tip. As was found with the elliptical wings, the flow moves outward along the wing-body juncture. Over most of the middle portion of the wing, the flow generally follows the free-stream direction. On the outboard portion of the wing, the flow patterns move inboard with the inward movement larger at the larger angle of attack. Close to the tip, the flow ceases its inboard movement and moves outward and eventually separates just before the tip trailing edge.

Wing Efficiency

The wing with the highest efficiency should have the least induced downwash, and thus it should have a lift-curve slope closest to the two-dimensional lift-curve slope of the airfoil section used on the wing. The wing with a span load distribution that induces the smallest downwash will have the largest lift-curve slope and the largest Oswald efficiency factor for a given aspect ratio. The lift-curve slope, the Oswald efficiency factor, and the cambered-wing efficiency factor will be used to determine the relative efficiencies of the wings.

Effect of transition. Fixing transition with strips of grit near the wing leading edge will force the boundary layer to transition to turbulent flow near the leading edge. Without the transition strips, the boundary layer on those portions of the wing with little or moderate sweep should remain laminar for a significant portion of the chord because of the natural laminar flow airfoil. In the absence of laminar separation bubbles, a laminar boundary layer is thinner than a turbulent boundary layer, and so the effective airfoil shape with free transition should be closer to the actual airfoil shape. The basic aerodynamic results with fixed and free transition were presented in figure 12 for wing A. A linear least-squares curve was fitted to the variation of lift coefficient with angle of attack to determine the lift-curve slope. The computed lift-curve slopes with fixed and free transition are plotted in figure 26. The slopes for wing A with free transition are greater than the slopes with fixed transition at each Mach number.

A linear least-squares curve was fitted to the variation of the drag coefficients as a function of the square of the lift coefficients to determine the Oswald efficiency factor. Results are presented in figure 27 with fixed and free transition. Considerable scatter occurs in the results at a Mach number of 0.3. The Oswald efficiency factor is generally independent of the Mach number. The results with free transition have a slightly larger Oswald efficiency factor, although the difference between the fixed and free transition values is about the same as the scatter in the fixed transition values.

To obtain the cambered-wing efficiency factor, a linear least-squares curve was fitted to the variation of the drag coefficients as a function of the square of the lift coefficients biased by the lift coefficient associated with minimum total drag. The results for the cambered-wing efficiency factor presented in figure 28 indicate that the wing with fixed transition has the higher efficiency. However, as noted above, the other two indicators of wing efficiency (the lift-curve slope and the Oswald efficiency factor) indicate that the wing with free transition has the higher efficiency. A comparison of the results for fixed and free transition requires a consideration of the different effective camber for each of these two cases. The different effective camber results in values of $C_{L,min}$ of about 0.01 for fixed transition and of about 0.06 for free transition. When these $C_{L,min}$ values are used to compute the cambered-wing efficiency factor, substantial changes in the relationship of the wing efficiencies for fixed and free transition can occur. Therefore, subsequent comparisons of the effect of wing planform on the Oswald and

cambered-wing efficiency factors will involve only results with fixed transition. For these fixed transition cases, the value of $C_{L,\min}$ will be about the same and will not be a factor. Therefore, the trends for the Oswald efficiency factor and the cambered-wing efficiency factor should be the same.

Variation of efficiency parameters with Reynolds number.

Changing the Reynolds number will change the boundary-layer displacement thickness, thereby changing the effective airfoil shape and the lift as well as the drag. Increasing the Reynolds number should decrease the boundary-layer thickness for fixed transition. The basic aerodynamic results with fixed transition for the two Reynolds numbers were presented in figure 14. The variation of the computed lift-curve slopes with Reynolds number for the three elliptical planform wings is plotted in figure 29, and the lift-curve slope for each of the three wings increases with increasing Reynolds number. This is consistent with the effect of transition discussed previously in that the results associated with the thinner boundary layer have the higher lifting efficiency.

The variation of the computed Oswald efficiency factor with Reynolds number for the three elliptical wings is plotted in figure 30. The Oswald efficiency factor increases as the Reynolds number increases. As was the case for the effect of transition, the change in value of the Oswald efficiency factor with Reynolds number is about the same as the scatter.

The variation of the cambered-wing efficiency factor for the three elliptical planform wings is plotted in figure 31. Because of the large scatter in the results at the higher Reynolds number, no trend in the cambered-wing efficiency factor with Reynolds number can be determined. The lift-curve slope and the Oswald efficiency factor indicate that wing efficiency increases with increasing Reynolds number.

Variation of efficiency parameters with Mach number.

Changing the curvature of the quarter-chord line (planform shape) changes the spanwise flow in the boundary layer and the span load distribution for the three elliptical planform wings. Changing the curvature of the quarter-chord line should change the three wing efficiency parameters. The basic aerodynamic results from the tests in the 8-Ft TPT for each of the wings are presented in figures 15 to 18. The lift-curve slopes were computed and the results are plotted in figure 32. The lift-curve slopes for the results from the 7 × 10 HST at a Mach number of 0.5 are included in figure 32 because the Reynolds number is close to the Reynolds number

from the tests in the 8-Ft TPT. In general, the lift-curve slopes measured in the 7 × 10 HST are smaller than those measured in the 8-Ft TPT, but similar trends are found on the effect of planform shape on the lift-curve slope.

The results for wing D with the square tip are provided as a baseline. For wing D, the local chord Reynolds number is constant across the wingspan so that possible flow separation problems associated with low Reynolds numbers near the tip of the elliptical wings are not present. Flow visualization results indicate that the flow generally moves in a spanwise direction with separation confined to the edge of the wingtip. Thus, wing D has a larger lift-curve slope than each of the three elliptical wings.

Some scatter occurs in the results but, of the three elliptical wings, the wing with the unswept trailing edge (wing B) has the highest lift-curve slope at a given Mach number and thus has the highest efficiency based on that parameter. The highly swept wing (wing C) has a larger lift-curve slope than the unswept wing (wing A). The results reported in reference 15 did not indicate a change in lift-curve slope for the planforms similar to wings A and C. The reason for the discrepancy between the two tests is not known.

The Oswald efficiency factors were computed for the data presented in figures 15 to 18, and the results are presented in figure 33. The Oswald efficiency factors computed from the results obtained at the 7 × 10 HST at $M_\infty = 0.5$ are included in figure 33. The results for wing D are again presented as a baseline. The Oswald efficiency factor of the rectangular wing D is similar to the elliptical wing A with the unswept quarter-chord line. The square tip may promote high loading out close to the tip, which would approximate the large change in loading near the tip of an elliptical span load distribution. As was found for the lift-curve slopes, the wing with the straight trailing edge (wing B) has the largest Oswald efficiency factor, the wing with the unswept quarter-chord line (wing A) has the lowest Oswald efficiency factor, and the crescent-shaped wing (wing C) has an efficiency in between. This result is consistent with results reported in reference 15 which suggested that a wing similar to wing C had a 2- to 4-percent larger Oswald efficiency factor than a wing similar to wing A. The computed Oswald efficiency factors from the 7 × 10 HST are smaller than those obtained in the 8-Ft TPT. The change in e is too small in the 7 × 10 HST tests to definitely state which wing had the highest Oswald efficiency factor.

The cambered-wing efficiency factors are presented in figure 34. The results are generally consistent with the Oswald efficiency factor although the scatter is larger. The cambered-wing efficiency factor from the 8-Ft TPT is the highest for wing B, the lowest for wing A, and is scattered in between for wing C.

Conclusions

Three planar, untwisted wings with the same elliptical spanwise chord distributions but different planform shapes have been tested in the Langley 8-Foot Transonic Pressure Tunnel (8-Ft TPT) and in the Langley 7- by 10-Foot High-Speed Tunnel (7 × 10 HST). The experiments were designed to obtain drag measurements as accurately as possible. Each wing was tested at Mach numbers from 0.3 to 0.5 over an angle-of-attack range from −4° to 7°. Tests in the 8-Ft TPT were at chord Reynolds numbers of 1.5×10^6 and 2.1×10^6, and tests in the 7 × 10 HST were at chord Reynolds numbers ranging from 1.3×10^6 to 1.9×10^6. The wing lift-curve slope, Oswald efficiency factor, and cambered-wing efficiency factor were used to determine the wing efficiency from an induced-drag standpoint. The results of this investigation indicated the following conclusions:

1. Fixing the boundary-layer transition near the leading edge of a wing with a laminar flow airfoil reduces the effective camber of the airfoil and leads to a less negative angle of attack at zero lift and an increase in the drag coefficient at zero lift. The higher lift-curve slope and Oswald efficiency factor with the free transition indicate that the wing with the longer laminar boundary layer is more efficient.

2. Increasing the Reynolds number decreases the drag coefficient at zero lift, increases the lift-curve slope, and increases the Oswald efficiency factor.

3. The lift-curve slope for the rectangular wing D was larger than the lift-curve slopes for the three elliptical wings. The Oswald efficiency factor of the rectangular wing was similar to that of the elliptical wing A with the unswept quarter-chord line.

4. Moving the wingtip aft (increasing the curvature of the quarter-chord line) makes the angle of attack at zero lift more negative but has little effect on the drag coefficient at zero lift. The change in lift-curve slope and the change in the Oswald efficiency factor with the change in curvature of the quarter-chord line (wingtip location) indicate that the elliptical wing with the unswept quarter-chord line (wing A) has the lowest lifting efficiency, the wing with the straight trailing edge (wing B) has the highest lifting efficiency, and the crescent-shaped wing (wing C) has an efficiency in between wings A and B. The small increase in the Oswald efficiency factor for the elliptical wing with the crescent-shaped planform (wing C) relative to the elliptical wing with the unswept quarter-chord line (wing A) is an indication that the improvement in the lifting efficiency is consistent with the trends reported in other published experimental and computational studies.

5. Flow visualization results indicate that for lifting conditions, the flow near the tip on the upper surface of the elliptical wing with the unswept quarter-chord line (wing A) is swept inboard. The flow near the tip of the wing with the straight trailing edge (wing B) moves streamwise at the lower angles of attack and slightly outboard at the higher angles of attack. The flow patterns near the tip of the crescent-shaped wing (wing C) are swept outboard with a separated flow region near the trailing edge of the wingtip. The flow patterns at the tip of the straight trailing-edge wing (wing B) and of the crescent-shaped wing (wing C) indicate a scrubbed area near the tip, probably caused by a vortex originating at the highly swept leading edge. The flow pattern near the tip on the rectangular wing (wing D) generally moves inboard over the forward portion of the chord and outboard over the rear portion of the chord with a small separated region at the edge of the tip.

Appendix

Derivation of Uncertainties in Lift, Drag, and Mach Number

The uncertainty of the measurements of the derived lift and drag coefficients and Mach number depends on the uncertainties of the primary measurements. This appendix presents a description of the technique used to determine the uncertainty in the lift, drag, and Mach number. The technique uses the principles presented in reference 28. The primary measurements used to define the lift and drag coefficients are the balance normal force (F_N), axial force (F_A), model angle of attack (α), free-stream static pressure (p_∞), and free-stream total pressure (p_t). The wing reference area (S) is assumed to be exact. The free-stream static pressure and the free-stream total pressure are used to compute the free-stream Mach number (M_∞), which, in turn, is used to compute the free-stream dynamic pressure (q_∞).

The lift (L) and drag (D) are defined by

$$L = F_N \cos \alpha - F_A \sin \alpha \tag{A1}$$

$$D = F_A \cos \alpha + F_N \sin \alpha \tag{A2}$$

Dividing both sides by $q_\infty S$ gives the following expressions for lift and drag coefficients, respectively:

$$C_L = \frac{F_N \cos \alpha}{q_\infty S} - \frac{F_A \sin \alpha}{q_\infty S} \tag{A3}$$

$$C_D = \frac{F_A \cos \alpha}{q_\infty S} + \frac{F_N \sin \alpha}{q_\infty S} \tag{A4}$$

The free-stream dynamic pressure, which is obtained from the Mach number, is

$$q_\infty = \frac{1}{2} \gamma p_\infty M_\infty^2 \tag{A5}$$

where γ denotes the ratio of specific heats. Substituting equation (A5) into the equations for the lift and drag coefficients (eqs. (A3) and (A4), respectively) gives

$$C_L = \frac{F_N \cos \alpha}{\frac{1}{2} \gamma p_\infty M_\infty^2 S} - \frac{F_A \sin \alpha}{\frac{1}{2} \gamma p_\infty M_\infty^2 S} \tag{A6}$$

$$C_D = \frac{F_A \cos \alpha}{\frac{1}{2} \gamma p_\infty M_\infty^2 S} + \frac{F_N \sin \alpha}{\frac{1}{2} \gamma p_\infty M_\infty^2 S} \tag{A7}$$

The Mach number, which is not a primary measurement, is derived from the free-stream static and total pressures and the ratio of specific heats. Thus,

$$M_\infty = \left\{ \frac{2}{\gamma - 1} \left[\left(\frac{p_\infty}{p_t} \right)^{-\frac{\gamma-1}{\gamma}} - 1 \right] \right\}^{1/2} \tag{A8}$$

The lift coefficient and drag coefficient are functions of five "measured" variables: the normal force, the axial force, the angle of attack, the free-stream static pressure, and the free-stream Mach number. The Mach number is a function of the free-stream static pressure and the stagnation pressure. The uncertainties of each of these measured variables, designated by $U(\ )$, are presented in table A1. The probability of the value of each uncertainty being correct is assumed to be the same. From reference 28, the uncertainty in the derived measurements with the same probability is

$$U(C_L) = \left\{ \left[\frac{\partial C_L}{\partial F_N} U(F_N) \right]^2 + \left[\frac{\partial C_L}{\partial F_A} U(F_A) \right]^2 + \left[\frac{\partial C_L}{\partial \alpha} U(\alpha) \right]^2 + \left[\frac{\partial C_L}{\partial p_\infty} U(p_\infty) \right]^2 + \left[\frac{\partial C_L}{\partial M_\infty} U(M_\infty) \right]^2 \right\}^{1/2} \tag{A9}$$

$$U(C_D) = \left\{ \left[\frac{\partial C_D}{\partial F_N}U(F_N)\right]^2 + \left[\frac{\partial C_D}{\partial F_A}U(F_A)\right]^2 + \left[\frac{\partial C_D}{\partial \alpha}U(\alpha)\right]^2 + \left[\frac{\partial C_D}{\partial p_\infty}U(p_\infty)\right]^2 + \left[\frac{\partial C_D}{\partial M_\infty}U(M_\infty)\right]^2 \right\}^{1/2}$$

(A10)

$$U(M_\infty) = \left\{ \left[\frac{\partial M_\infty}{\partial p_\infty}U(p_\infty)\right]^2 + \left[\frac{\partial M_\infty}{\partial p_t}U(p_t)\right]^2 \right\}^{1/2}$$

(A11)

The equations for lift coefficient, drag coefficient, and Mach number are used to obtain the sensitivity of the derived quantity with respect to each of the primary measurements. These sensitivity factors change as the values of the primary measurements change. The uncertainty in Mach number was determined using the nominal tunnel static and total pressures for the two Reynolds numbers and three Mach numbers. The contributions of the static pressure measurement and total pressure measurement are presented in table A2 along with the uncertainty in the Mach number. The contributions of the total pressure uncertainty and static pressure uncertainty to the Mach number uncertainty are about the same. For these test conditions, the uncertainty in the Mach number is very small, typically 0.0003 to 0.0004.

The contribution of each of the primary measurements to the lift coefficient is presented in table A3 along with the uncertainty in the lift coefficient. The uncertainty of the normal force is the largest contributor to the uncertainty in the lift coefficient, with a smaller contribution coming from the Mach number uncertainty. The uncertainty becomes smaller as the Reynolds number and/or the Mach number increases. Over the small angle-of-attack range of these results, the uncertainty is relatively constant and small. The lift coefficient uncertainty ranges from 0.001 to 0.002.

The contribution of each of the primary measurements to the drag coefficient is presented in table A4 along with the uncertainty in the drag coefficient. The uncertainty of the axial force is the largest contributor to the uncertainty in the drag coefficient, with a smaller contribution coming from the uncertainty in the angle of attack. The uncertainty becomes smaller as the Reynolds number and/or the Mach number increases. Over the small angle-of-attack range of these results, the uncertainty is relatively constant for a given Mach number and Reynolds number. The drag coefficient uncertainty ranges from 0.0003 to 0.0006.

Table A1. Uncertainties in the Primary Measurement

$U(F_N)$, lbf 0.70
$U(F_A)$, lbf 0.25
$U(\alpha)$, deg 0.01
$U(p_\infty)$, psf . . . . <0.30
$U(p_t)$, psf . . . . <0.30

Table A2. Contribution of Primary Measurements
to Mach Number Uncertainty

M_∞	R_c	$\frac{\partial M_\infty}{\partial p_\infty} U(p_\infty)$	$\frac{\partial M_\infty}{\partial p_t} U(p_t)$	$U(M_\infty)$
0.3	1.5×10^6	−0.0003	0.0003	0.0004
.3	2.1	−.0002	.0002	.0003
.4	2.1	−.0002	.0002	.0003
.5	2.1	−.0002	.0002	.0003

Table A3. Contribution of Primary Measurements to Lift Coefficient Uncertainty

M_∞	α, deg	$\frac{\partial C_L}{\partial F_N}U(F_N)$	$\frac{\partial C_L}{\partial F_A}U(F_A)$	$\frac{\partial C_L}{\partial \alpha}U(\alpha)$	$\frac{\partial C_L}{\partial p_\infty}U(p_\infty)$	$\frac{\partial C_L}{\partial M_\infty}U(M_\infty)$	$U(C_L)$
[a]0.3	−3.0	0.00172	0.00003	<0.00001	0.00000	0.00001	0.0017
	0	.00172	.00000	<0.00001	−.00003	−.00071	.0019
	3.0	.00172	−.00003	<0.00001	−.00006	−.00137	.0022
0.3	−3.0	0.00124	0.00002	<0.00001	0.00000	−0.00004	0.0012
	0	.00124	.00000	<0.00001	−.00002	−.00052	.0013
	3.0	.00124	−.00002	<0.00001	−.00005	−.00101	.0016
0.4	−3.0	0.00096	0.00002	<0.00001	0.00000	0.00001	0.0010
	0	.00096	.00000	<0.00001	−.00003	−.00040	.0010
	3.0	.00096	−.00002	<0.00001	−.00006	−.00080	.0012
0.5	−3.0	0.00078	0.00002	<0.00001	0.00000	0.00000	0.0008
	0	.00078	.00000	<0.00001	−.00004	−.00035	.0009
	3.0	.00078	−.00002	<0.00001	−.00008	−.00066	.0010

[a]Data are at $R_c = 1.5 \times 10^6$; all other data are at $R_c = 2.1 \times 10^6$.

Table A4. Contribution of Primary Measurements to Drag Coefficient Uncertainty

M_∞	α, deg	$\frac{\partial C_D}{\partial F_N}U(F_N)$	$\frac{\partial C_D}{\partial F_A}U(F_A)$	$\frac{\partial C_D}{\partial \alpha}U(\alpha)$	$\frac{\partial C_D}{\partial p_\infty}U(p_\infty)$	$\frac{\partial C_D}{\partial M_\infty}U(M_\infty)$	$U(C_D)$
[a]0.3	−3.0	−0.00010	0.00061	0.00000	<0.00001	−0.00004	0.0006
	0	.00000	.00061	.00005	<0.00001	−.00005	.0006
	3.0	.00009	.00062	.00009	<0.00001	−.00007	.0006
0.3	−3.0	−0.00006	0.00044	0.00000	<0.00001	−0.00002	0.0004
	0	.00000	.00044	.00005	<0.00001	−.00003	.0004
	3.0	.00007	.00044	.00009	<0.00001	−.00005	.0005
0.4	−3.0	−0.00005	0.00034	0.00000	<0.00001	−0.00002	0.0002
	0	.00000	.00034	.00005	<0.00001	−.00002	.0003
	3.0	.00005	.00034	.00009	<0.00001	−.00004	.0004
0.5	−3.0	−0.00004	0.00028	0.00000	<0.00001	−0.00002	0.0003
	0	.00000	.00028	.00005	<0.00001	−.00002	.0003
	3.0	.00004	.00028	.00009	<0.00001	−.00003	.0003

[a]Data are at $R_c = 1.5 \times 10^6$; all other data are at $R_c = 2.1 \times 10^6$.

References

1. Zimmer, H.: *Aerodynamic Optimization of Wings at Subsonic Speeds and the Influence of Wingtip Design.* NASA TM-88534, 1983.

2. Munk, Max M.: *The Minimum Induced Drag of Aerofoils.* NACA Rep. 121, 1921.

3. Cone, Clarence D., Jr.: *The Theory of Induced Lift and Minimum Induced Drag of Nonplanar Lifting Systems.* NASA TR R-139, 1962.

4. Whitcomb, Richard T.: *A Design Approach and Selected Wind-Tunnel Results at High Subsonic Speeds for Wing-Tip Mounted Winglets.* NASA TN D-8260, 1976.

5. Whitcomb, R. T.: Methods for Reducing Subsonic Drag Due to Lift. *Special Course on Concepts for Drag Reduction,* AGARD-R-654, June 1977, pp. 2-1–2-17.

6. Milne-Thomson, L. M.: *Theoretical Aerodynamics,* Fourth ed. Dover Publ., Inc., c.1958.

7. Burkett, Chris W.: Reductions in Induced Drag by the Use of Aft Swept Wing Tips. *Aeronaut. J.,* vol. 93, Dec. 1989, pp. 400–405.

8. Lowson, Martin V.: Minimum Induced Drag for Wings With Spanwise Camber. *J. Aircr.,* vol. 27, no. 7, July 1990, pp. 627–631.

9. Van Dam, C. P.: Induced-Drag Characteristics of Crescent-Moon-Shaped Wings. *J. Aircr.,* vol. 24, no. 2, Feb. 1987, pp. 115–119.

10. Van Dam, C. P.; Vijgen, P. M. H. W.; and Obara, C. J.: Keels and Rudders With Highly Swept Tips. Paper presented at AIAA/SNAME 18th Annual International Conference on Sailing Technology (Formerly The Ancient Interface) (Stanford University, California), Oct. 14–15, 1989.

11. DeHaan, Mark A.: Induced Drag of Wings With Highly Swept and Tapered Wing Tips. *A Collection of Technical Papers, Part 2—AIAA 8th Applied Aerodynamics Conference,* Aug. 1990, pp. 571–581. (Available as AIAA-90-3062-CP.)

12. Van Dam, C. P.; Nikfetrat, Koorosh; Vijgen, P. M. H. W.; and Fremaux, C. M.: Calculation and Measurement of Induced Drag at Low Speeds. SAE Paper 901935, Oct. 1990.

13. Van Dam, C. P.; Nikfetrat, K.; and Vijgen, P. M. H. W.: Lift and Drag Calculations for Wings and Tails: Techniques and Applications. *Contemporary Mathematics,* Volume 141 of *Fluid Dynamics in Biology,* A. Y. Cheer and C. P. van Dam, eds., American Mathematical Soc., 1993, pp. 463–477.

14. Vijgen, P. M. H. W.; Van Dam, C. P.; and Holmes, B. J.: Sheared Wing-Tip Aerodynamics: Wind-Tunnel and Computational Investigation. *J. Aircr.,* vol. 26, no. 3, Mar. 1989, pp. 207–213.

15. Van Dam, C. P.; Vijgen, P. M. H. W.; and Holmes, B. J.: Experimental Investigation on the Effect of Crescent Planform on Lift and Drag. *J. Aircr.,* vol. 28, no. 11, Nov. 1991, pp. 713–720.

16. Van Dam, C. P.; Vijgen, P. M. H. W.; and Holmes, B. J.: Aerodynamic Characteristics of Crescent and Elliptic Wings at High Angles of Attack, *J. Aircr.,* vol. 28, Apr. 1991, pp. 253–260.

17. Holbrook, G. Thomas; Dunham, Dana Morris; and Greene, George C.: *Vortex Wake Alleviation Studies With a Variable Twist Wing.* NASA TP-2442, 1985.

18. Schaefer, William T., Jr.: *Characteristics of Major Active Wind Tunnels at the Langley Research Center.* NASA TM X-1130, 1965.

19. Fox, Charles H., Jr.; and Huffman, Jarrett K.: *Calibration and Test Capabilities of the Langley 7- by 10-Foot High Speed Tunnel.* NASA TM X-74027, 1977.

20. Somers, Dan M.: *Design and Experimental Results for a Natural-Laminar-Flow Airfoil for General Aviation Applications.* NASA TP-1861, 1981.

21. Braslow, Albert L.; and Knox, Eugene C.: *Simplified Method for Determination of Critical Height of Distributed Roughness Particles for Boundary-Layer Transition at Mach Numbers From 0 to 5.* NACA TN 4363, 1958.

22. Covell, Peter F.; Hernandez, Gloria; Flamm, Jeffrey D.; and Rose, Ollie J.: Supersonic Aerodynamic Characteristics of a Mach 3 High-Speed Civil Transport Configuration. AIAA-90-3210, Sept. 1990.

23. Russo, G. P.: Techniques for Boundary Layer Tripping and Control. *Boundary Layer Simulation and Control in Wind Tunnels.* AGARD-AR-224, Apr. 1988, pp. 80–90. (Available from DTIC as AD A198 667.)

24. Poll, D. I. A.; and Paisley, D. J.: On the Effect of Wing Taper and Sweep Direction on Leading Edge Transition. *Aeronaut. J.,* vol. 89, Mar. 1985, pp. 109–117.

25. Gaster, M.: On the Flow Along Swept Leading Edges. *Aeronaut. Q.,* vol. XVIII, pt. 2, May 1967, pp. 165–184.

26. Gillis, Clarence L.; Polhamus, Edward C.; and Gray, Joseph L., Jr.: *Charts for Determining Jet-Boundary Corrections for Complete Models in 7- by 10-foot Closed Rectangular Wind Tunnels.* NACA WR L-123, 1945. (Formerly NACA ARR L5G31.)

27. Herriott, John G.: *Blockage Corrections for Three-Dimensional-Flow Closed-Throat Wind Tunnels, With Consideration of the Effect of Compressibility.* NACA Rep. 995, 1950. (Supersedes NACA RM A7B28.)

28. Holman, J. P.: *Experimental Methods for Engineers, Fifth ed.* McGraw-Hill, c.1989.

Table 1. Physical Characteristics of Models

Wing	b, in.	c_{root}, in.	S, in^2	A	$\dfrac{x_{\text{tip}}}{c_{\text{root}}}$
A	48.00	10.19	384.00	6.00	0.25
B	↓	10.19	↓	↓	1.00
C	↓	10.19	↓	↓	1.50
D (square tip)	↓	8.00	↓	↓	
D (round tip)	49.28	8.00	390.34	6.22	

Table 2. Design Coordinates of the NASA NLF(1)-0416 Airfoil

Upper surface		Lower surface	
x/c	z/c	x/c	z/c
0.00000	0.00000	0.00000	0.00000
.00049	.00403	.00073	−.00439
.00509	.01446	.00709	−.01154
.01393	.02573	.01956	−.01883
.02687	.03729	.03708	−.02594
.04383	.04870	.05933	−.03254
.06471	.05964	.08609	−.03847
.08936	.06984	.11708	−.04361
.11761	.07904	.15200	−.04787
.14925	.08707	.19050	−.05121
.18404	.09374	.23218	−.05357
.22169	.09892	.27659	−.05494
.26187	.10247	.32326	−.05529
.30422	.10425	.37167	−.05462
.34839	.10405	.42127	−.05291
.39438	.10162	.47150	−.05009
.44227	.09729	.52175	−.04614
.49172	.09166	.57122	−.04063
.54204	.08515	.62019	−.03250
.59256	.07801	.67014	−.02231
.64262	.07047	.72107	−.01221
.69155	.06272	.77156	−.00364
.73872	.05493	.82012	.00278
.78350	.04724	.86536	.00667
.82530	.03977	.90576	.00792
.86357	.03265	.93978	.00696
.89779	.02594	.96638	.00478
.92749	.01974	.98520	.00242
.95224	.01400	.99633	.00065
.97197	.00862	1.00000	.00000
.98686	.00398		
.99656	.00098		
1.00000	.00000		

Table 3. Design Coordinates of Model Forebody

Axial location, in.	Radius, in.
0.000	0.000
.010	.106
.020	.150
.040	.211
.060	.259
.080	.298
.100	.333
.150	.406
.200	.466
.250	.519
.300	.566
.350	.609
.400	.649
.450	.685
.500	.719
.550	.751
.600	.781
.700	.836
.800	.886
.900	.932
1.000	.974
1.500	1.141
2.000	1.258
2.500	1.343
3.000	1.403
3.500	1.445
4.000	1.472
4.500	1.488
5.000	1.497
5.500	1.500

Table 4. Summary of Curve Fits of Lift and Drag Data From the Langley 8-Foot Transonic Pressure Tunnel

Run	Wing (a)	Attitude (b)	Grit (c)	M_∞	R_c	α_0, deg	C_{L_α}, deg^{-1}	Error in first curve fit, rms (d)	$C_{L,\min}$	$C_{D,\min}$	$C_{D,0}$	e^*	Error in second curve fit, rms (e)	e	Error in third curve fit, rms (f)
3	A	U	F	0.5	2.1×10^6	−3.44	0.0899	0.0013	0.0658	0.00921	0.0095	0.789	0.00008	0.979	0.00006
4				.3	1.5	−3.50	.0830	.0015	.0582	.00940	.0096	.787	.00010	.952	.00004
5				.4	2.1	−3.49	.0856	.0017	.0621	.00916	.0094	.801	.00005	.971	.00005
7				.3	→	−3.51	.0843	.0013	.0597	.00923	.0095	.808	.00007	.984	.00008
8				.3		−3.50	.0843	.0012	.0631	.00909	.0094	.799	.00005	.997	.00007
17	A	U	B	0.5	2.1×10^6	−3.11	0.0873	0.0005	0.0130	0.01255	0.0126	0.924	0.00003	0.965	0.00004
18				.3	1.5	−3.18	.0808	.0008	.0090	.01293	.0129	.930	.00004	.956	.00004
19				.4	2.1	−3.17	.0831	.0006	.0123	.01234	.0123	.920	.00004	.956	.00004
20				.3		−3.20	.0816	.0010	.0101	.01227	.0123	.933	.00004	.961	.00005
22				.3		−3.22	.0826	.0009	.0129	.01252	.0125	.945	.00005	.982	.00007
27		I		.5		−3.11	.0873	.0004	.0201	.01254	.0126	.899	.00004	.961	.00006
28		I		.3		−3.22	.0819	.0008	.0149	.01219	.0122	.921	.00004	.969	.00004
31		U		.5		−3.11	.0873	.0007	.0121	.01250	.0125	.928	.00004	.965	.00004
32		U		.3		−3.22	.0818	.0007	.0060	.01217	.0122	.949	.00003	.969	.00003
37	C	U	B	0.5	2.1×10^6	−3.24	0.0882	0.0013	0.0195	0.01251	0.0125	0.933	0.00005	0.984	0.00006
38				.3	1.5	−3.29	.0818	.0012	.0046	.01261	.0126	.951	.00007	.963	.00009
39				.4	2.1	−3.30	.0841	.0011	.0143	.01234	.0123	.948	.00002	.987	.00003
40				.3		−3.32	.0825	.0009	.0068	.01220	.0122	.966	.00003	.984	.00003
42				.3		−3.34	.0824	.0012	.0099	.01232	.0123	.961	.00003	.987	.00004
45		I		.5		−3.25	.0882	.0013	.0300	.01235	.0124	.897	.00007	.991	.00007
46		I		.3		−3.36	.0825	.0013	.0241	.01216	.0122	.930	.00006	1.002	.00007
49	C	U	M	0.5	2.1×10^6	−3.25	0.0882	0.0014	0.0240	0.01254	0.0126	0.930	0.00004	1.000	0.00005
52	A	U	M	0.5	2.1×10^6	−3.12	0.0872	0.0010	0.0134	0.01245	0.0125	0.930	0.00004	0.966	0.00002
54				.4	→	−3.18	.0832	.0007	.0096	.01222	.0122	.940	.00004	.966	.00003
55				.3		−3.22	.0819	.0007	.0044	.01213	.0121	.968	.00005	.982	.00005
61	B	U	M	0.5	2.1×10^6	−3.17	0.0893	0.0007	0.0219	0.01245	0.0125	0.945	0.00004	1.008	0.00005
62				.3	1.5	−3.23	.0826	.0009	.0089	.01272	.0127	.977	.00005	.999	.00006
63				.4	2.1	−3.23	.0848	.0011	.0186	.01215	.0122	.946	.00004	.998	.00005
64				.3	2.1	−3.26	.0832	.0016	.0139	.01217	.0122	.979	.00004	1.018	.00006
76	D,s	U	M	0.5	2.1×10^6	−3.20	0.0903	0.0006	0.0230	0.01388	0.0139	0.914	0.00008	0.974	0.00011
77				.3	1.5	−3.29	.0831	.0008	.0138	.01402	.0140	.930	.00004	.971	.00003
78				.4	2.1	−3.27	.0856	.0010	.0164	.01338	.0134	.923	.00003	.967	.00003
79				.3	2.1	−3.31	.0838	.0011	.0119	.01322	.0132	.942	.00004	.974	.00005
82	D,r	U	M	0.5	2.1×10^6	−3.20	0.0899	0.0008	0.0150	0.01303	0.0130	0.915	0.00004	0.952	0.00005
83				.3	1.5	−3.28	.0828	.0007	.0078	.01328	.0133	.927	.00004	.950	.00005
84				.3	2.1	−3.32	.0834	.0006	.0063	.01259	.0126	.943	.00003	.959	.00004

a Wing: r—round tip; s—square tip.
b Attitude: U—upright; I—inverted.
c Grit: F—free transition; B—baseline; M—modified.
d First curve fit: linear fit of C_L vs. α.
e Second curve fit: fit of C_D vs. $(C_L - C_{L,\min})^2$.
f Third curve fit: fit of C_D vs. C_L^2.
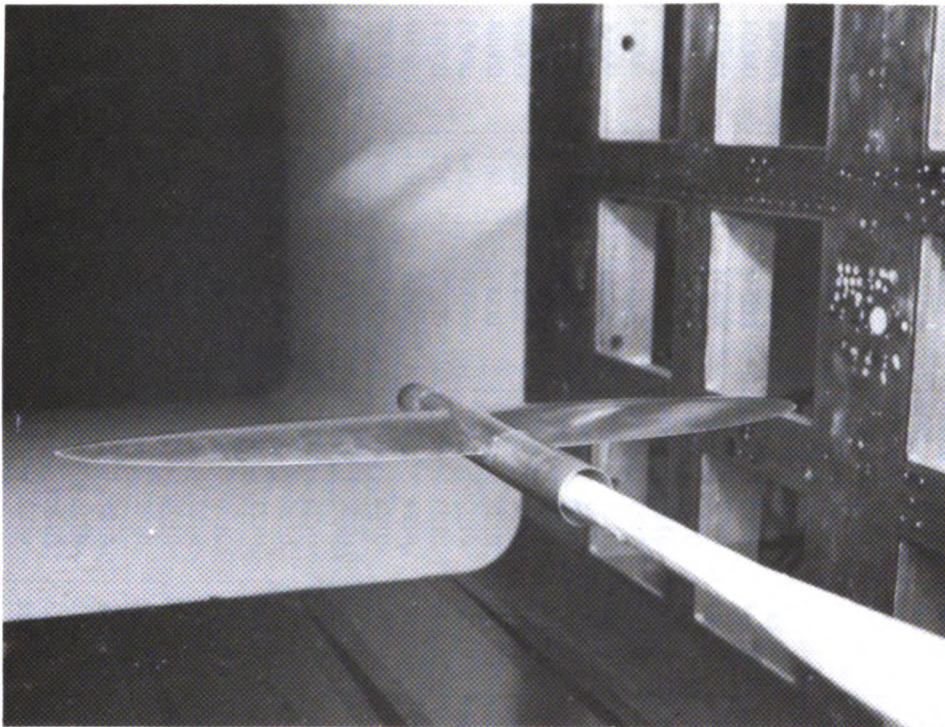
(a) Rear three-quarter view.
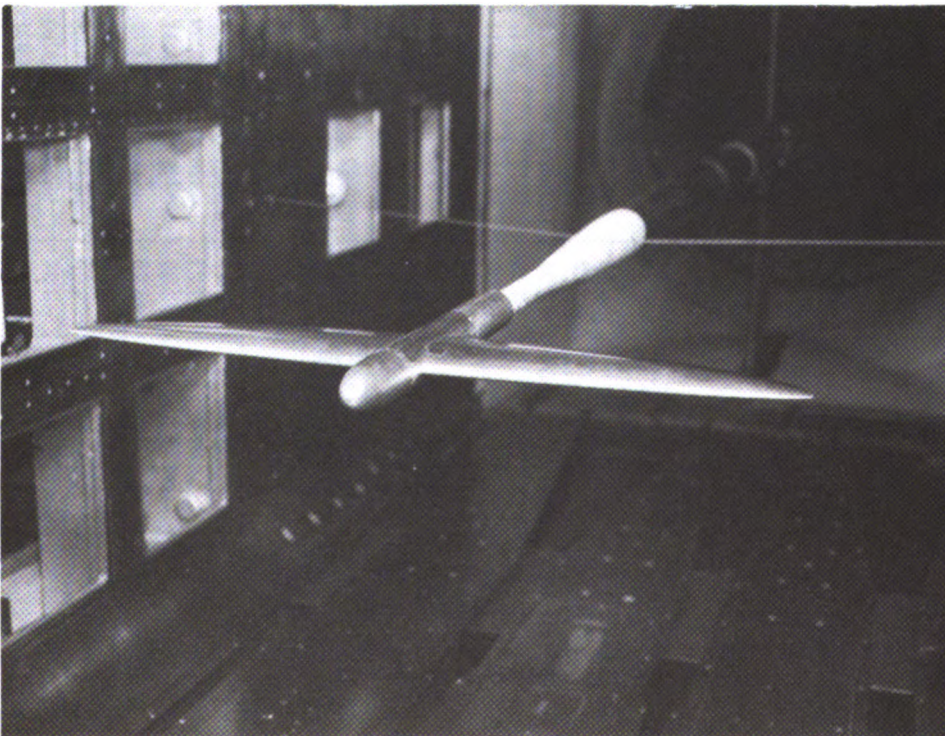
(b) Front three-quarter view.

Figure 1. Photographs of model with wing A installed in the Langley 8-Foot Transonic Pressure Tunnel.
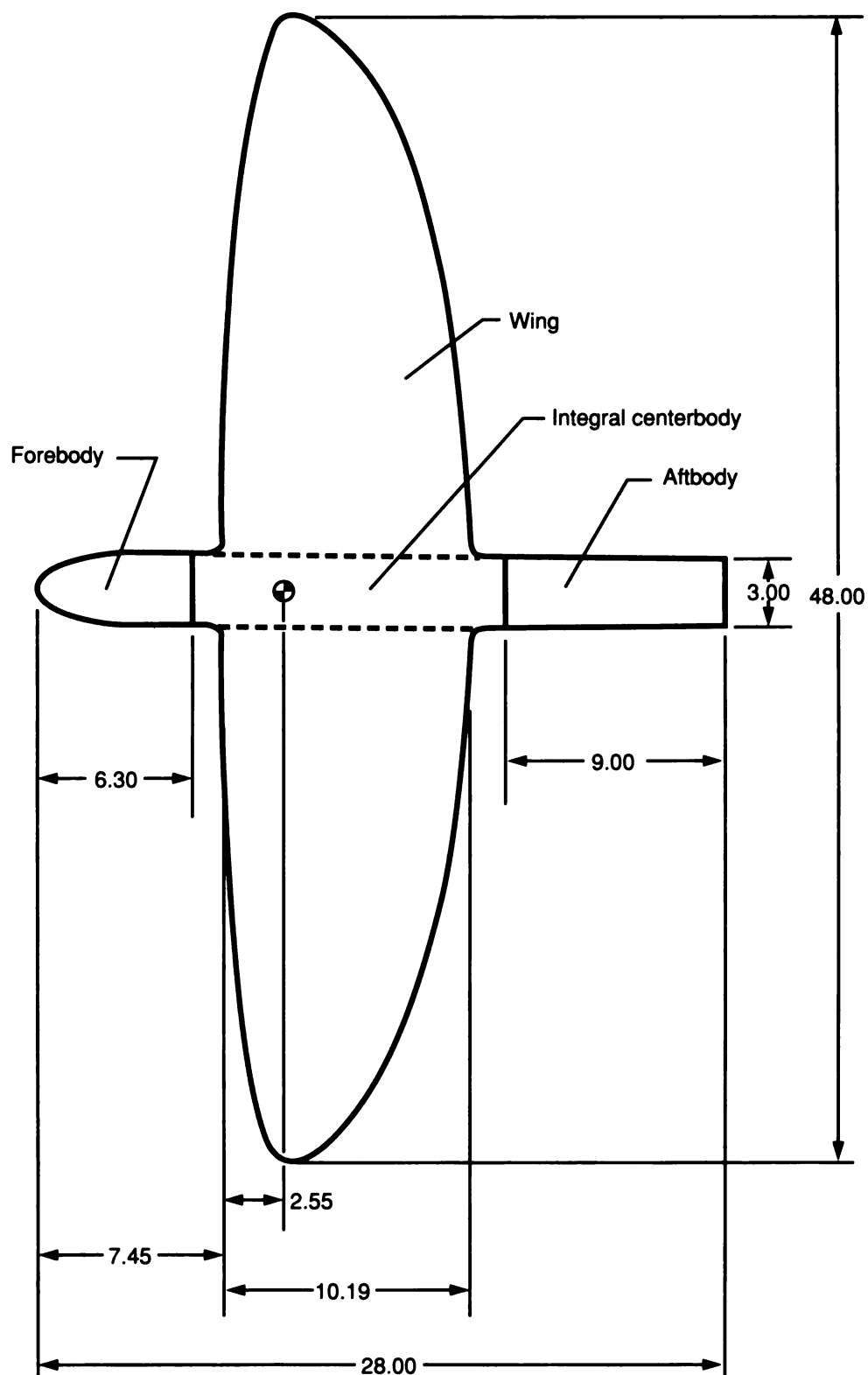
(a) Model components (wing A shown).

Figure 2. Details of model. All dimensions are given in inches.

25
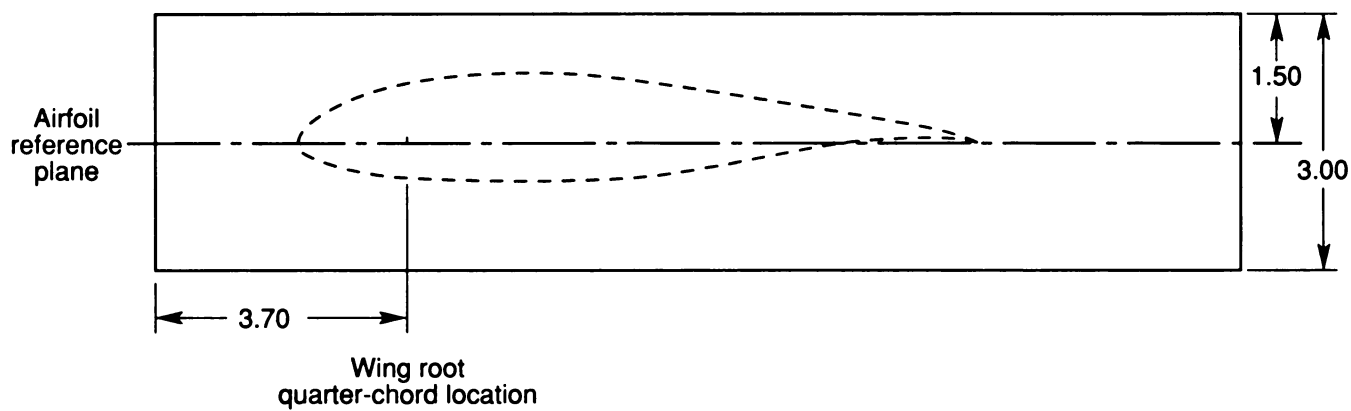
(b) Position of wing on centerbody.
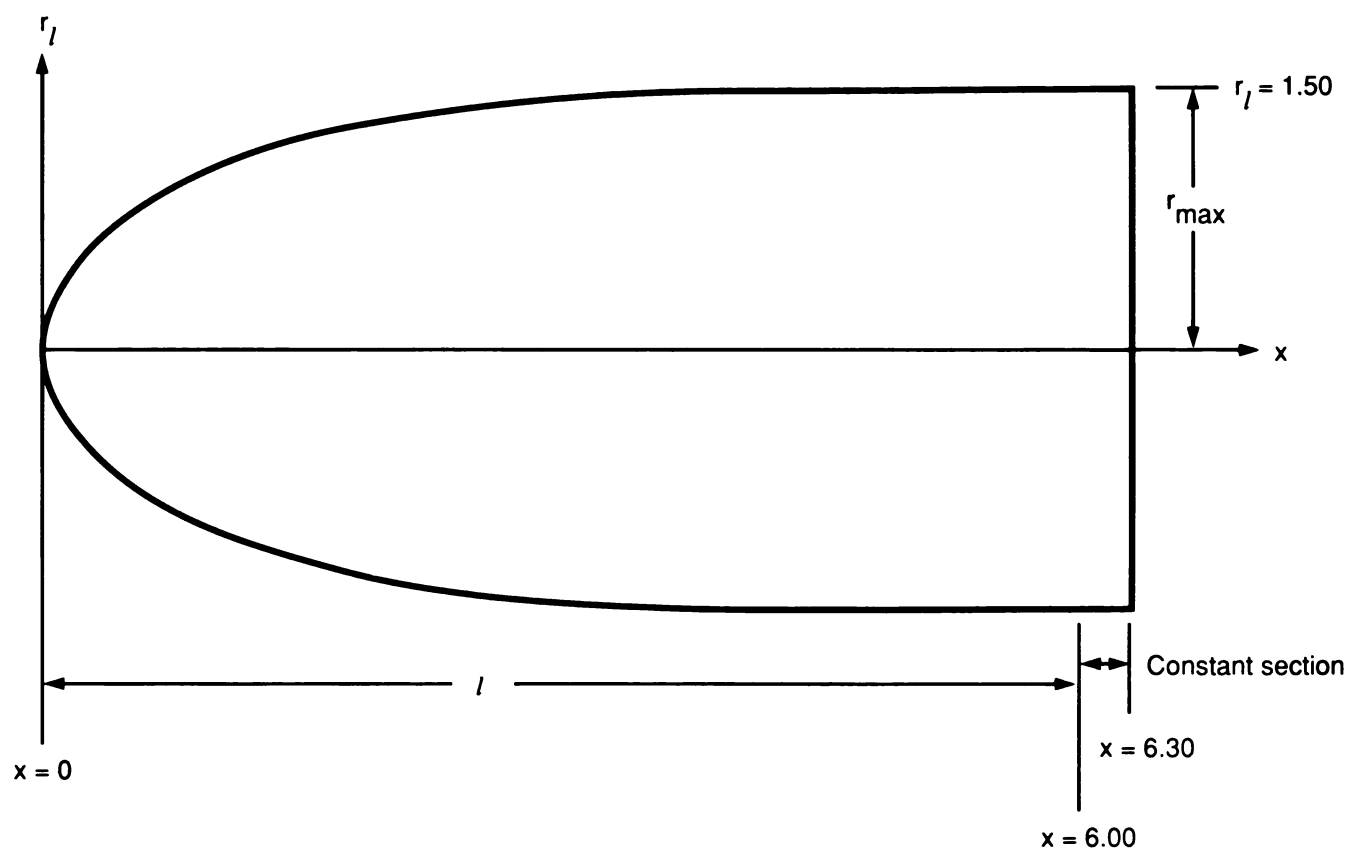
(c) Details of forebody. $\frac{r_l}{r_{\max}} = \left[3 \left(\frac{x}{2} \right) - 3 \left(\frac{x}{2} \right)^2 + \left(\frac{x}{2} \right)^3 \right]^{1/2}$

Figure 2. Concluded.
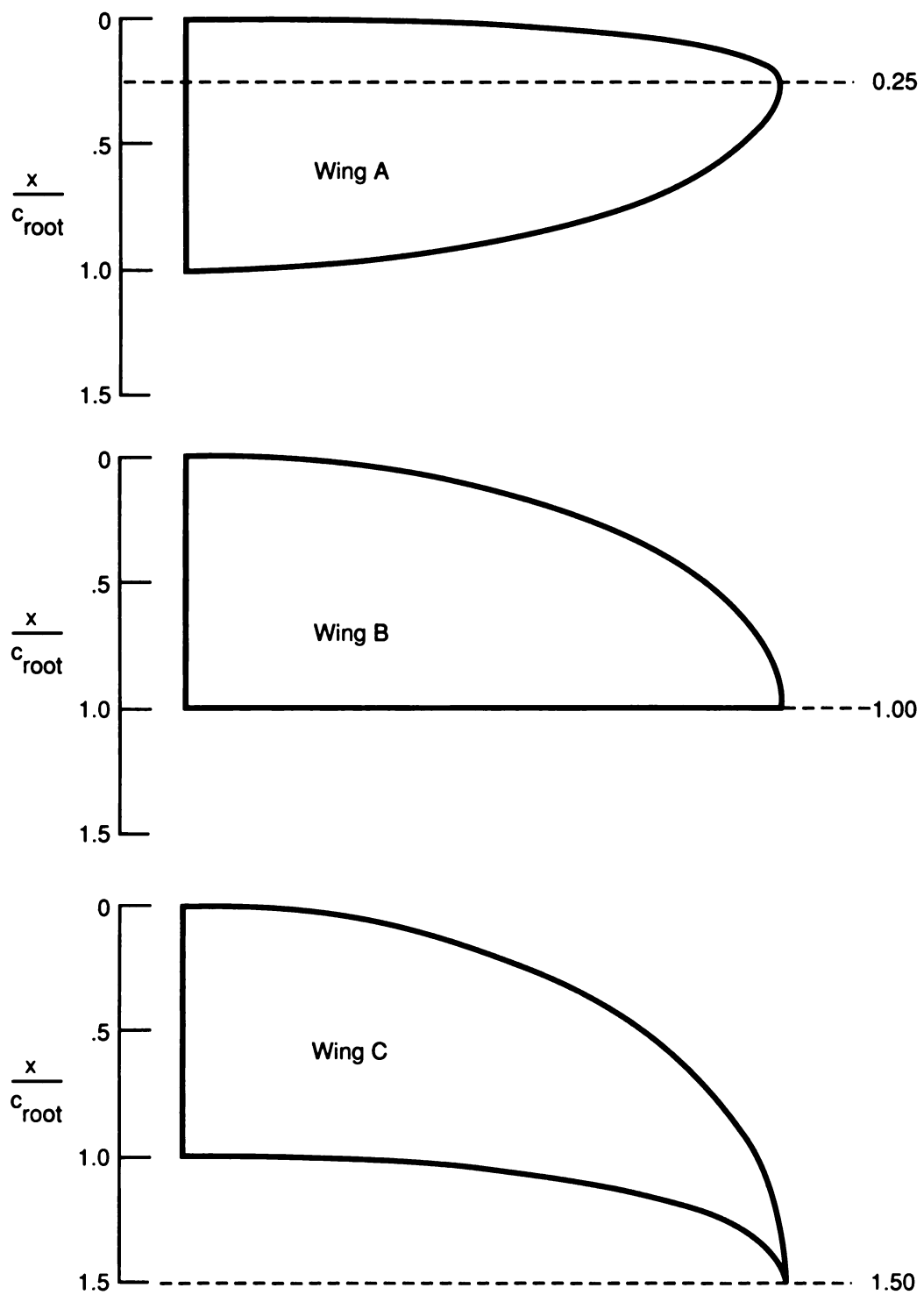
Figure 3. Comparison of elliptical wing planforms.
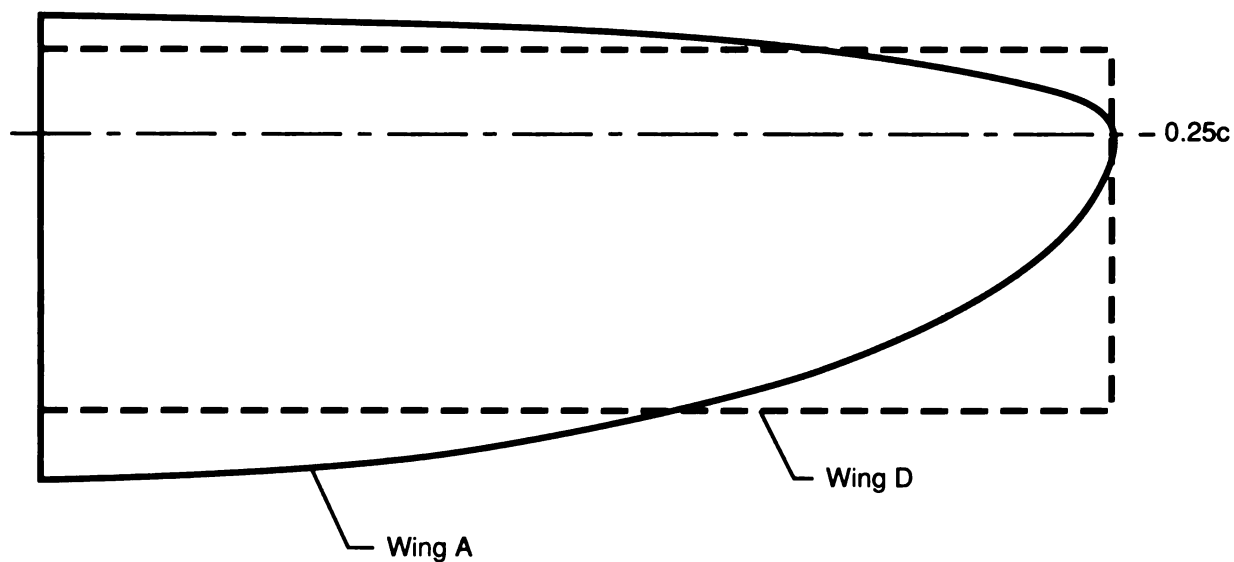
Figure 4. Comparison of planforms of elliptical wing A with rectangular wing D.
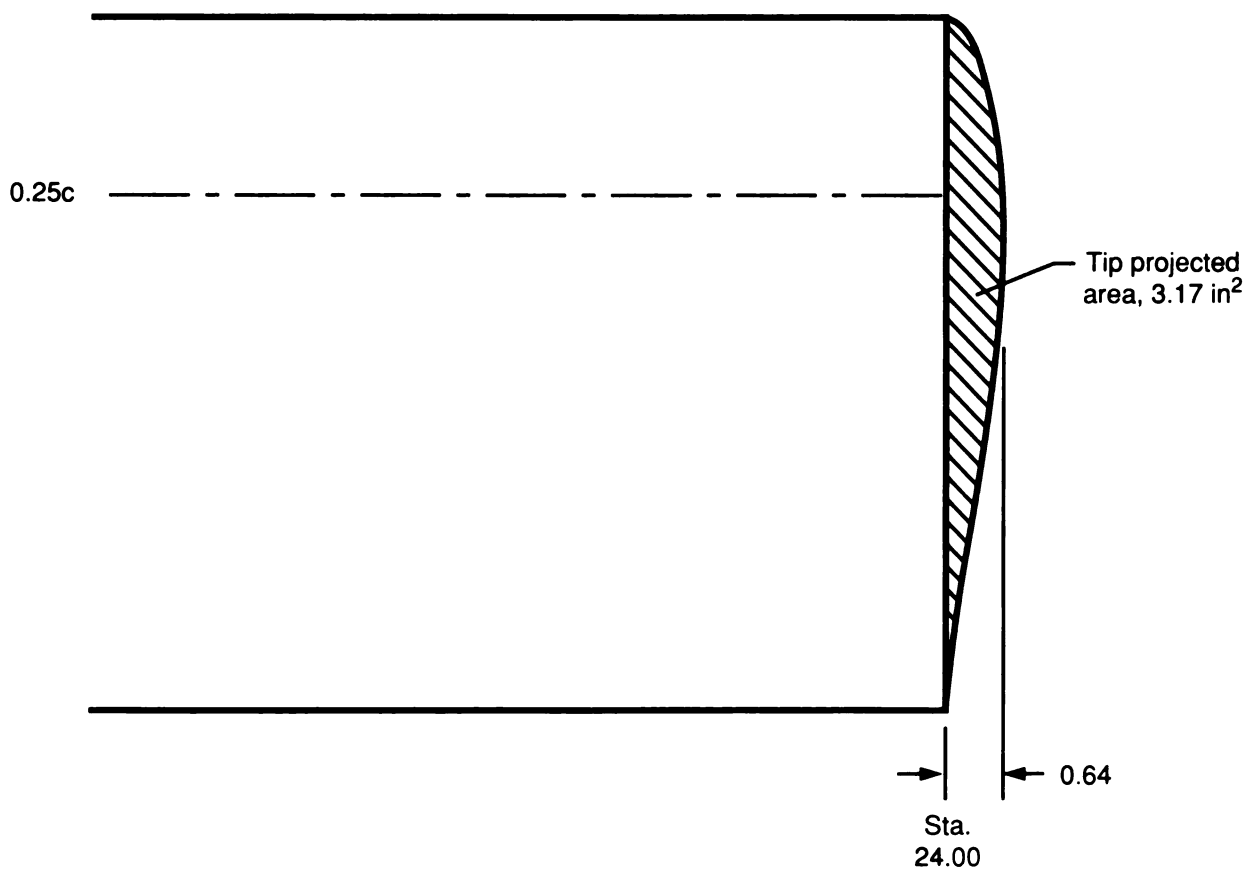
Figure 5. Planform view of round tip superimposed on square tip. All dimensions are given in inches.
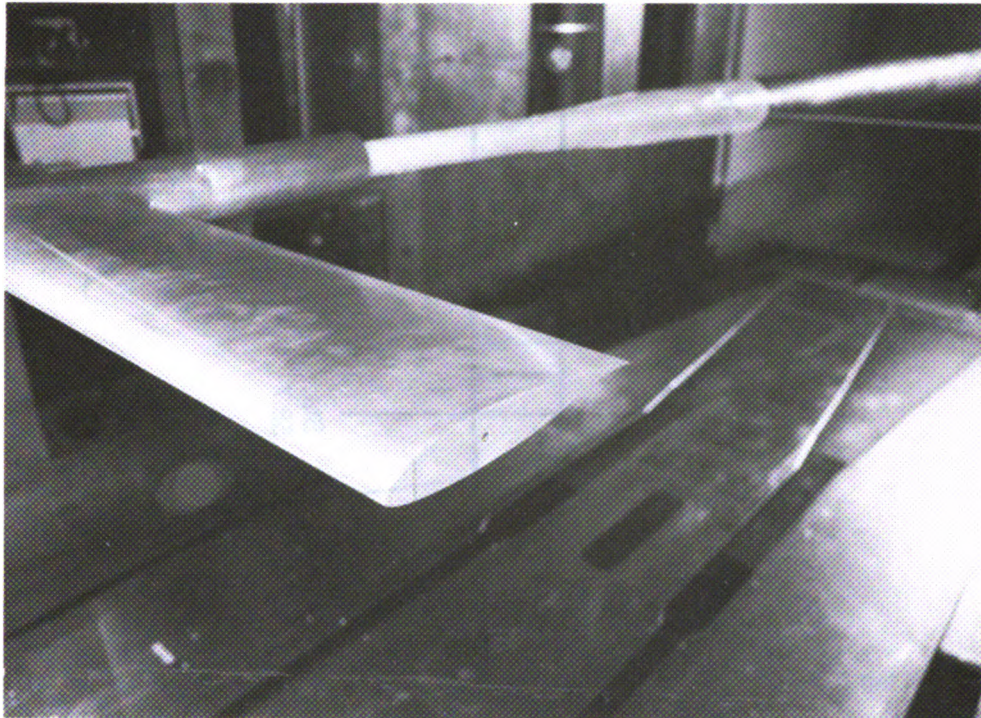
L-90-10713

(a) Square tip.
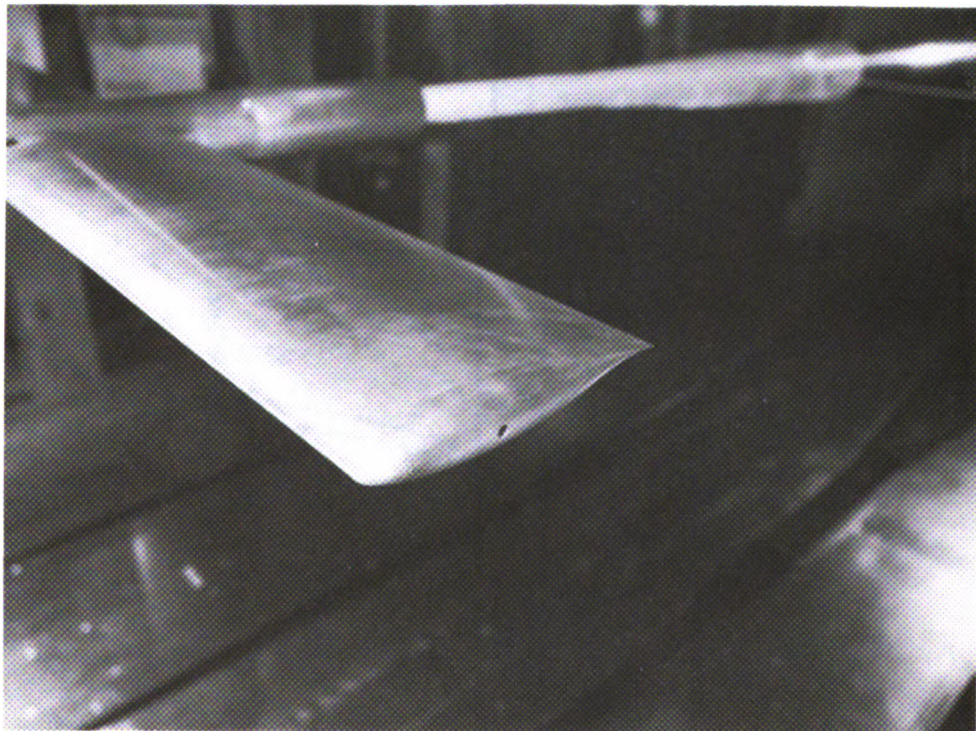
L-90-10709

(b) Round tip.

Figure 6. Photographs of tip region on rectangular wing D.

Center of rotation

Model support

4.00 diam.

Sting

1.95 diam.

1.67 diam.

Model

Moment reference center

Sta. 69.5

Sta. 58.7

Sta. 42.8

Sta. 29.2

Sta. 28.0

Sta. 10.0

Sta. 0

All dimensions are given in inches.
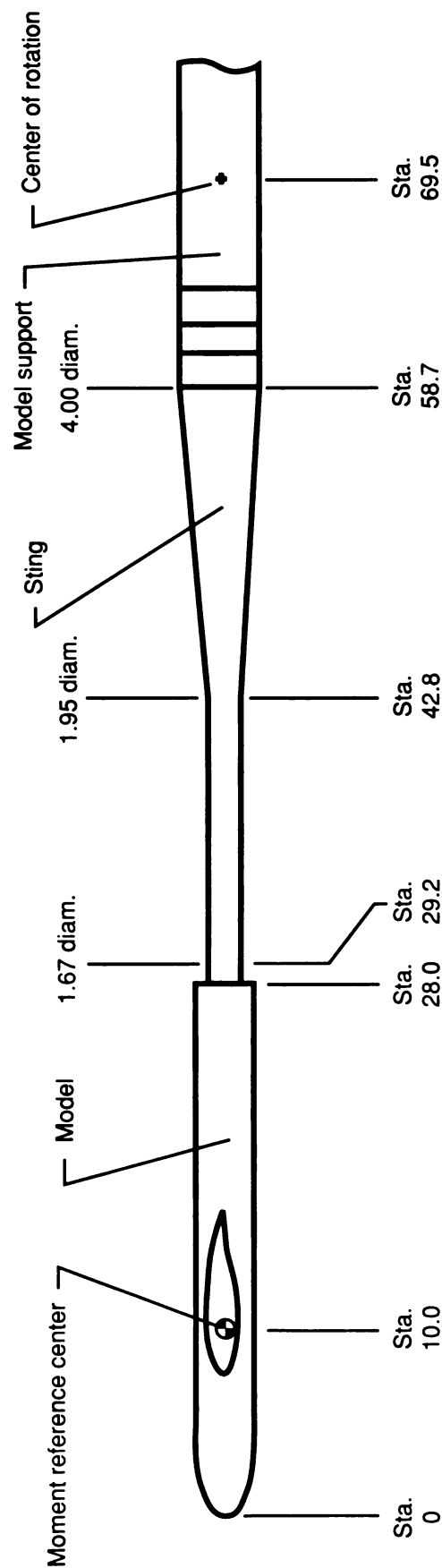
Figure 7. Sketch of model and sting.
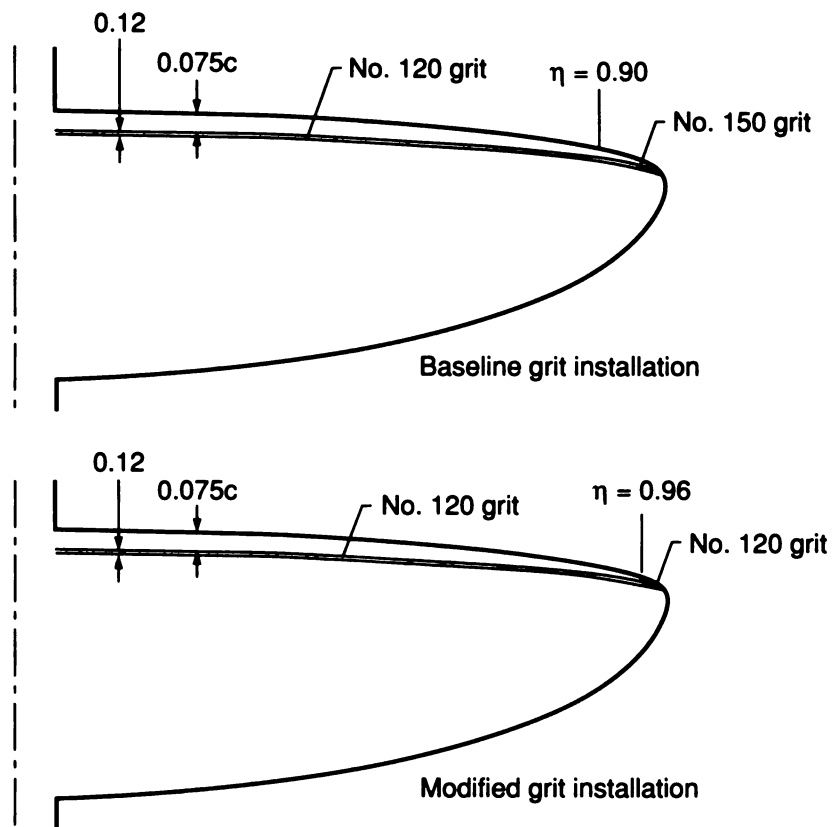
(a) Wing A.
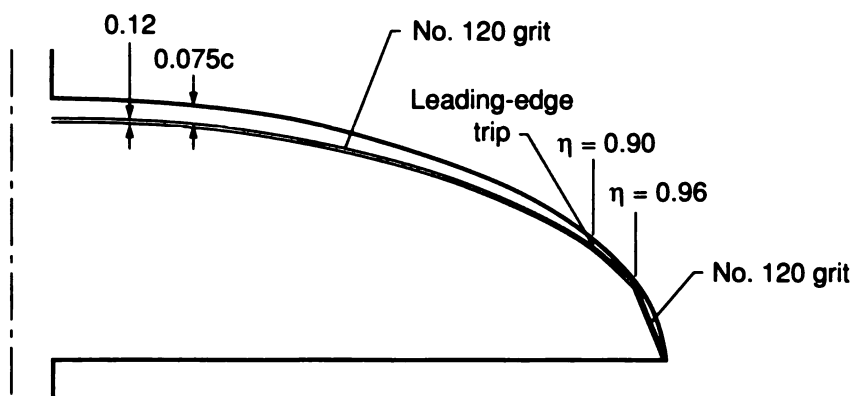
(b) Wing B.

Figure 8. Location of transition grit on wings. All dimensions are given in inches.

0.12
0.075c
No. 120 grit
η = 0.75
η = 0.90
No. 150 grit
Baseline grit installation

0.12
0.075c
No. 120 grit
η = 0.75
Leading-edge trip
η = 0.94
No. 120 grit
Modified grit installation

(c) Wing C.

0.12
0.075c
No. 120 grit
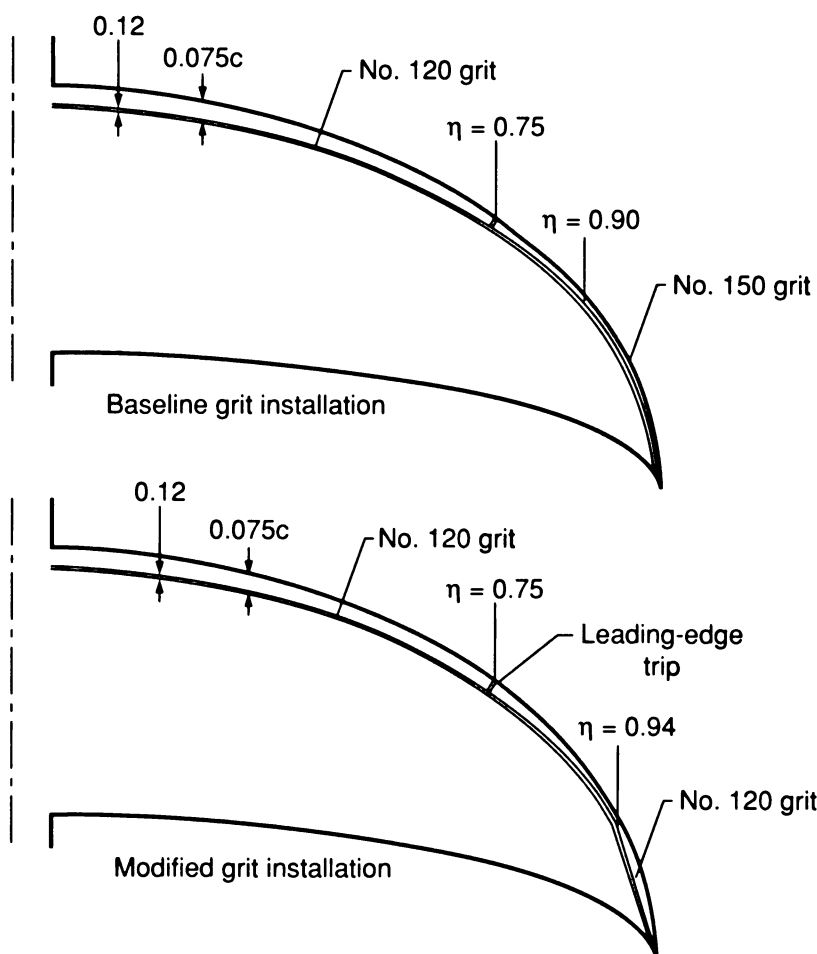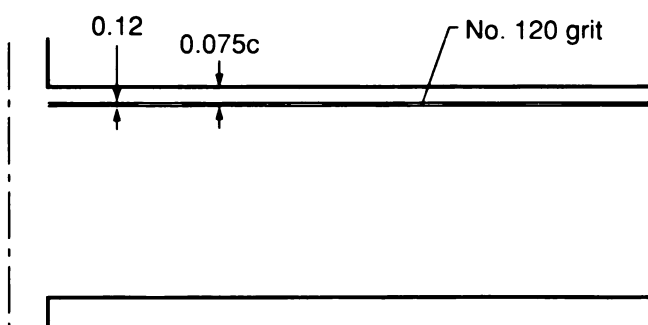
(d) Wing D.

Figure 8. Concluded.

	Run	Grit
O	31	Baseline
□	52	Modified
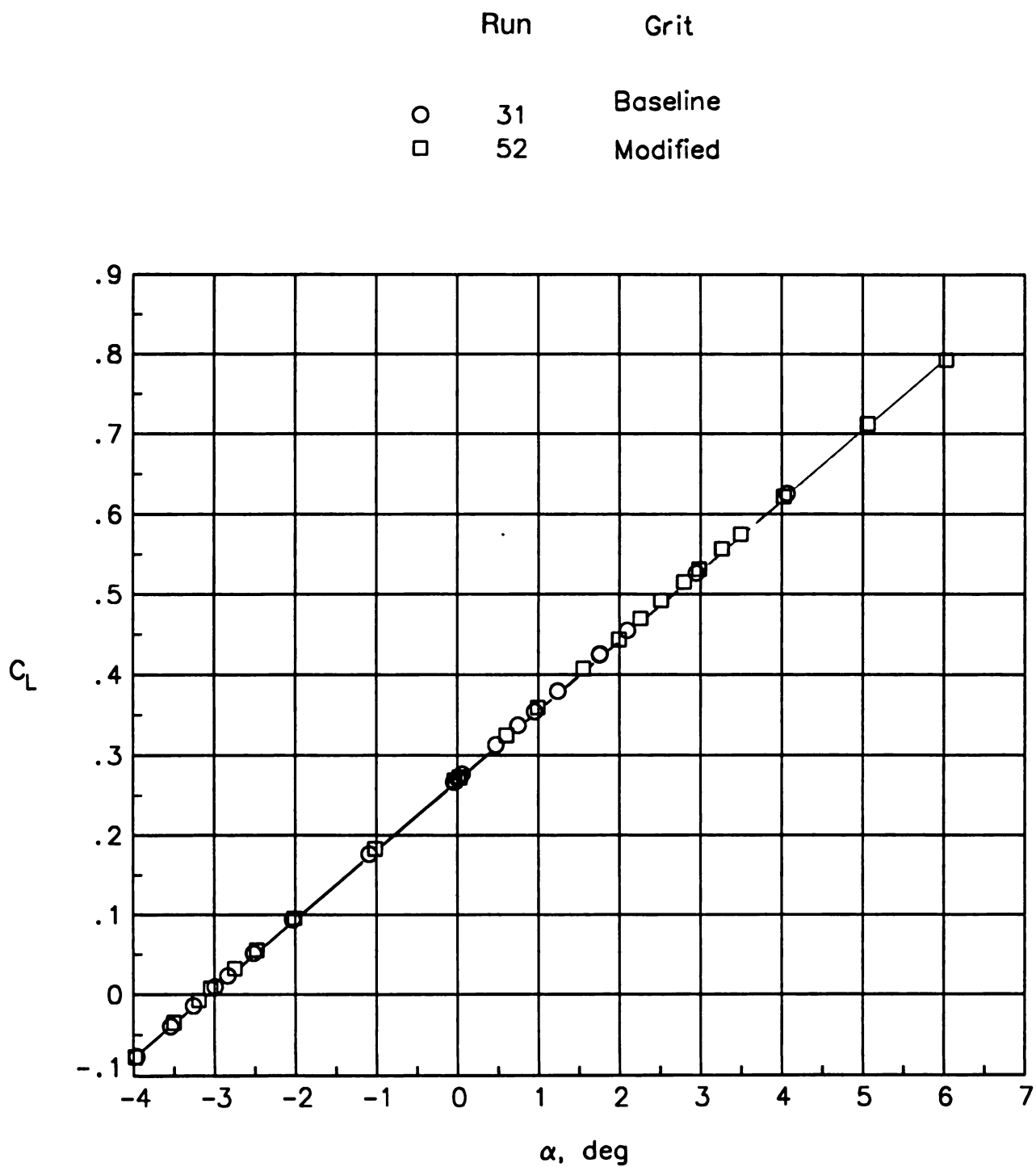
(a) Variation of lift with angle of attack.

Figure 9. Effect of grit location near tip of wing A. $M_\infty = 0.5$; $R_c = 2.1 \times 10^6$.

	Run	Grit
O	31	Baseline
□	52	Modified
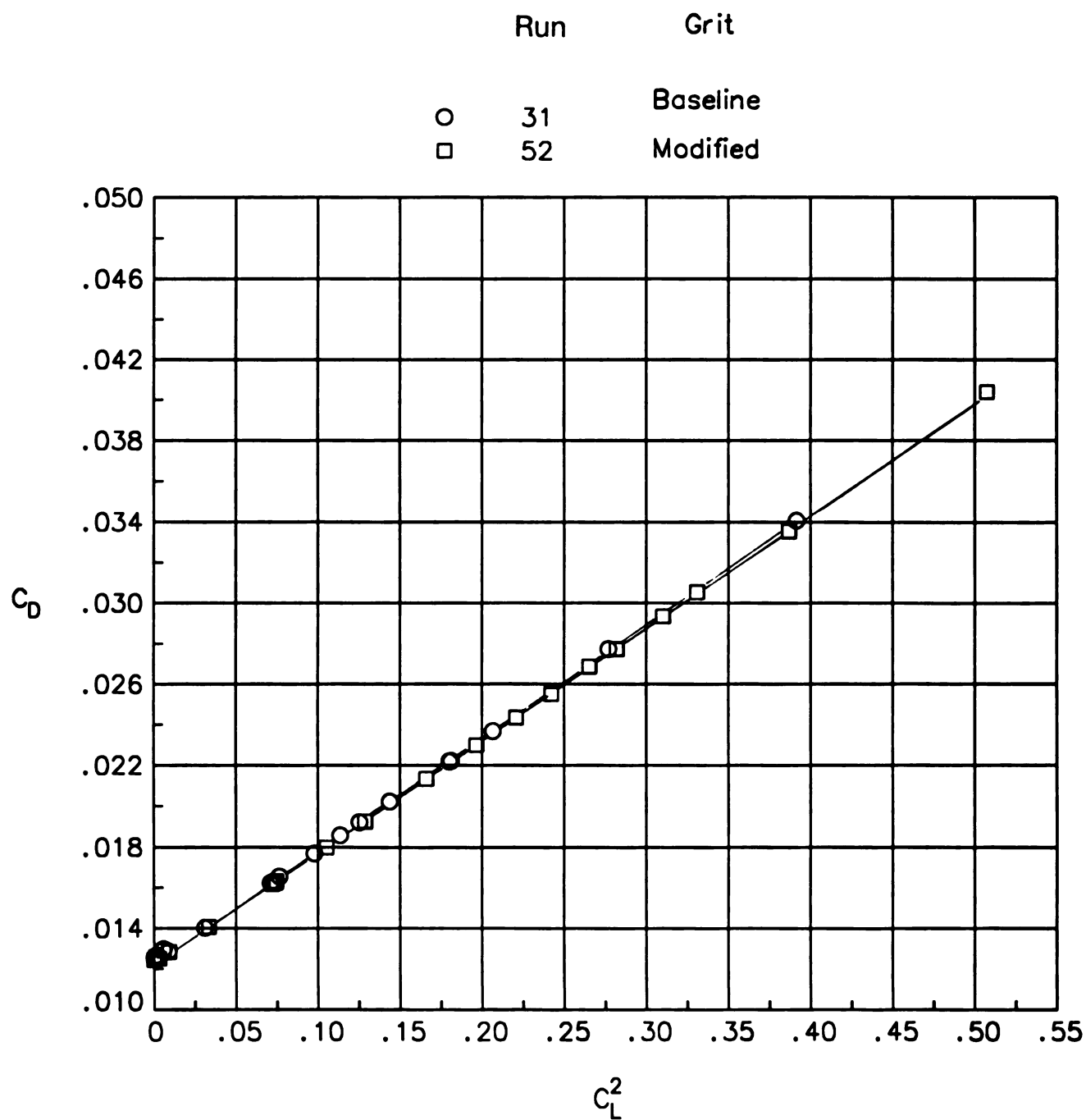
(b) Variation of drag with lift squared.

Figure 9. Continued.

	Run	Grit
O	31	Baseline
□	52	Modified
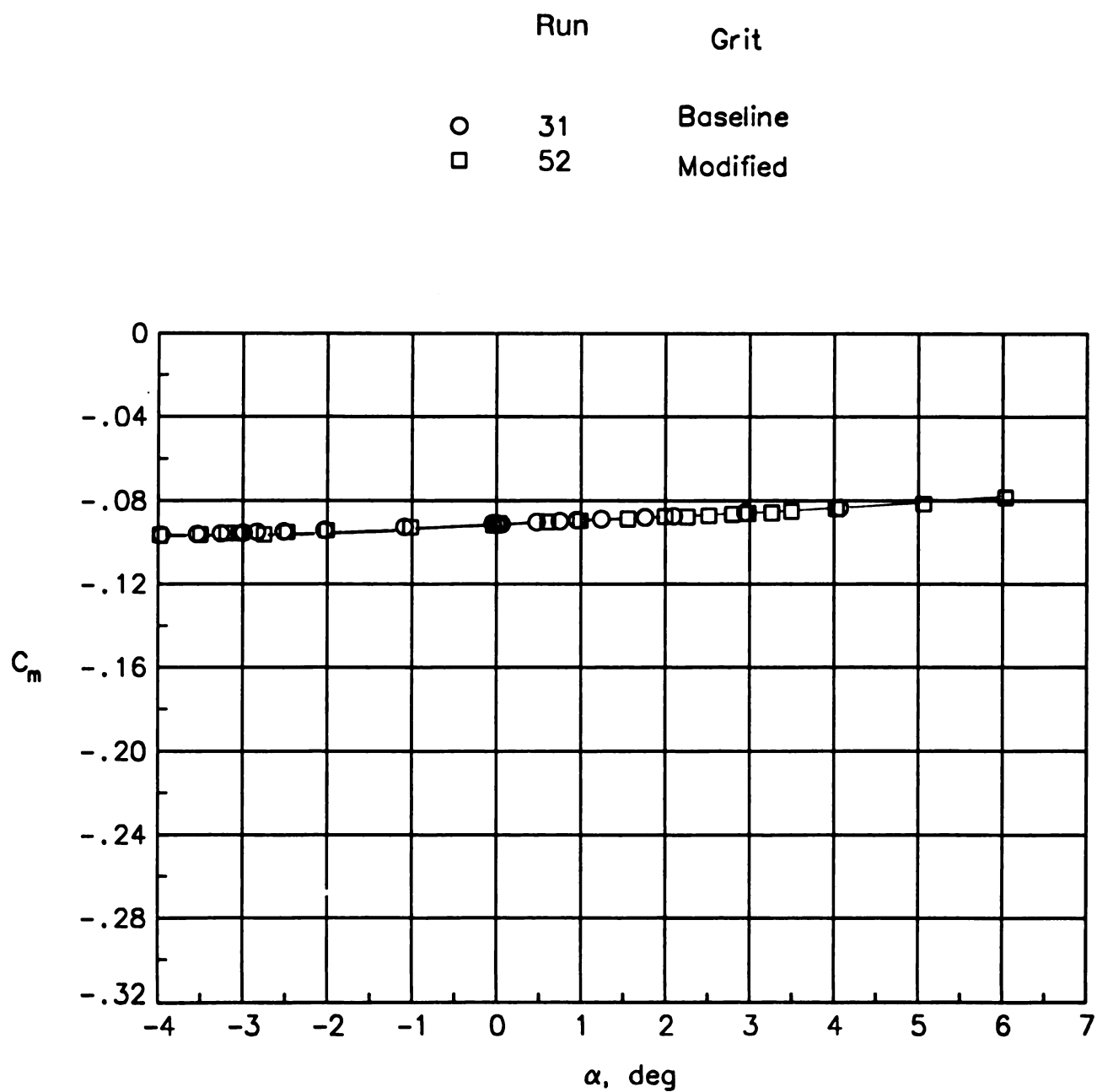
(c) Variation of pitching moment with angle of attack.

Figure 9. Concluded.
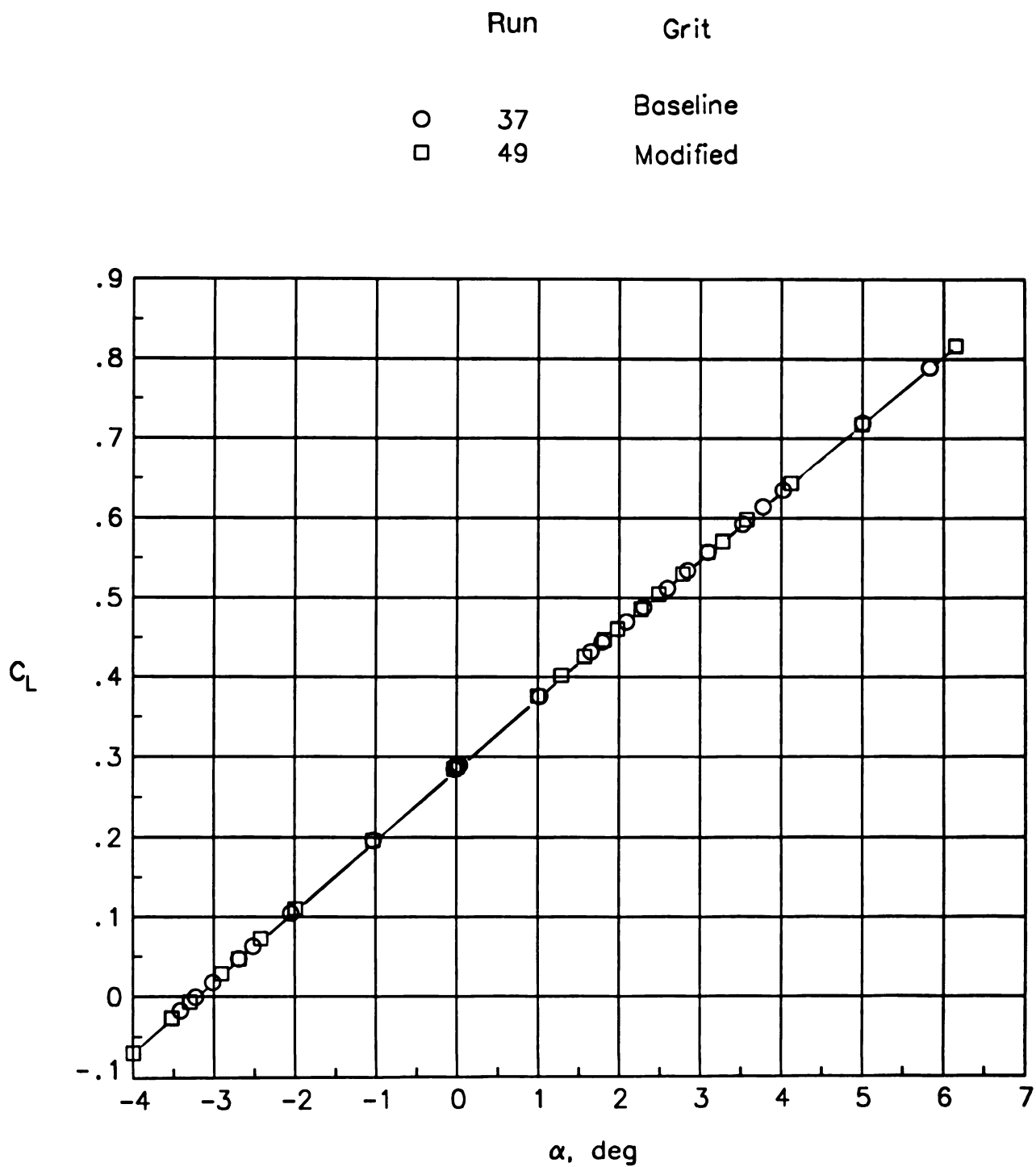
(a) Variation of lift with angle of attack.

Figure 10. Effect of grit location near tip of wing C. $M_\infty = 0.5$; $R_c = 2.1 \times 10^6$.
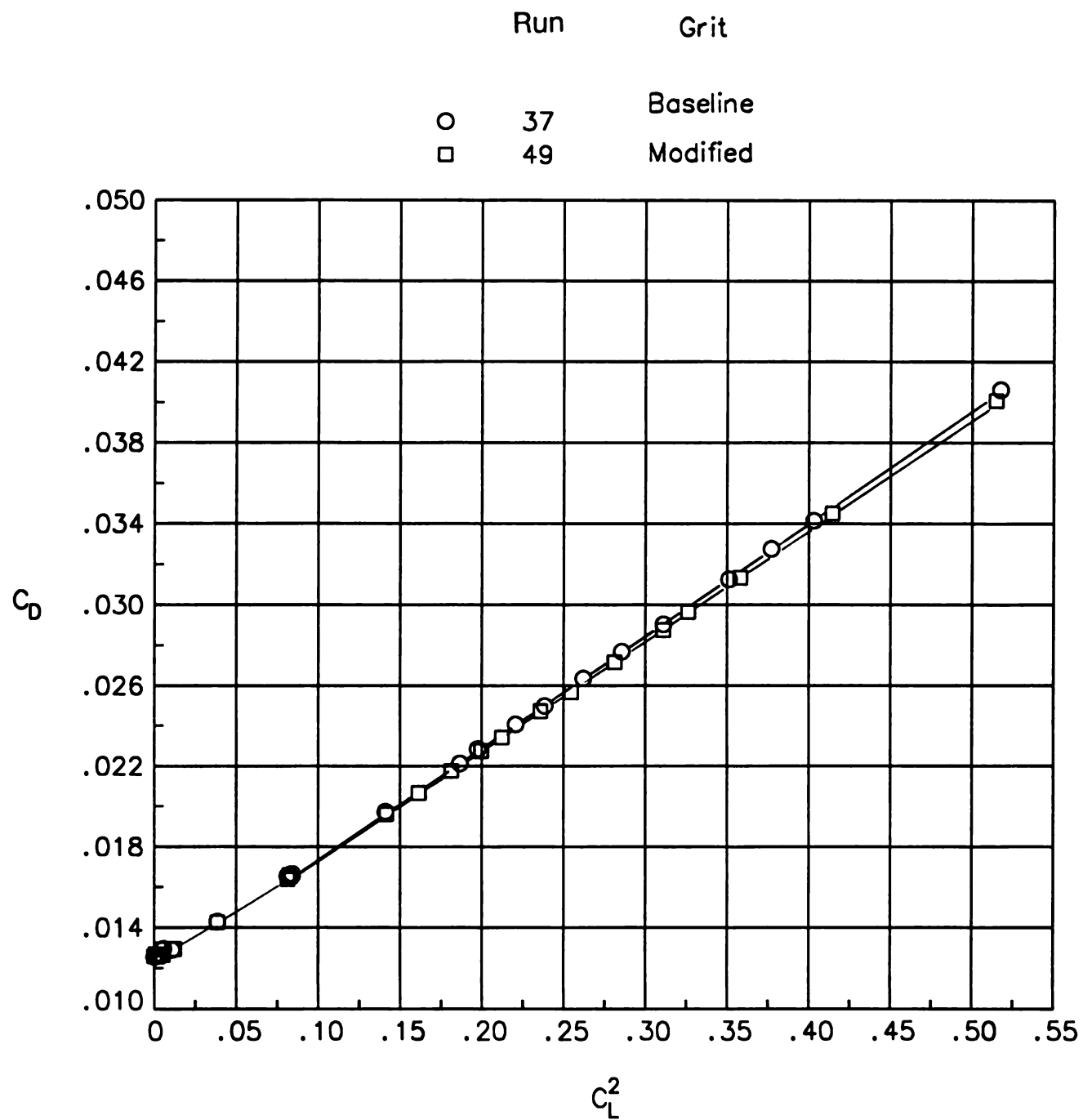
(b) Variation of drag with lift squared.

Figure 10. Continued.
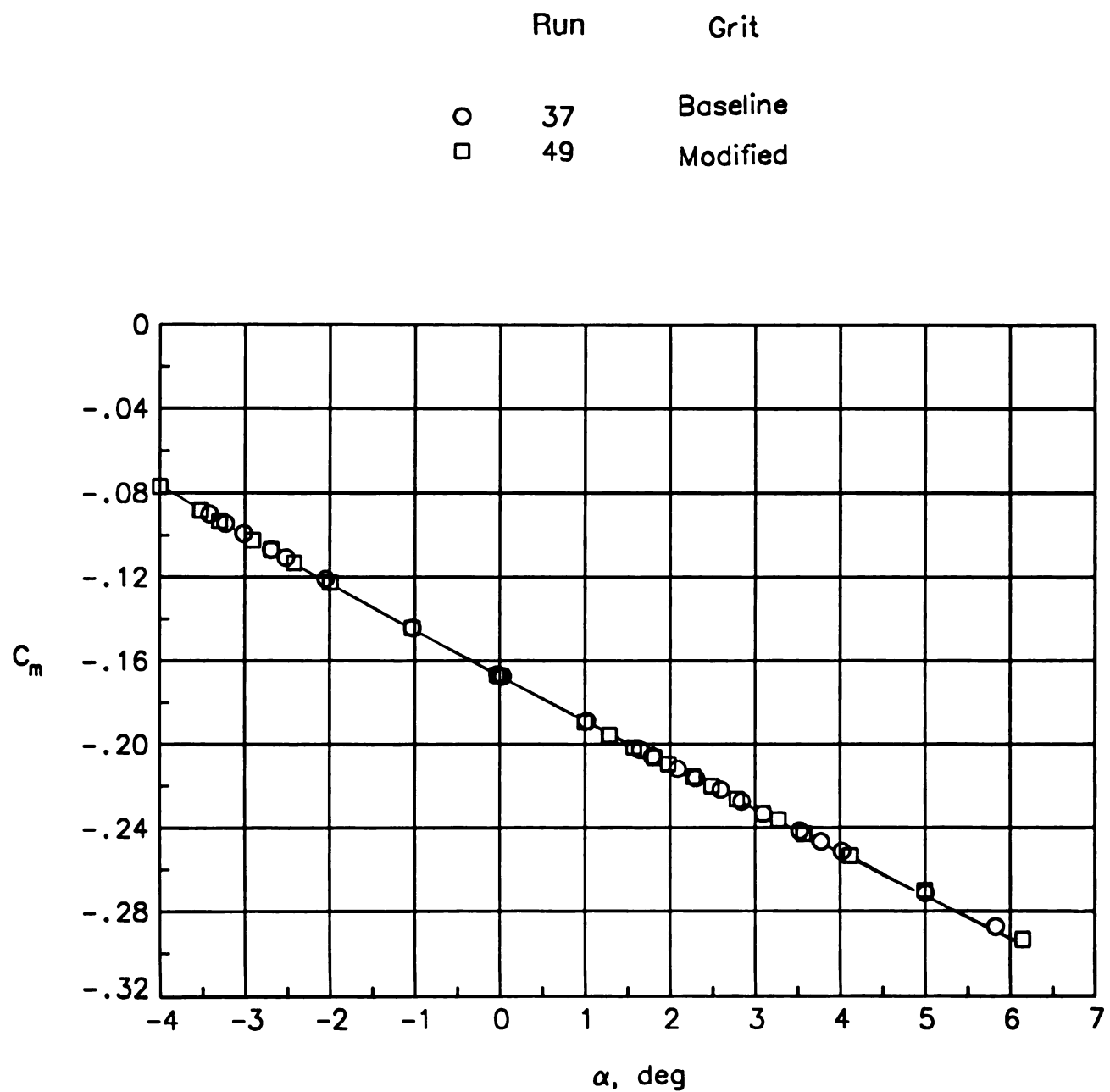
(c) Variation of pitching moment with angle of attack.

Figure 10. Concluded.

	Run	Attitude	α_0, deg	C_{L_α}, deg^{-1}
O	20	Upright	−3.20	.0816
□	22	Inverted	−3.22	.0826
◇	28	Upright	−3.22	.0819
△	32	Upright	−3.22	.0818
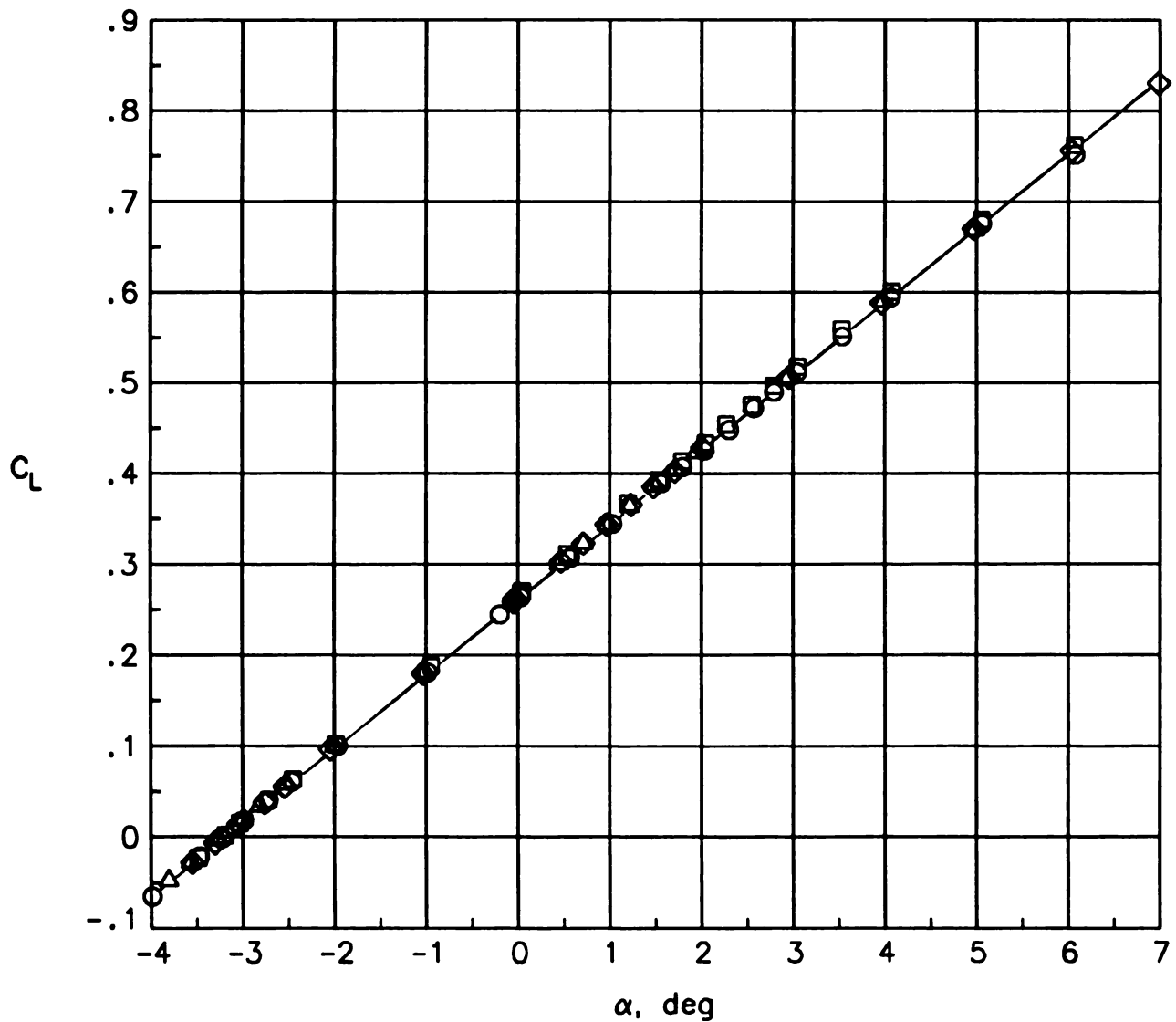
(a) Variation of C_L with α.

Figure 11. Data repeatability for wing A. $M_\infty = 0.3$; $R_c = 2.1 \times 10^6$.

	Run	Attitude	$C_{D,0}$	$\dfrac{dC_D}{dC_L^2}$
O	20	Upright	.0123	.0572
□	22	Inverted	.0125	.0561
◇	28	Upright	.0122	.0577
△	32	Upright	.0122	.0569
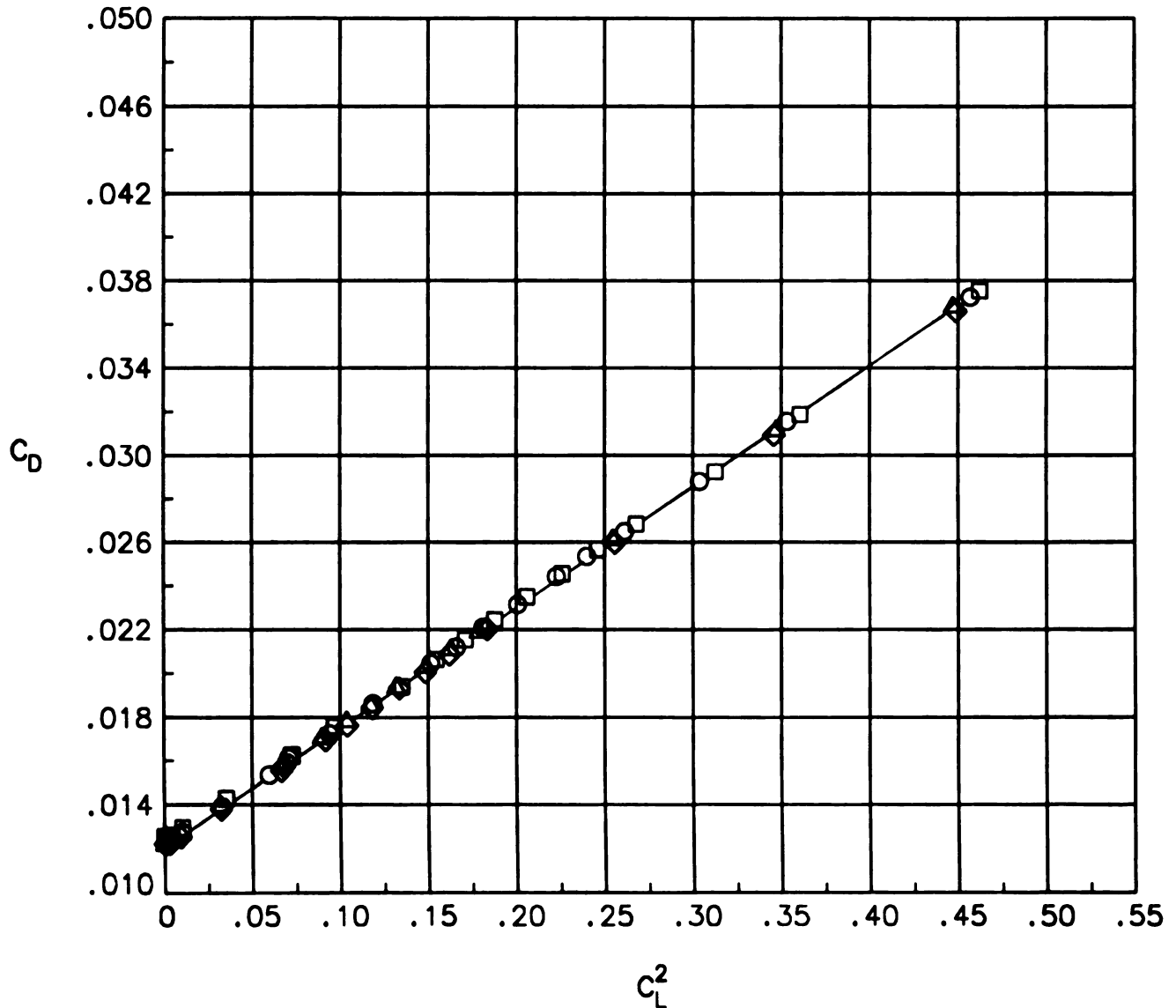
(b) Variation of C_D with C_L^2.

Figure 11. Continued.
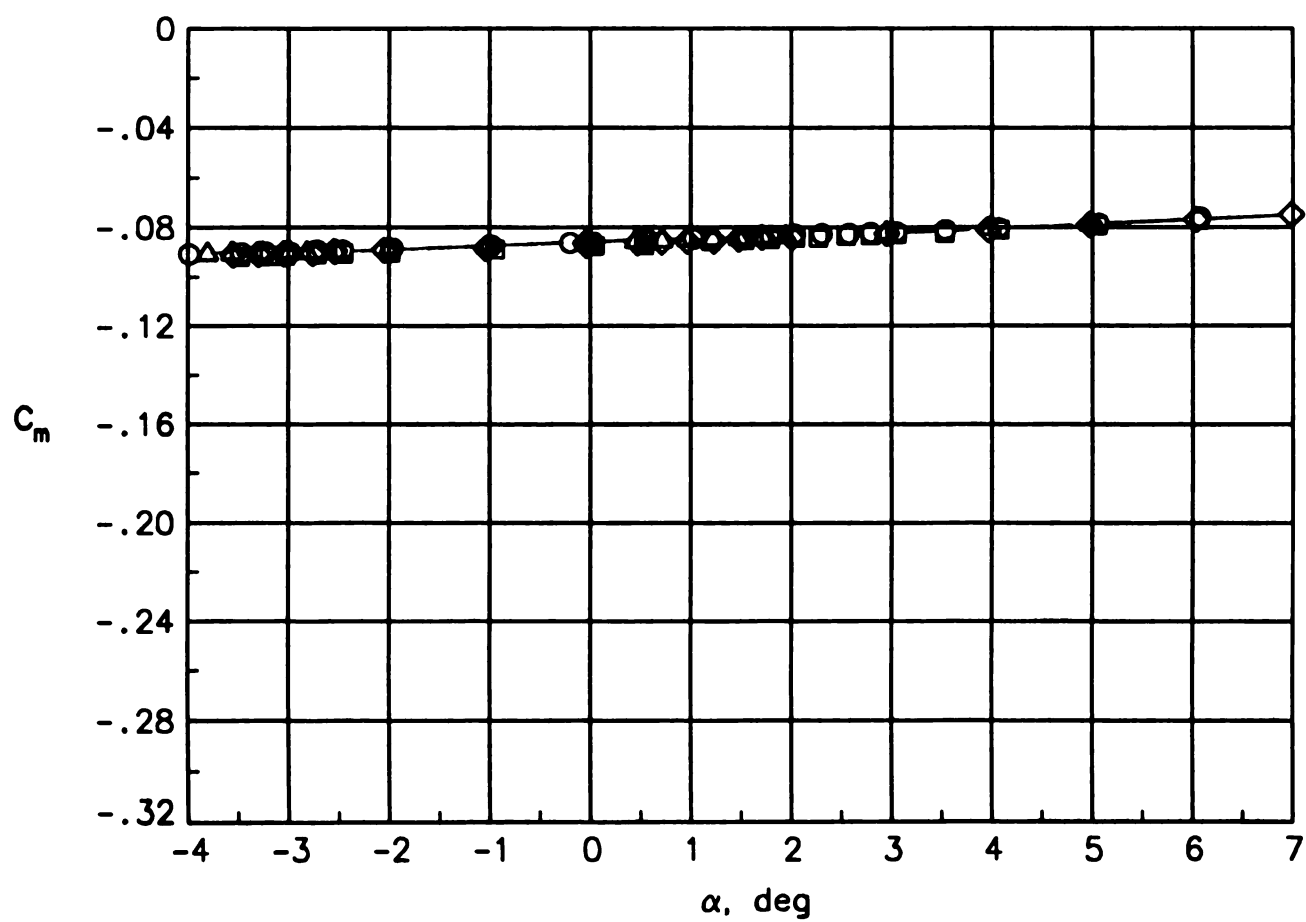
(c) Variation of C_M with α.

Figure 11. Concluded.
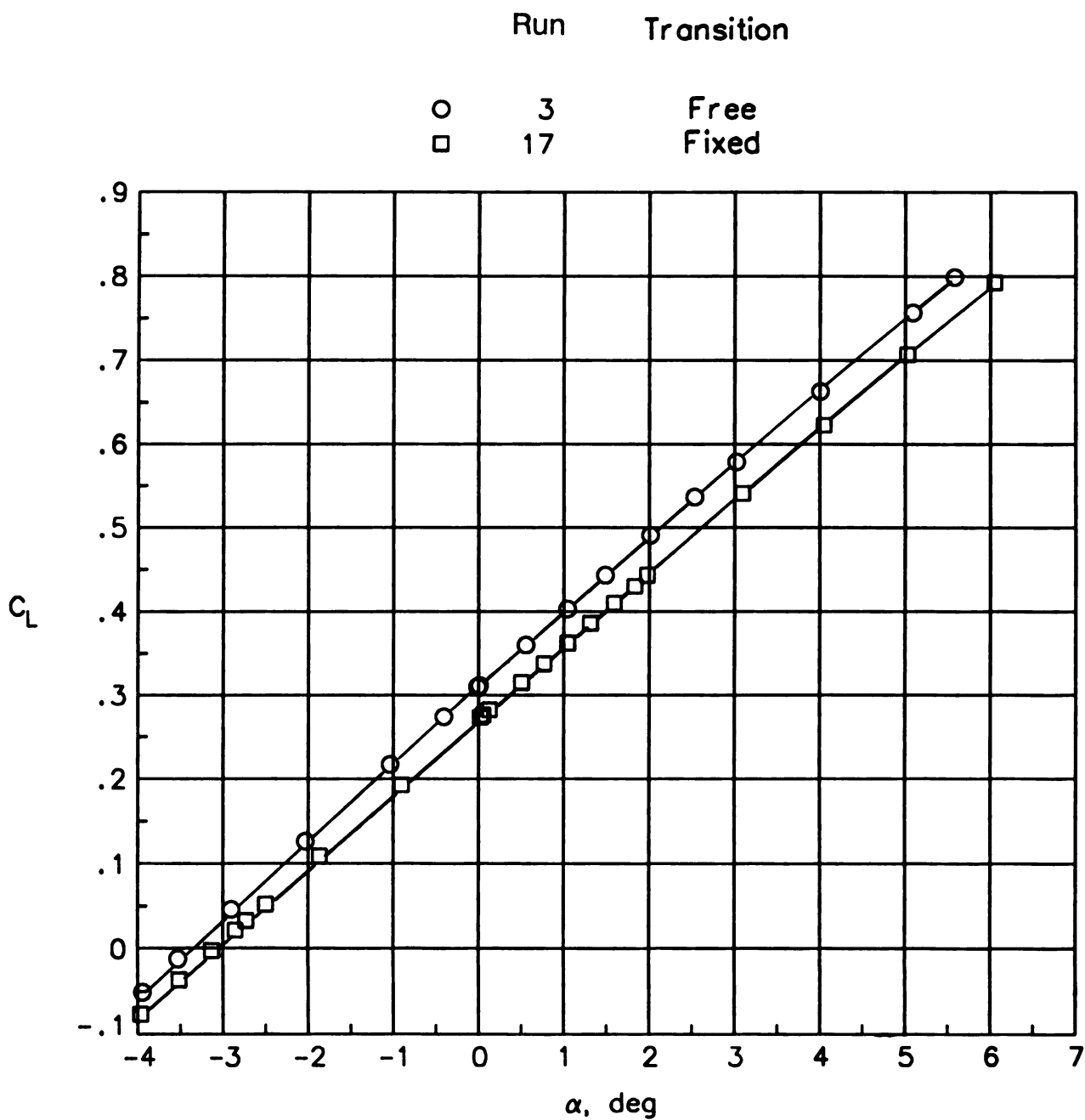
(a) Variation of lift with angle of attack.

Figure 12. Effect of transition on aerodynamic characteristics of wing A. $M_\infty = 0.5$; $R_c = 2.1 \times 10^6$.
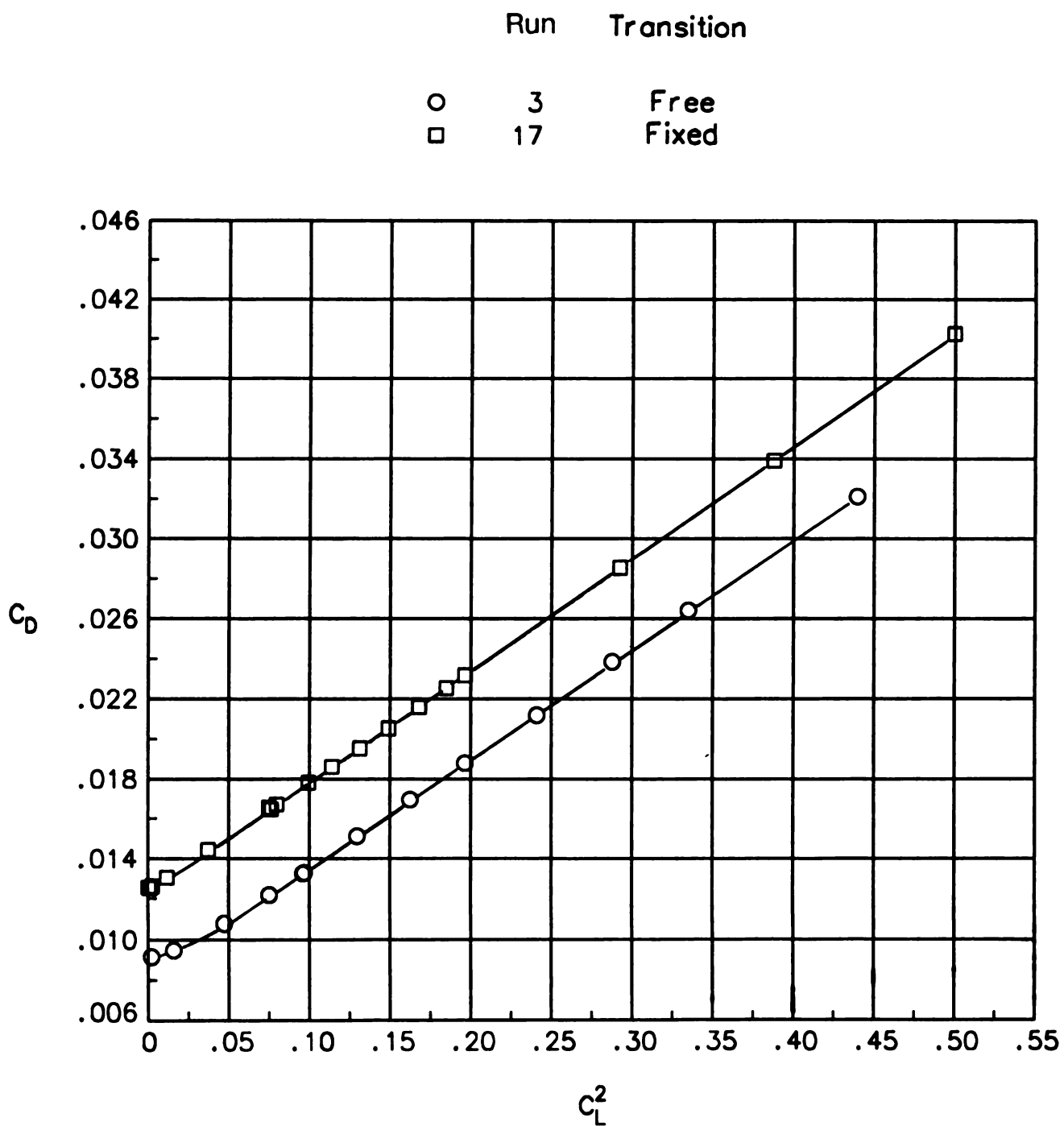
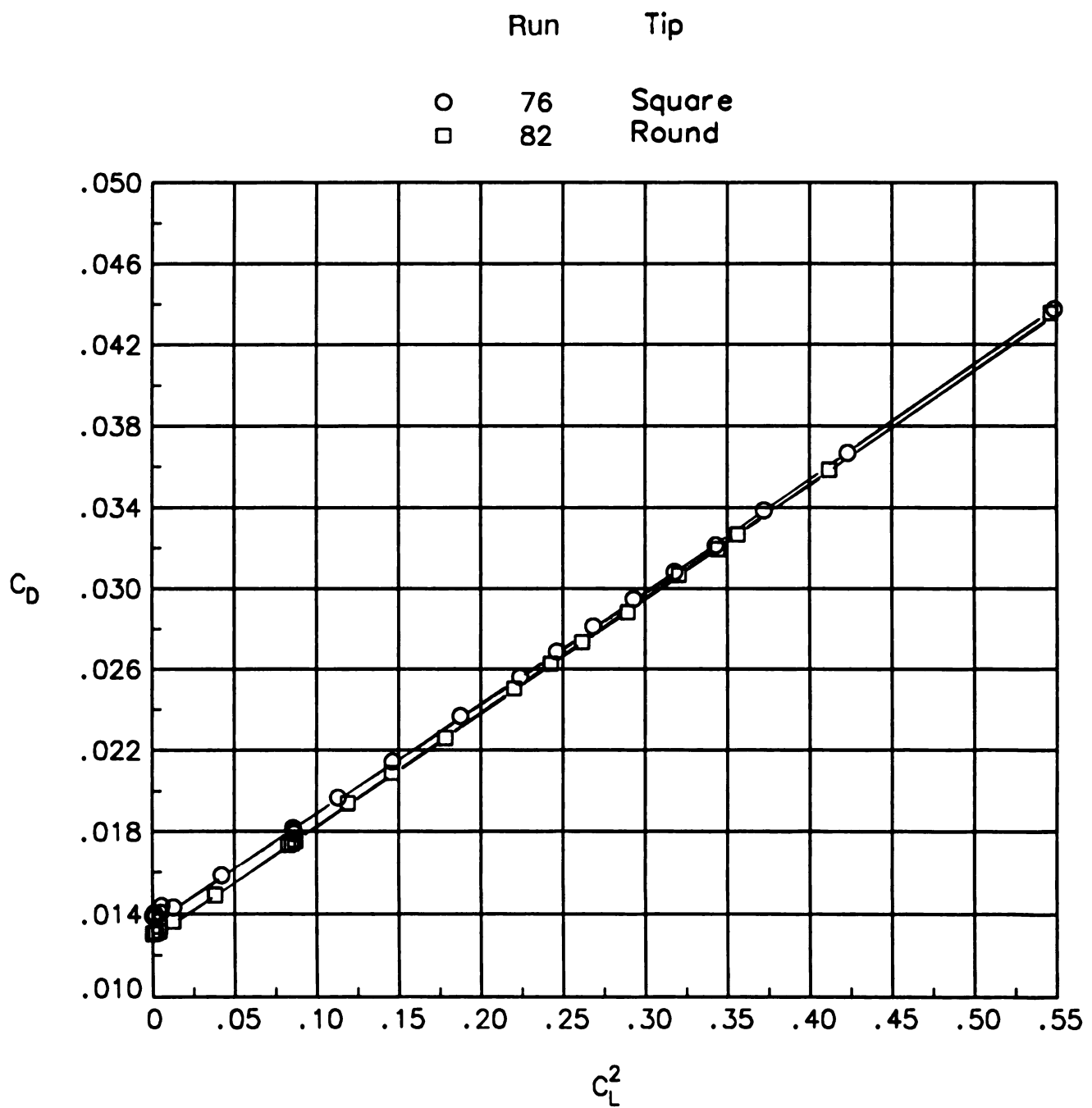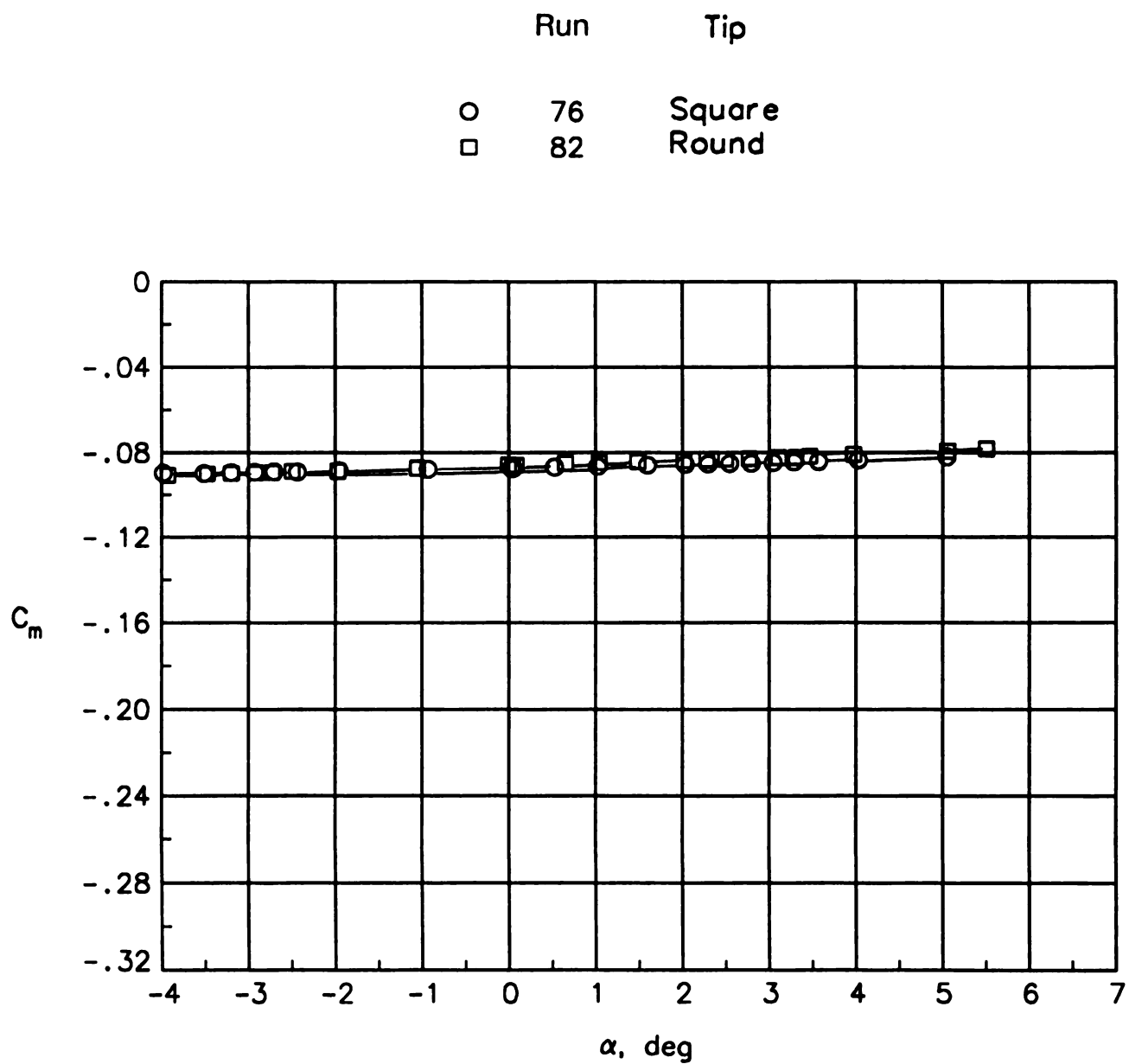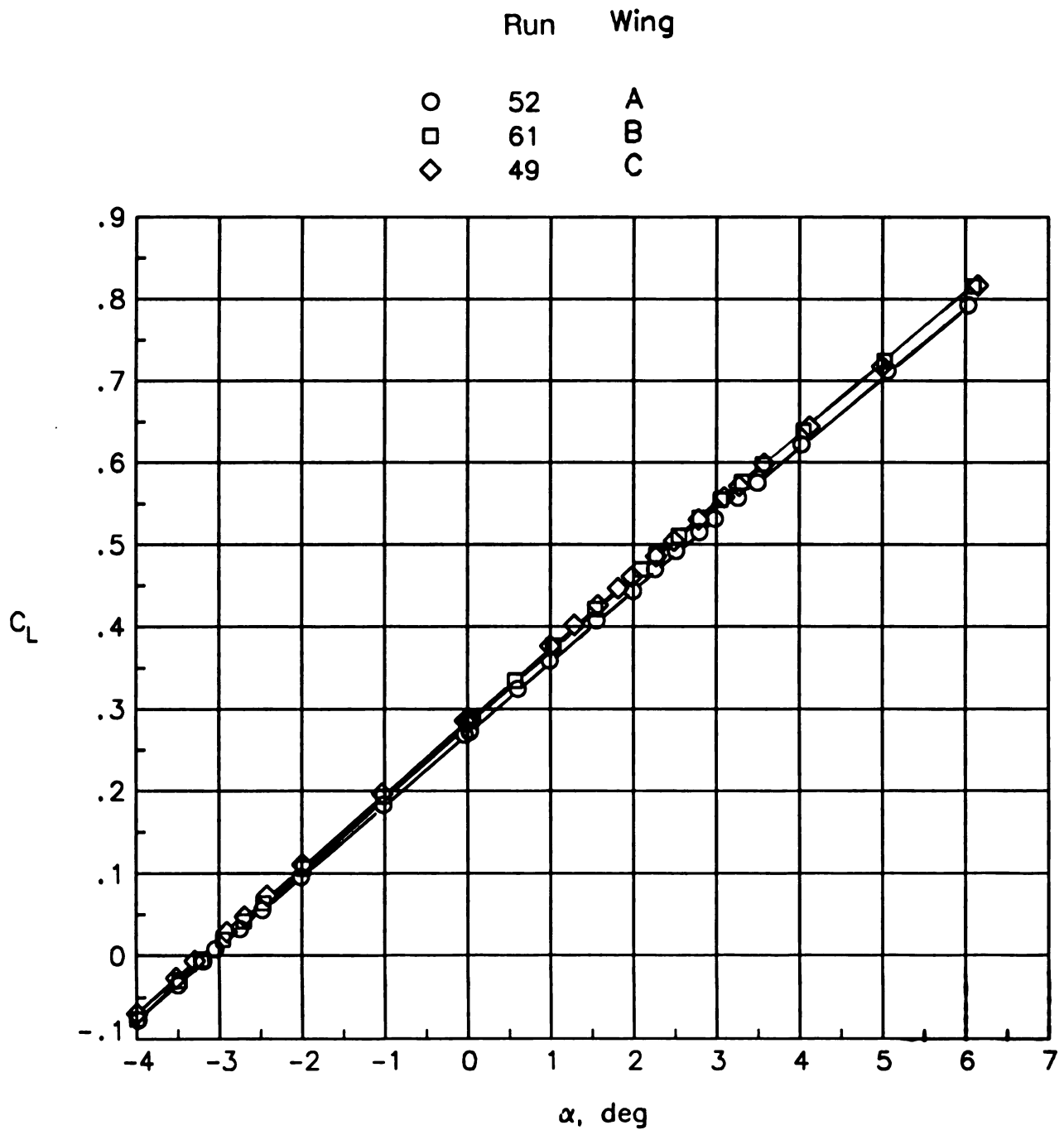(b) Variation of drag with square of lift.

Figure 12. Continued.
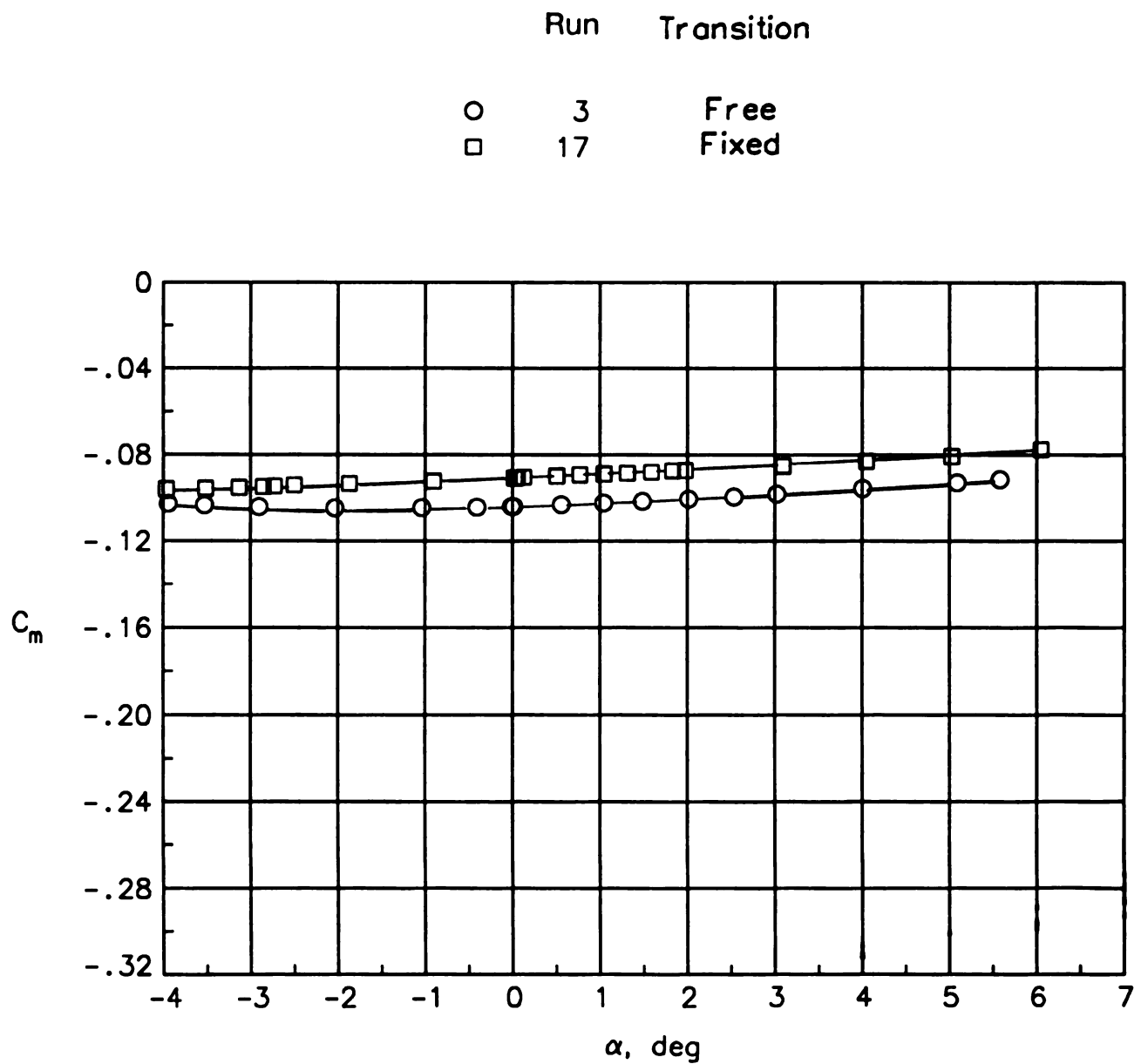
(c) Variation of pitching moment with angle of attack.

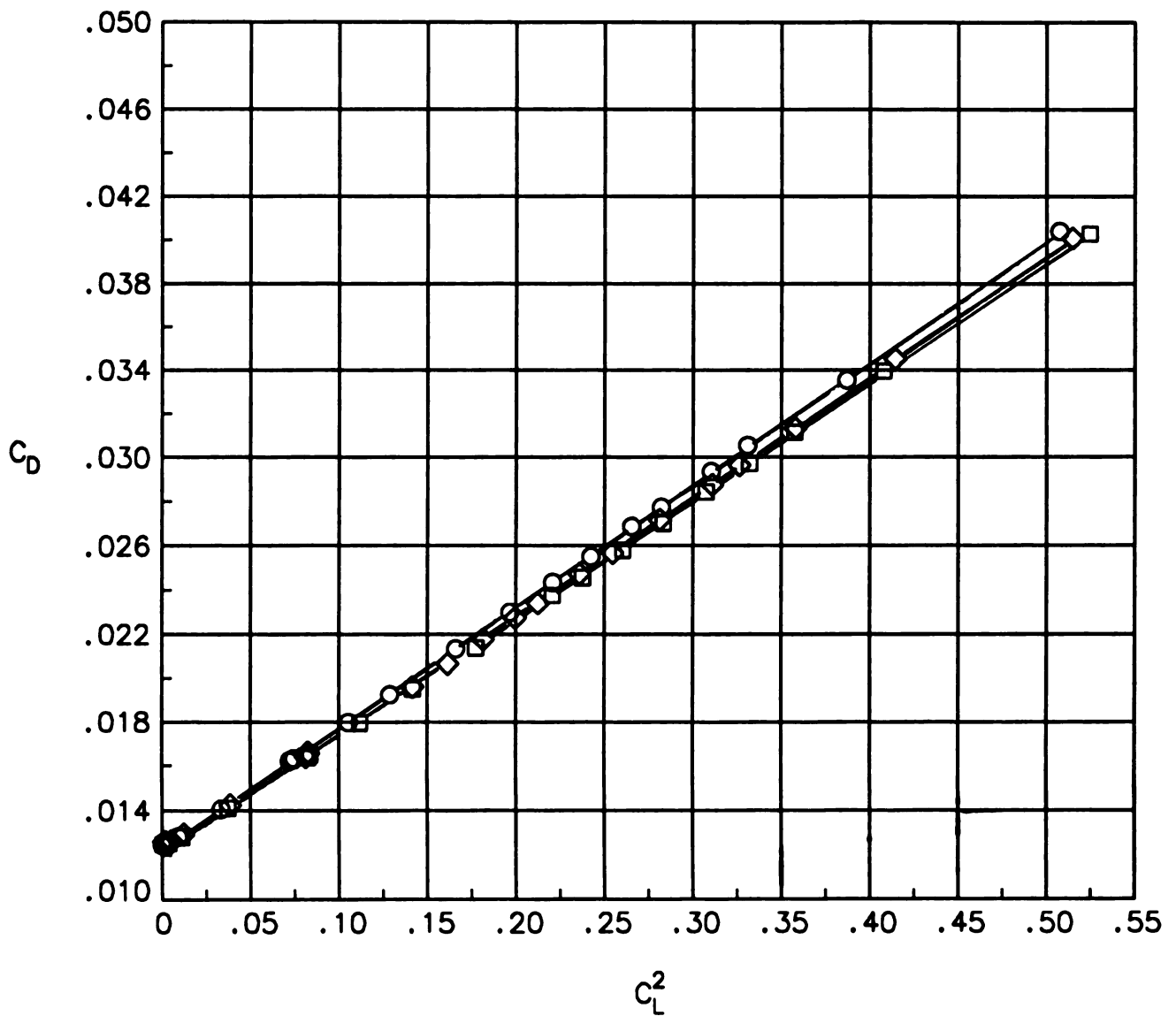Figure 12. Concluded.
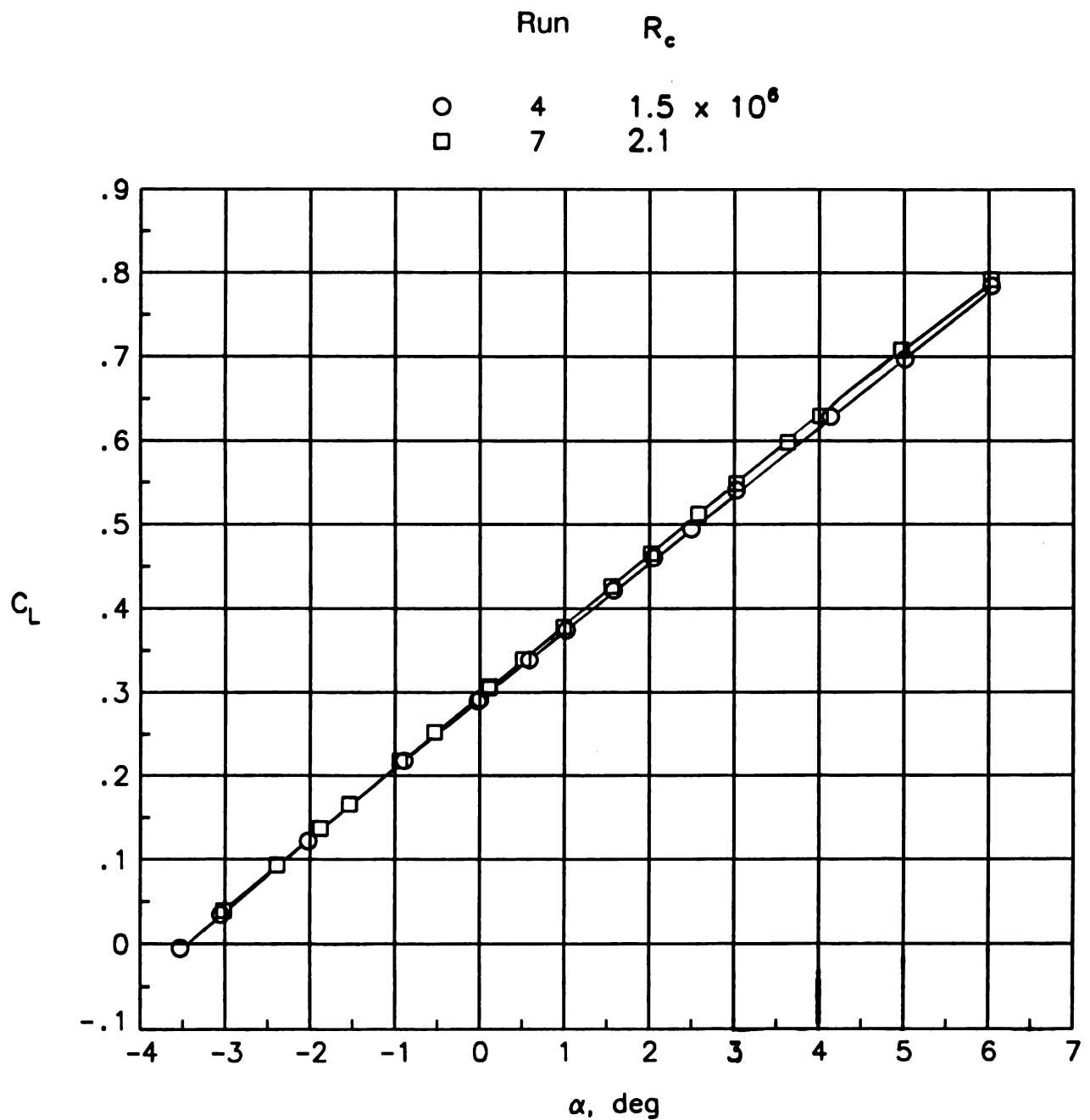
(a) Variation of lift with angle of attack.

Figure 13. Effect of Reynolds number on aerodynamic characteristics of wing A at $M_\infty = 0.3$ with free transition.
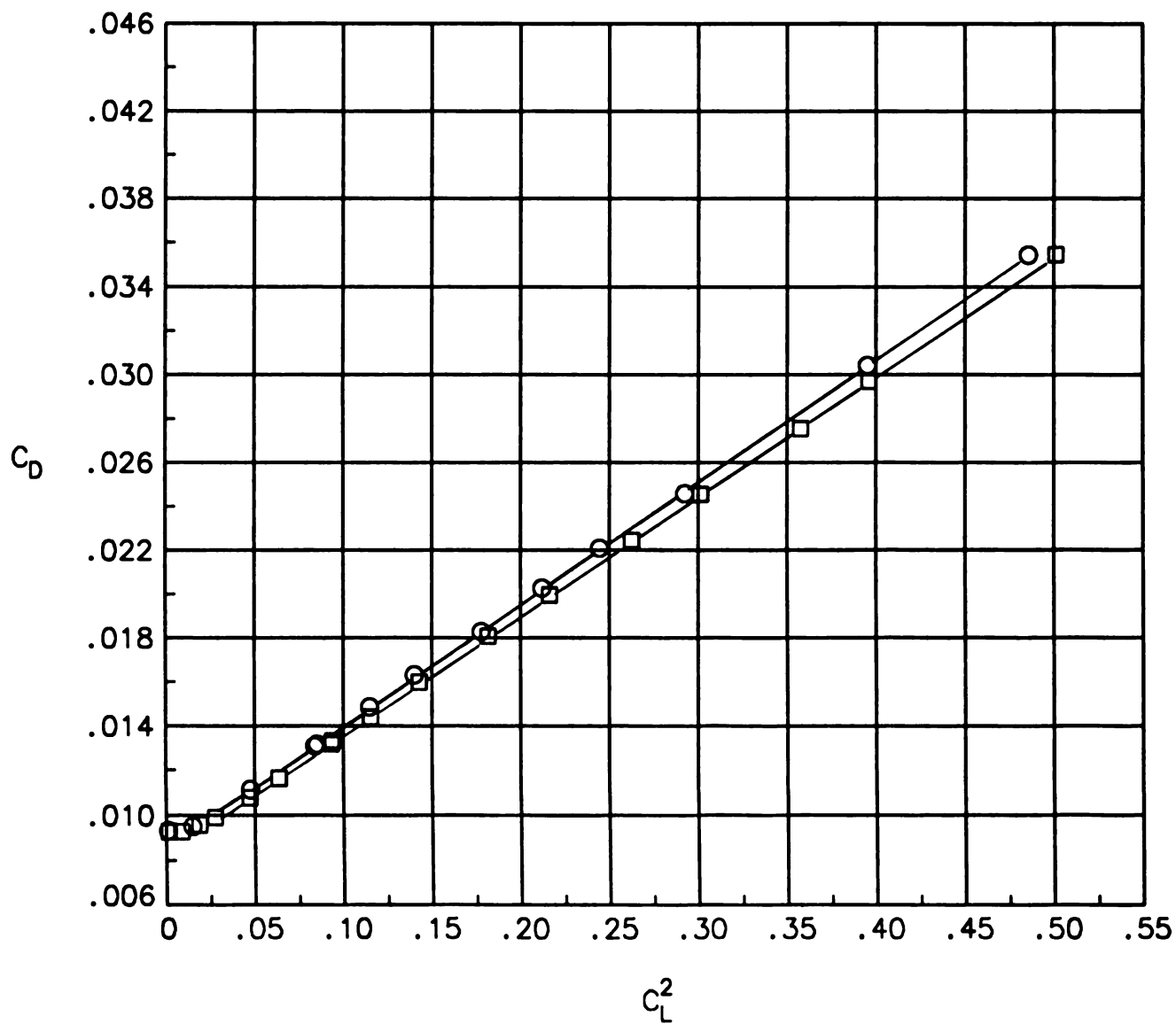
(b) Variation of drag with square of lift.

Figure 13. Continued.
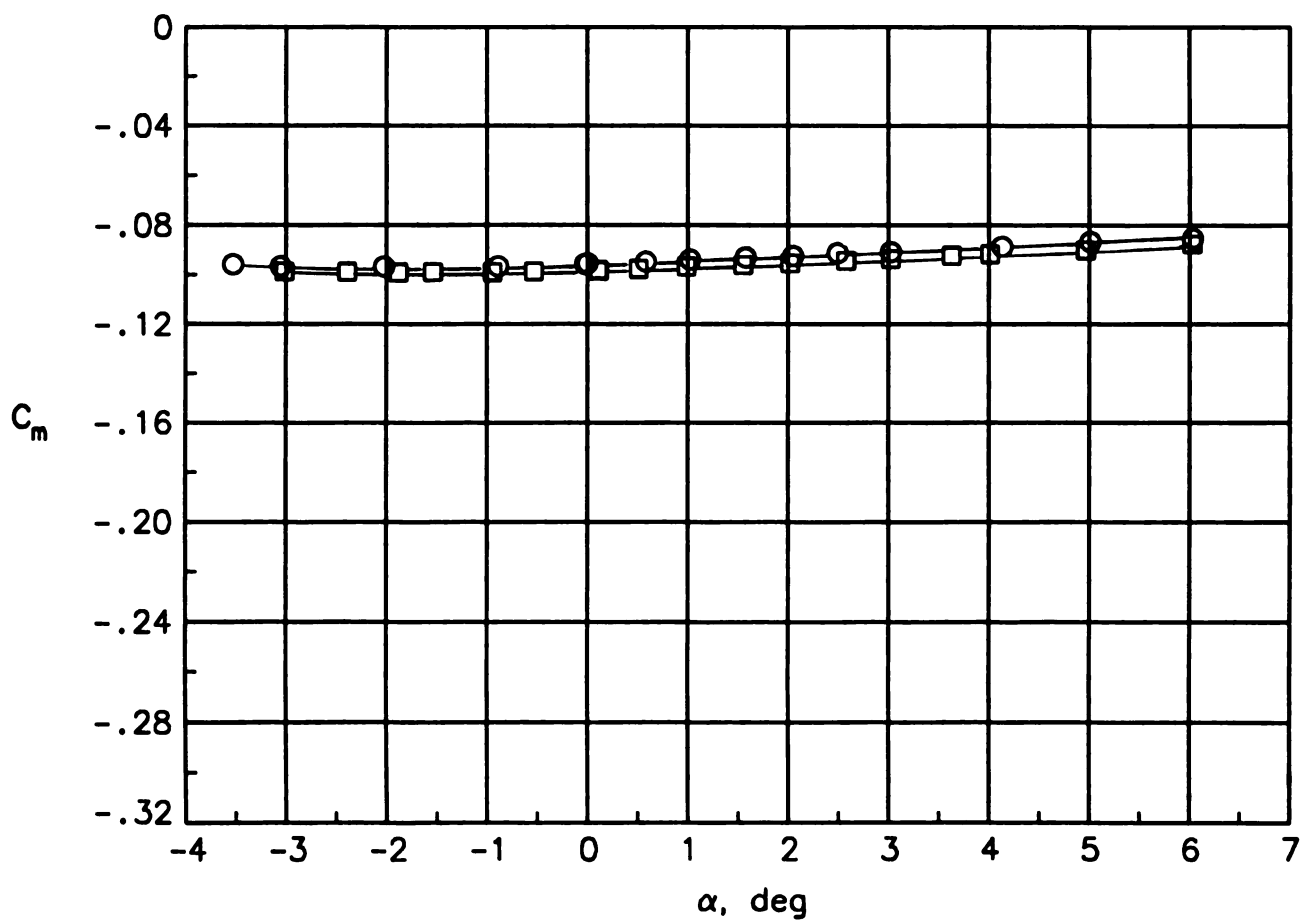
(c) Variation of pitching moment with angle of attack.

Figure 13. Concluded.

Run R_c
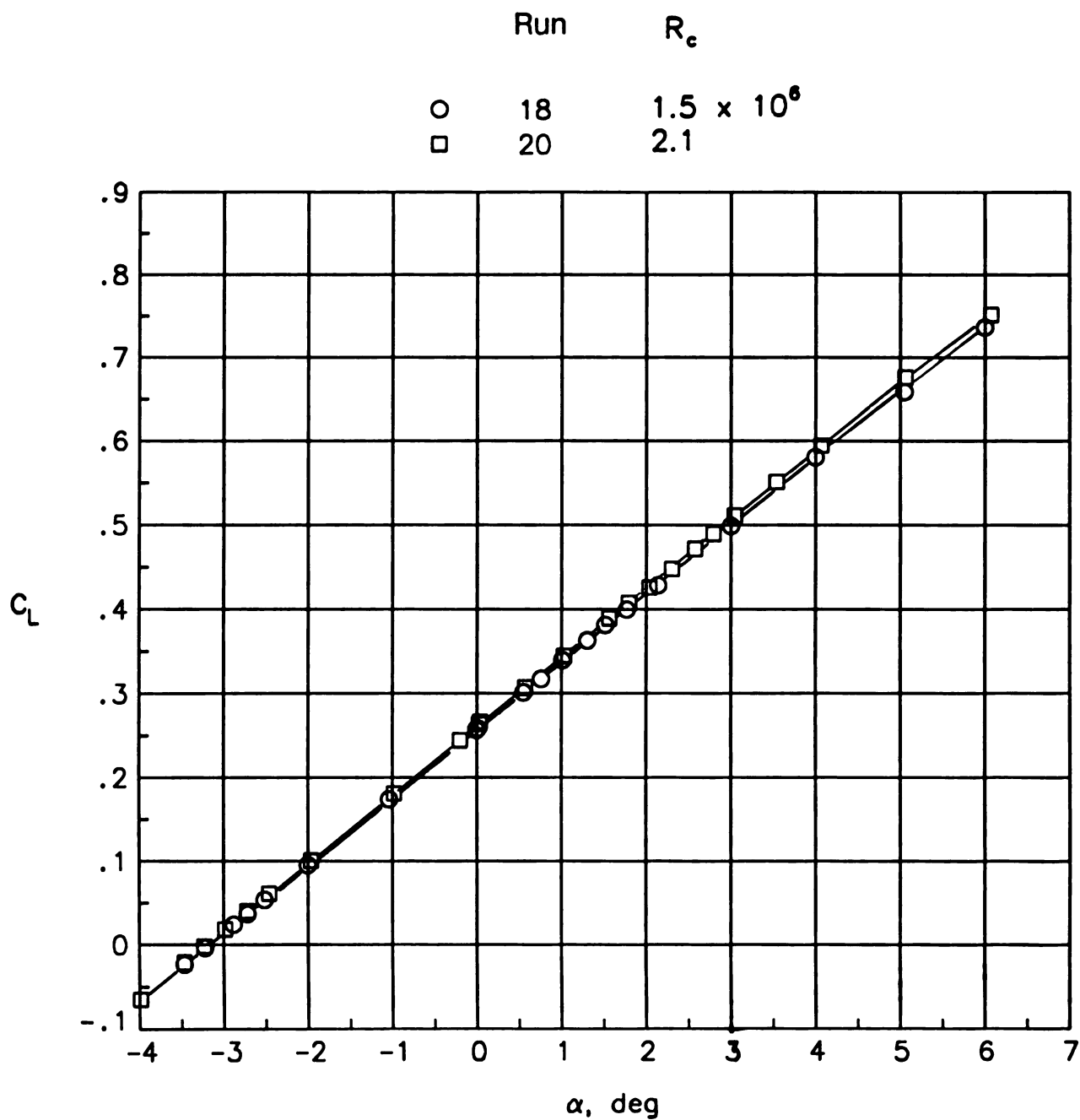
○   18 1.5×10^6
□   20   2.1

(a) Variation of lift with angle of attack.

Figure 14. Effect of Reynolds number on aerodynamic characteristics of wing A at $M_\infty = 0.3$ with fixed transition.
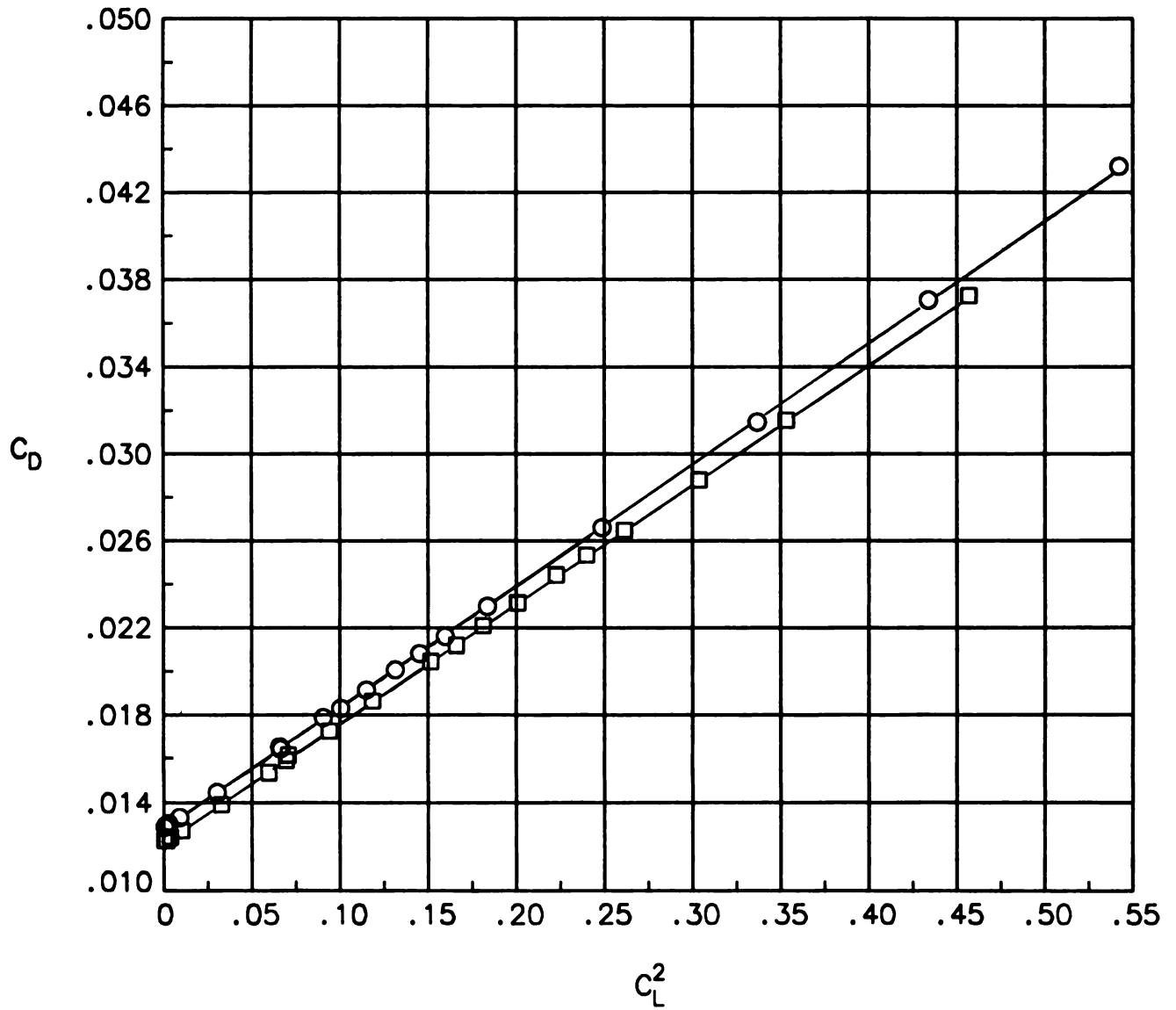
(b) Variation of drag with square of lift.

Figure 14. Continued.
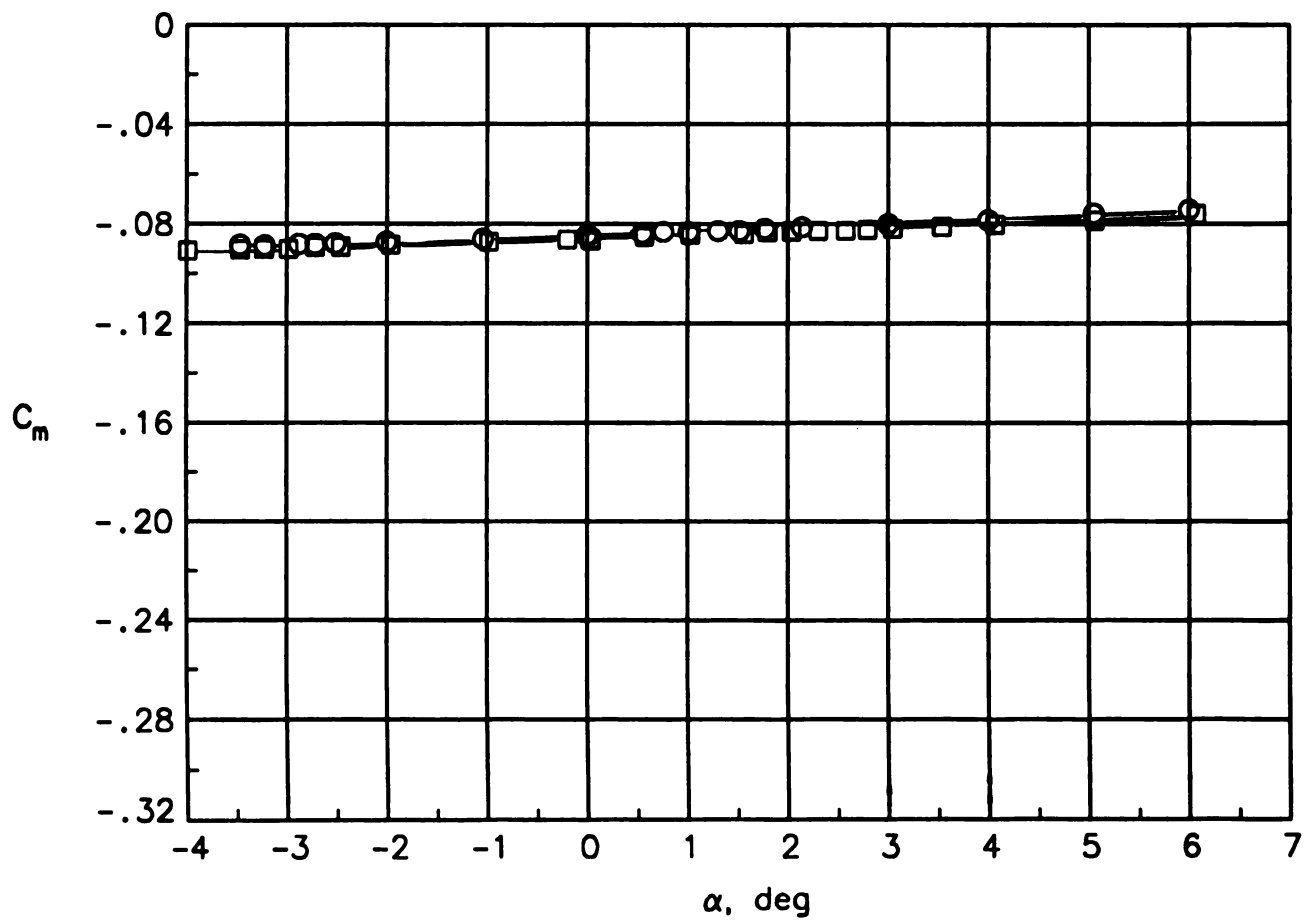
(c) Variation of pitching moment with angle of attack.

Figure 14. Concluded.
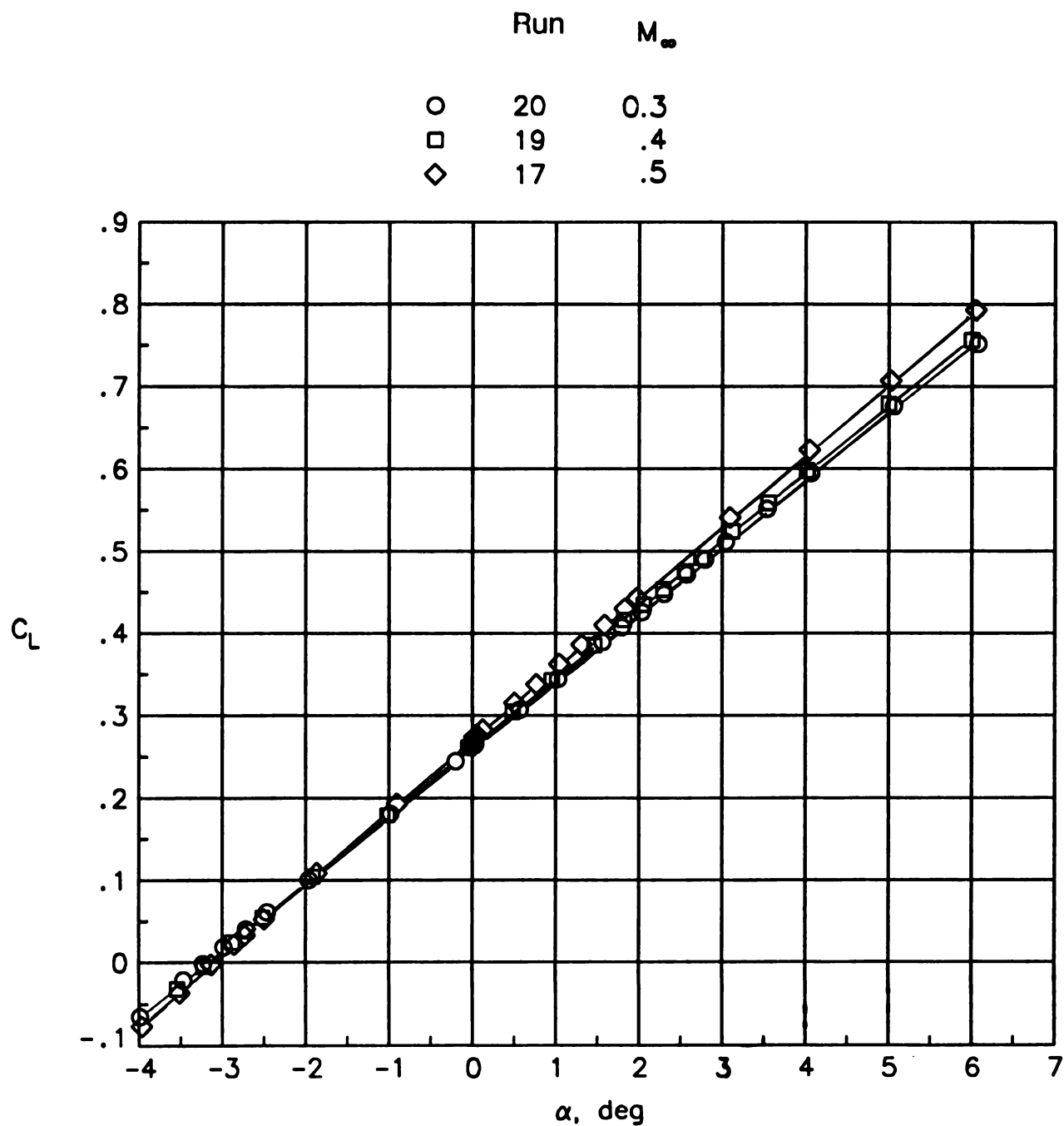
(a) Variation of lift with angle of attack.

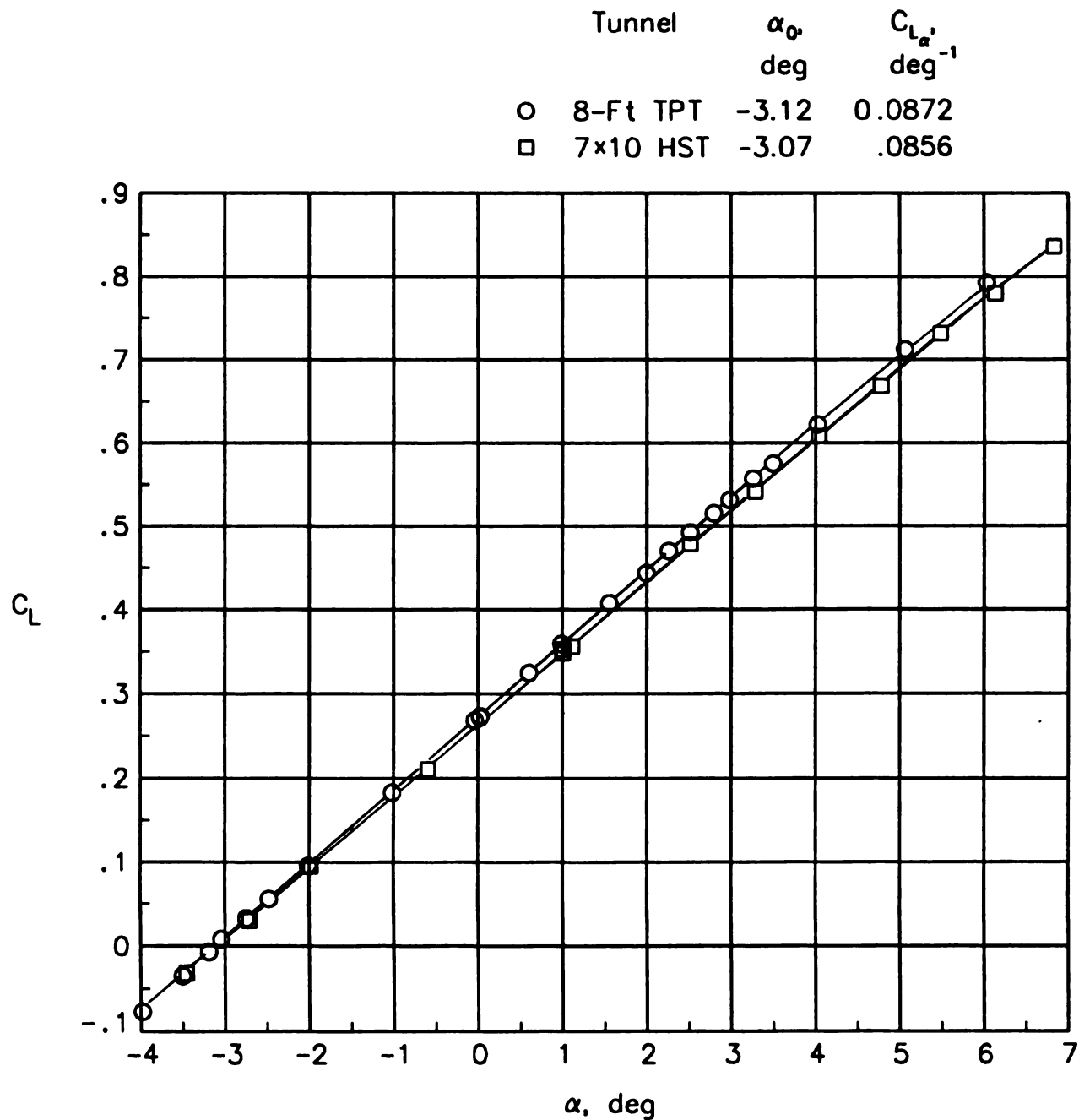Figure 15. Effect of Mach number on aerodynamic characteristics of wing A. $R_c = 2.1 \times 10^6$.
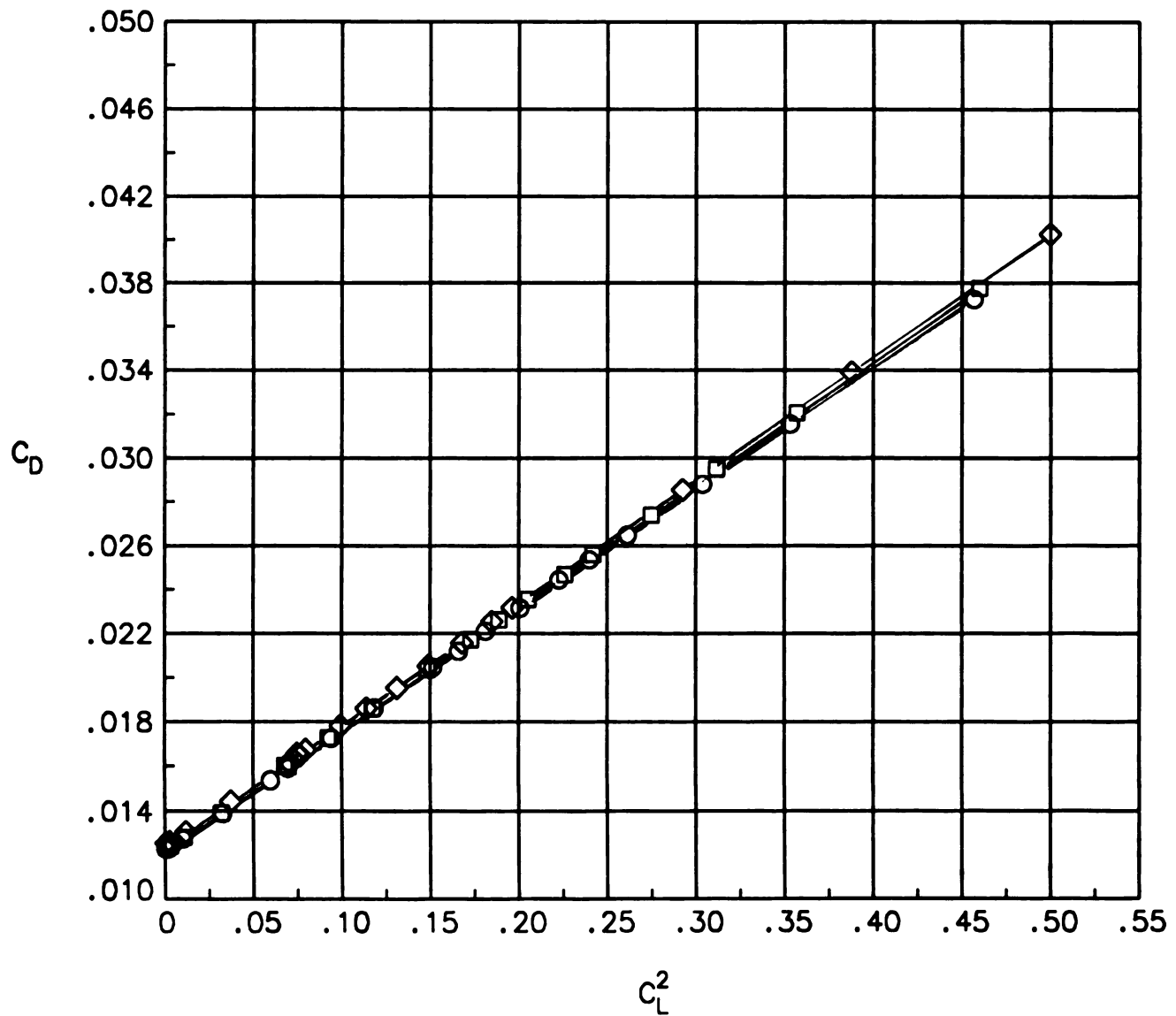
(b) Variation of drag with square of lift.

Figure 15. Continued.
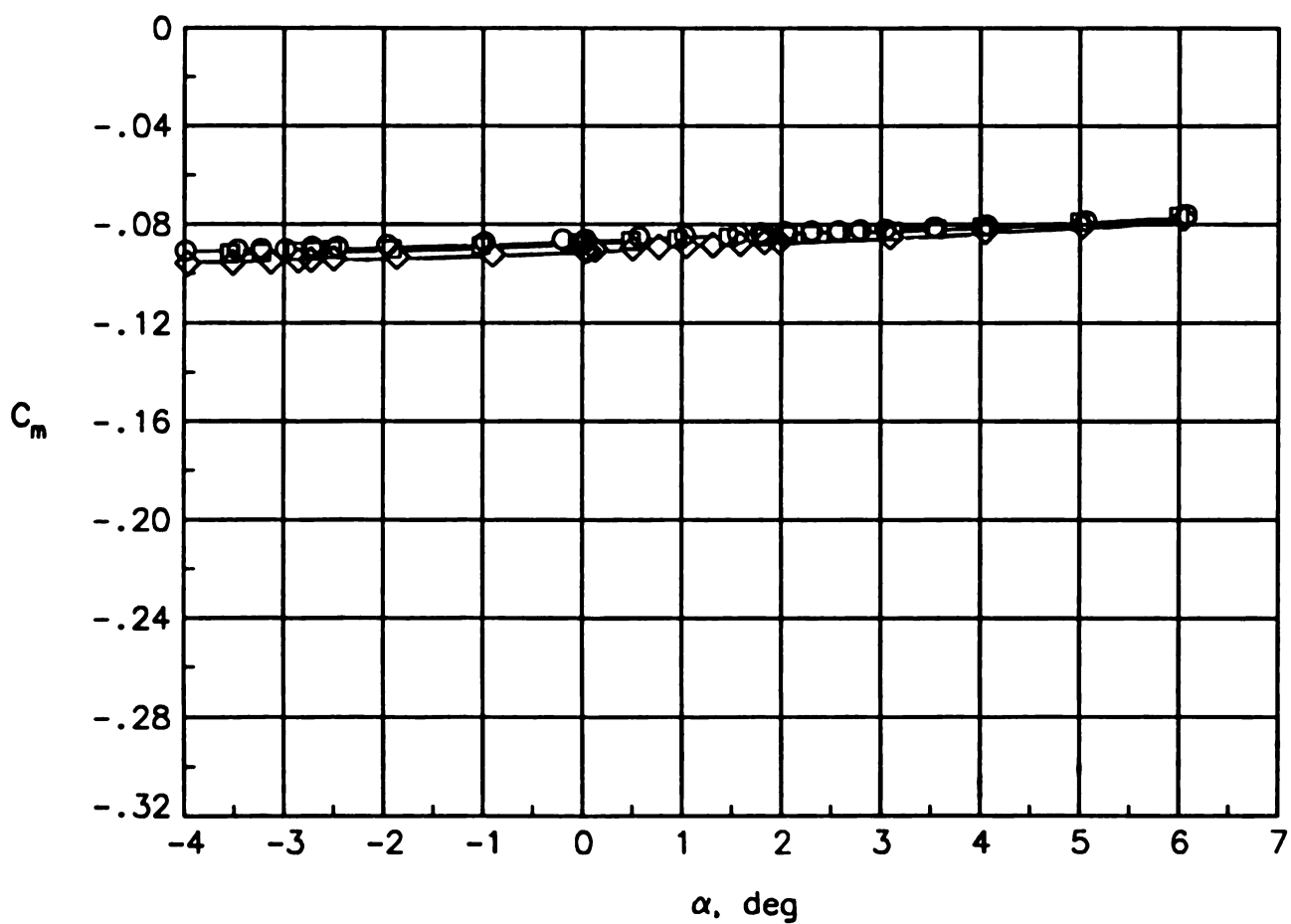
(c) Variation of pitching moment with angle of attack.

Figure 15. Concluded.
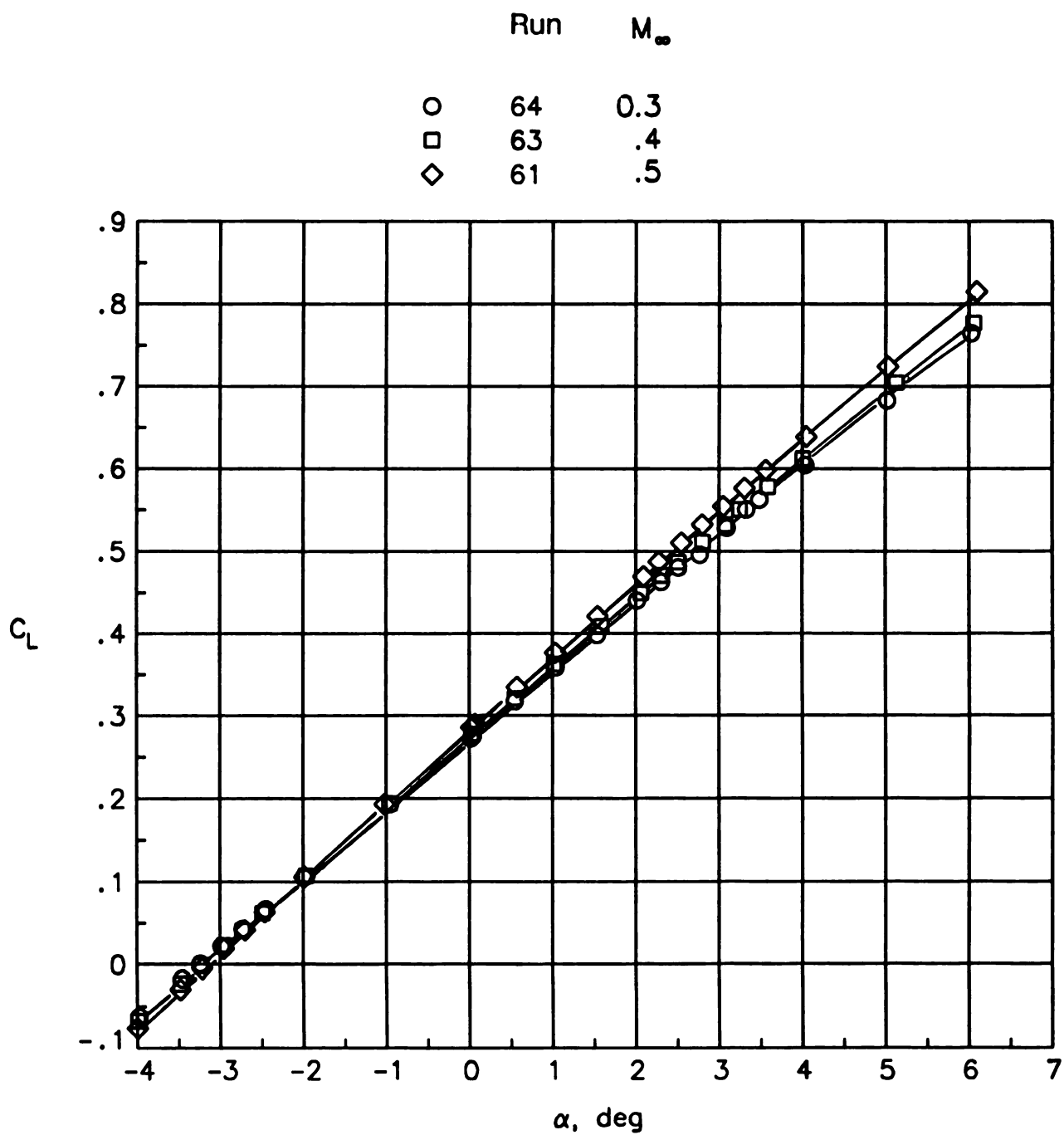
Run M_∞

○ 64 0.3
□ 63 .4
◇ 61 .5

(a) Variation of lift with angle of attack.

Figure 16. Effect of Mach number on aerodynamic characteristics of wing B. $R_c = 2.1 \times 10^6$.
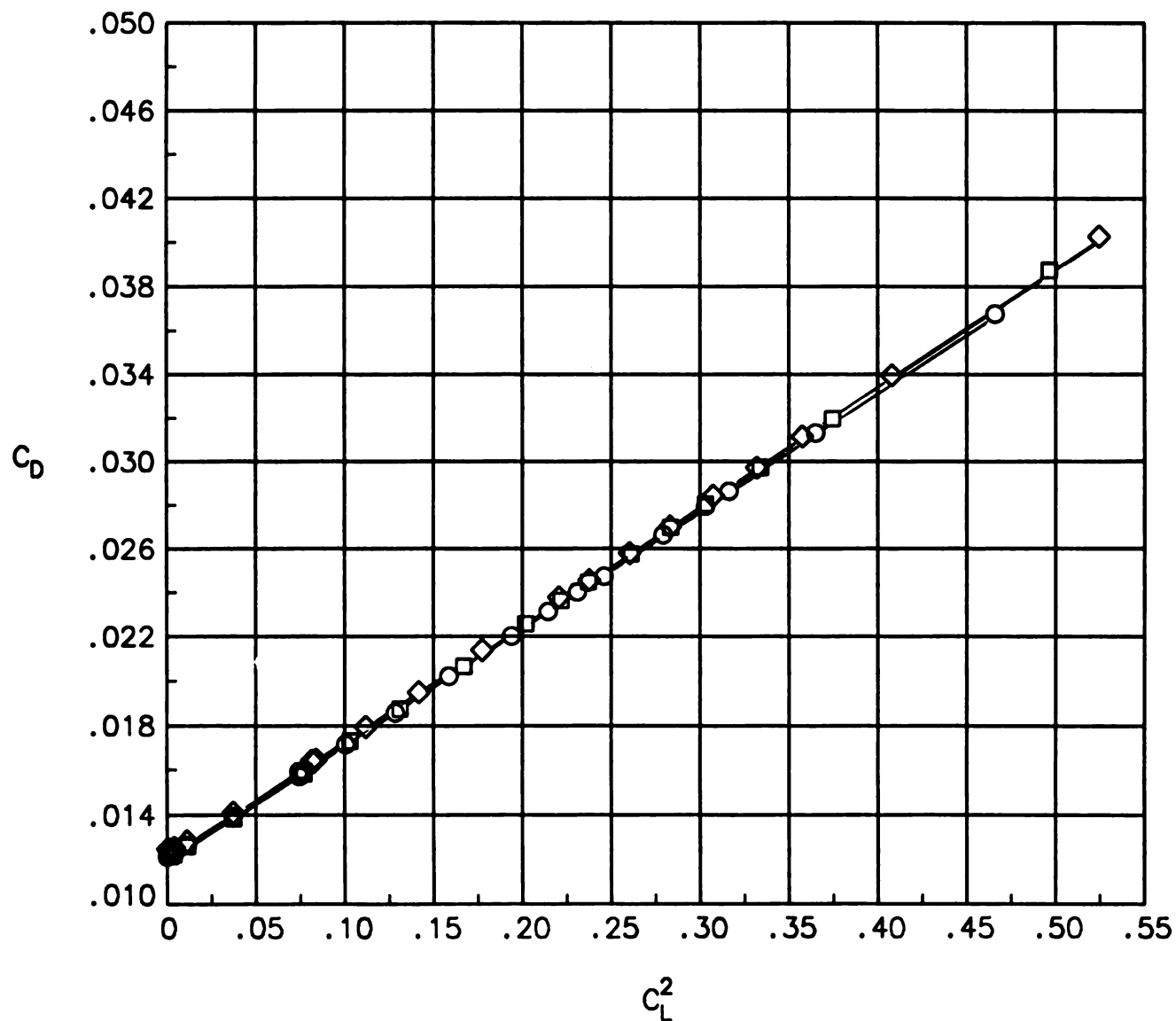
(b) Variation of drag with square of lift.

Figure 16. Continued.
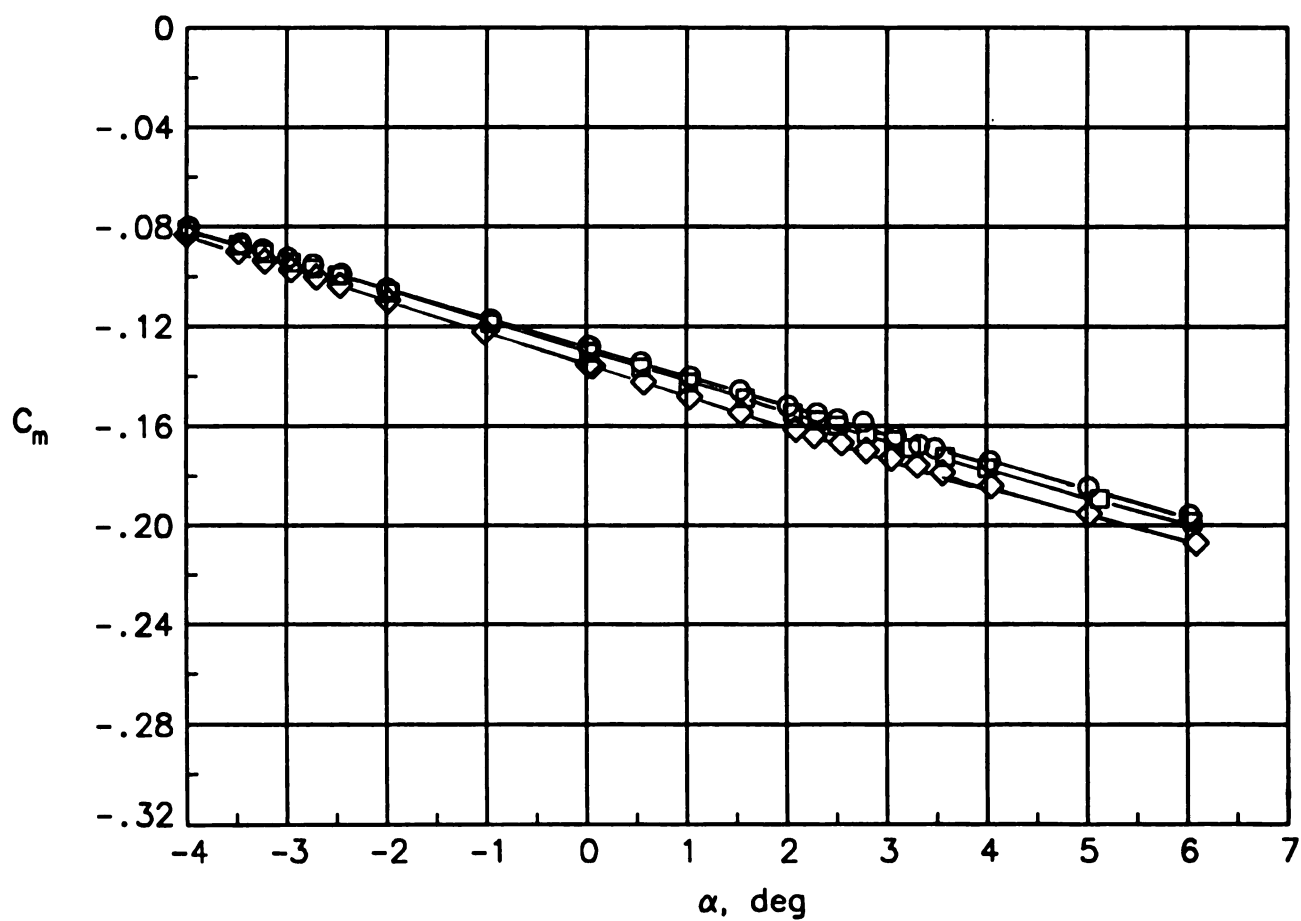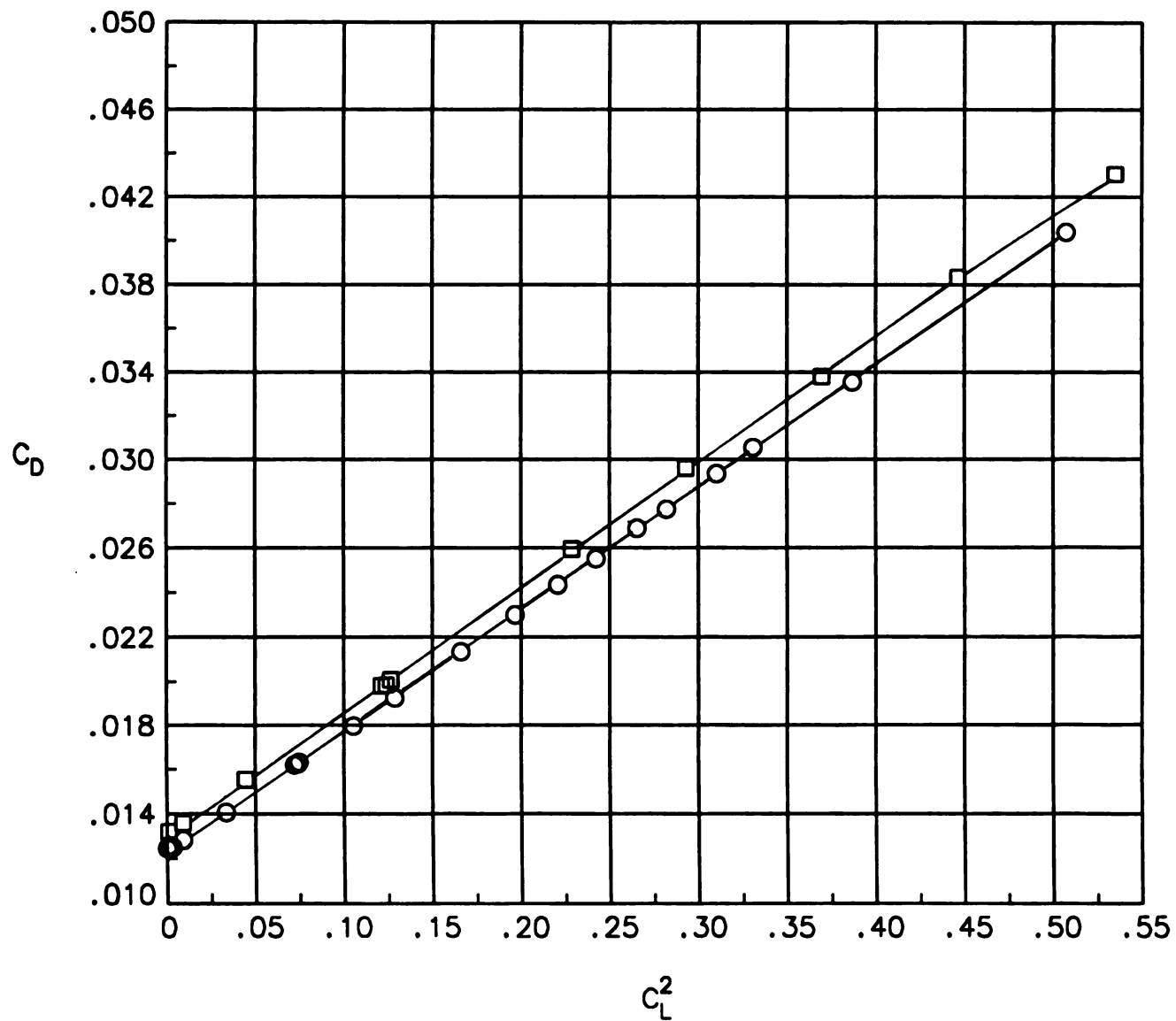
(c) Variation of pitching moment with angle of attack.

Figure 16. Concluded.
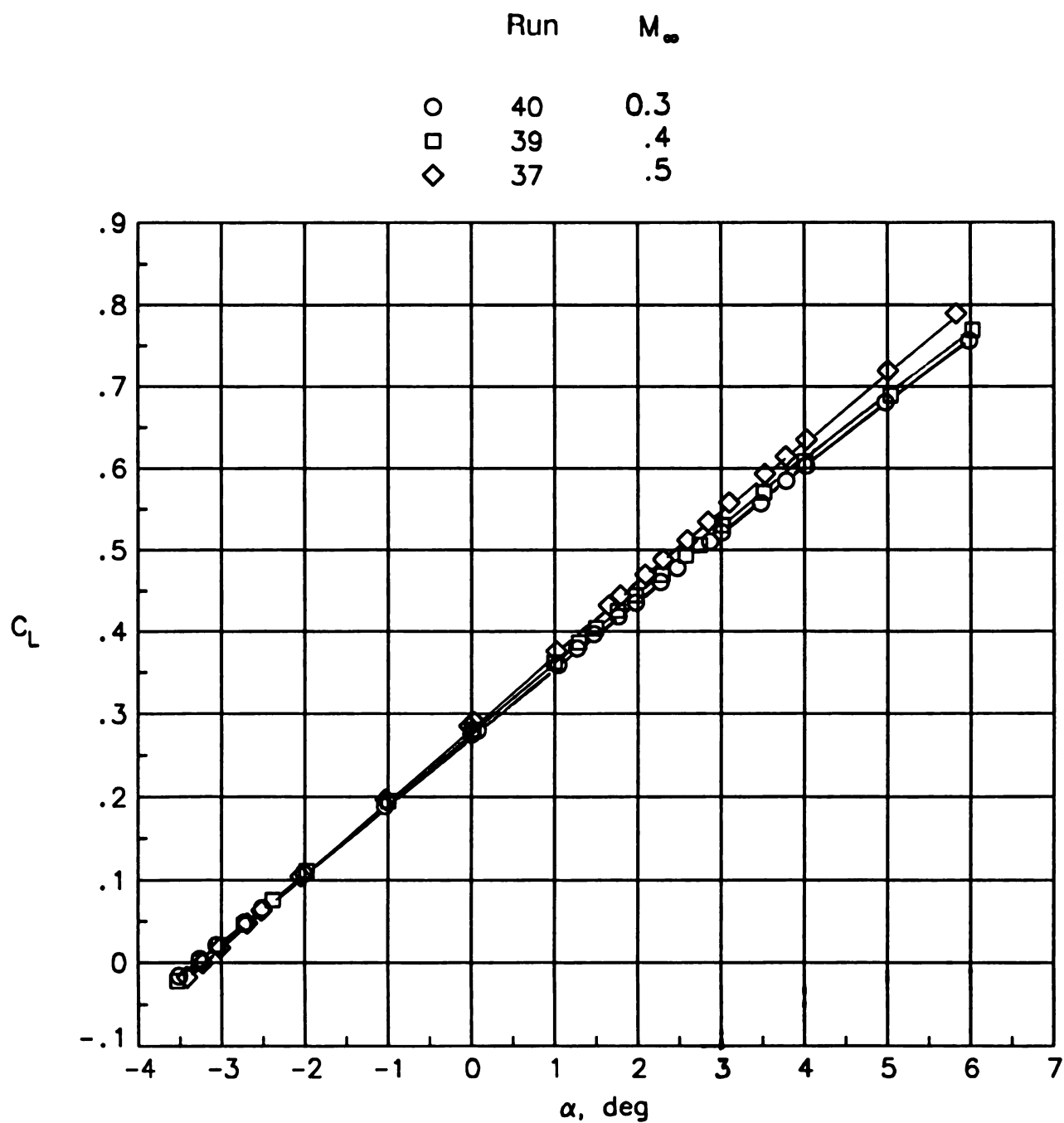
Run	M_∞
○ 40	0.3
□ 39	.4
◇ 37	.5

(a) Variation of lift with angle of attack.

Figure 17. Effect of Mach number on aerodynamic characteristics of wing C. $R_c = 2.1 \times 10^6$.
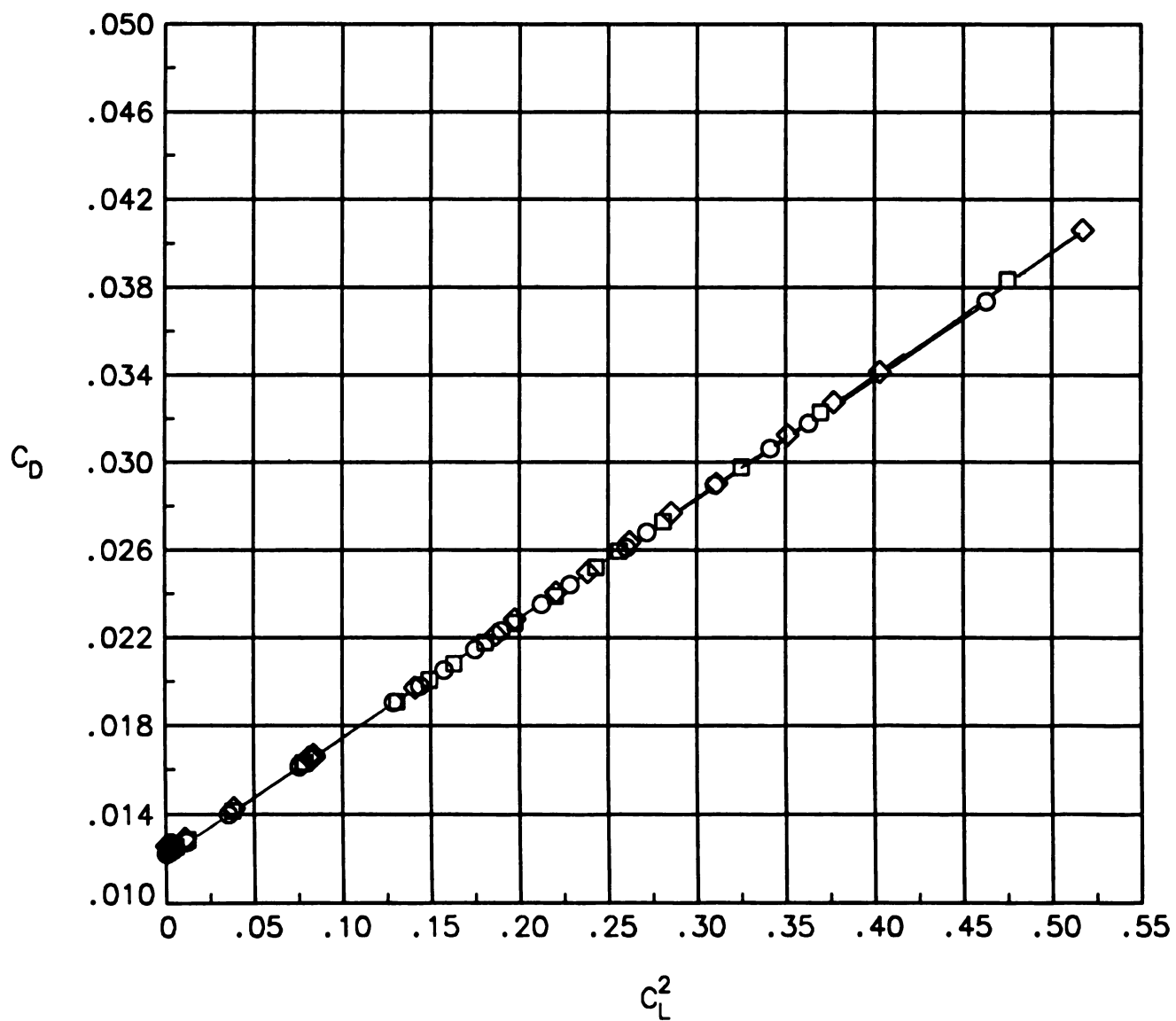
(b) Variation of drag with square of lift.

Figure 17. Continued.

Run   M∞

○   40   0.3
□   39   .4
◇   37   .5
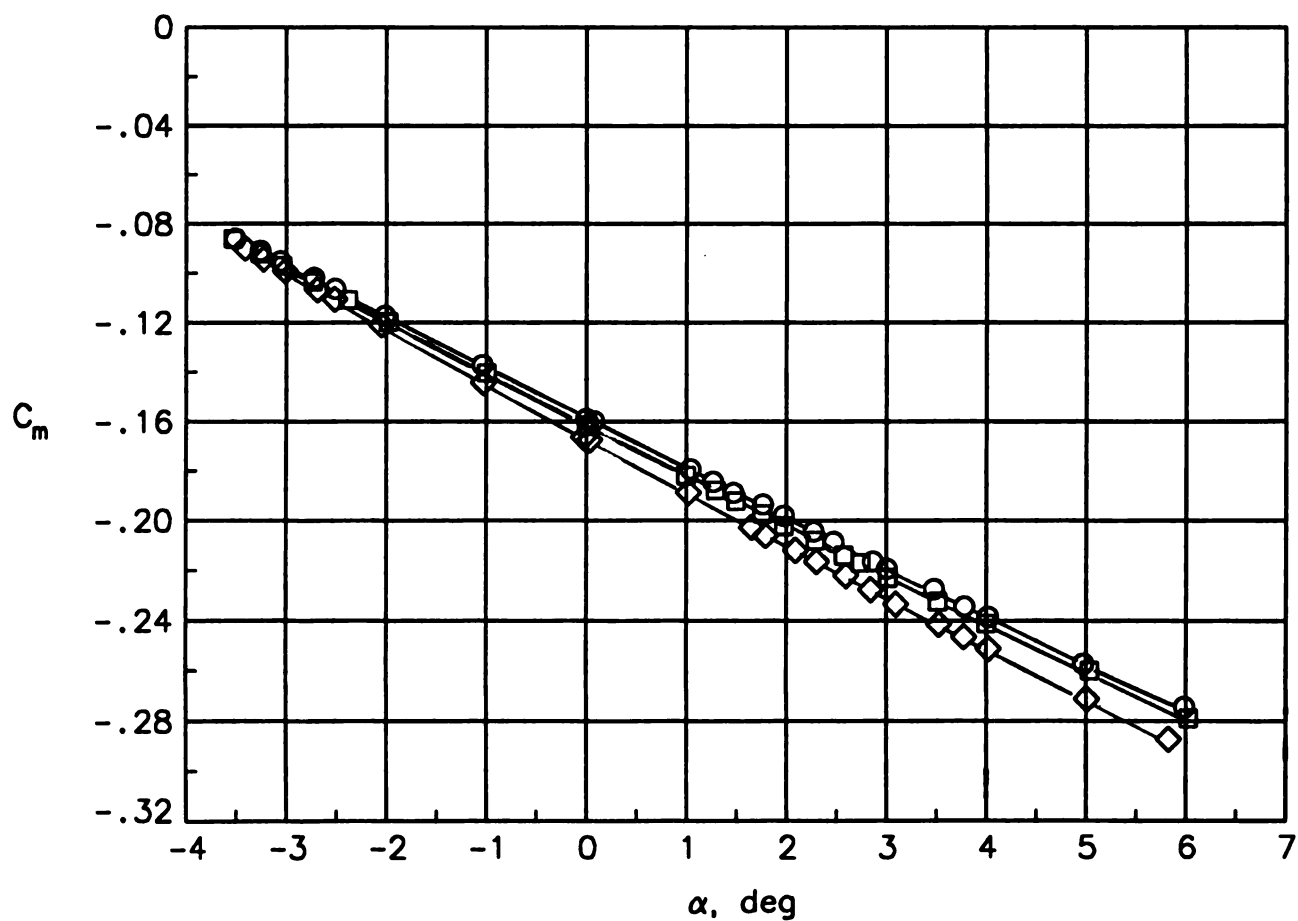
(c) Variation of pitching moment with angle of attack.

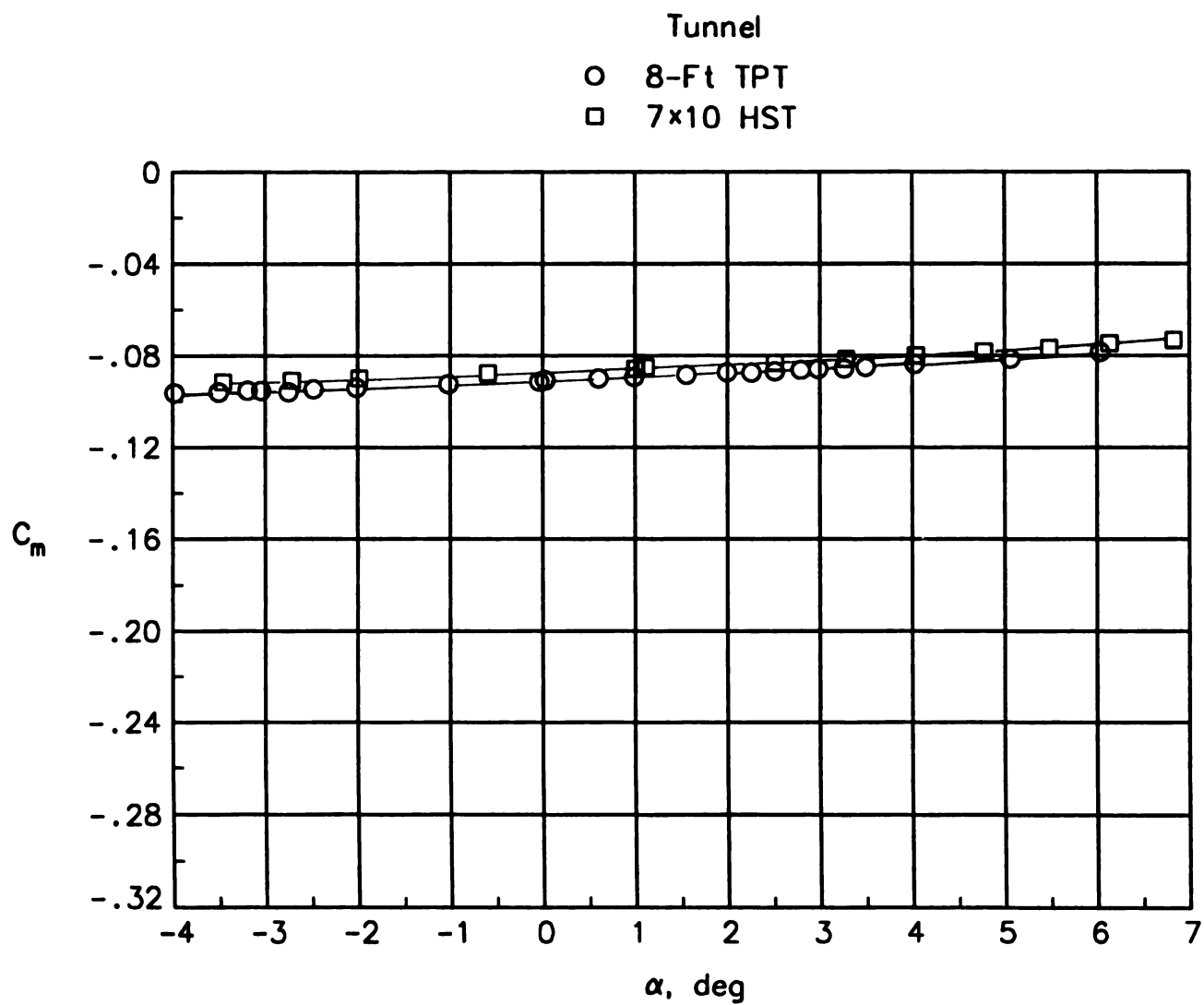Figure 17. Concluded.
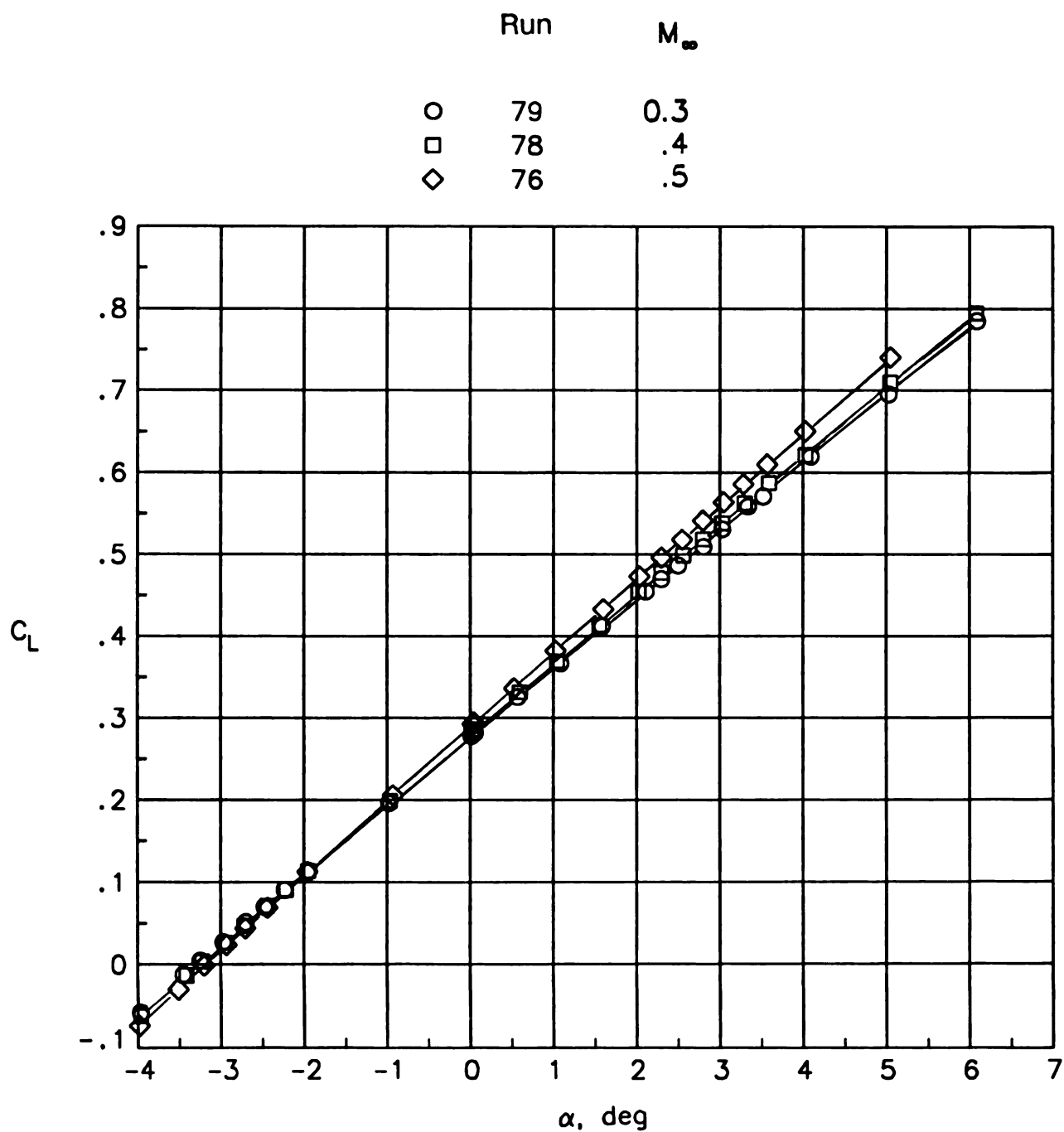
(a) Variation of lift with angle of attack.

Figure 18. Effect of Mach number on aerodynamic characteristics of wing D. $R_c = 2.1 \times 10^6$.
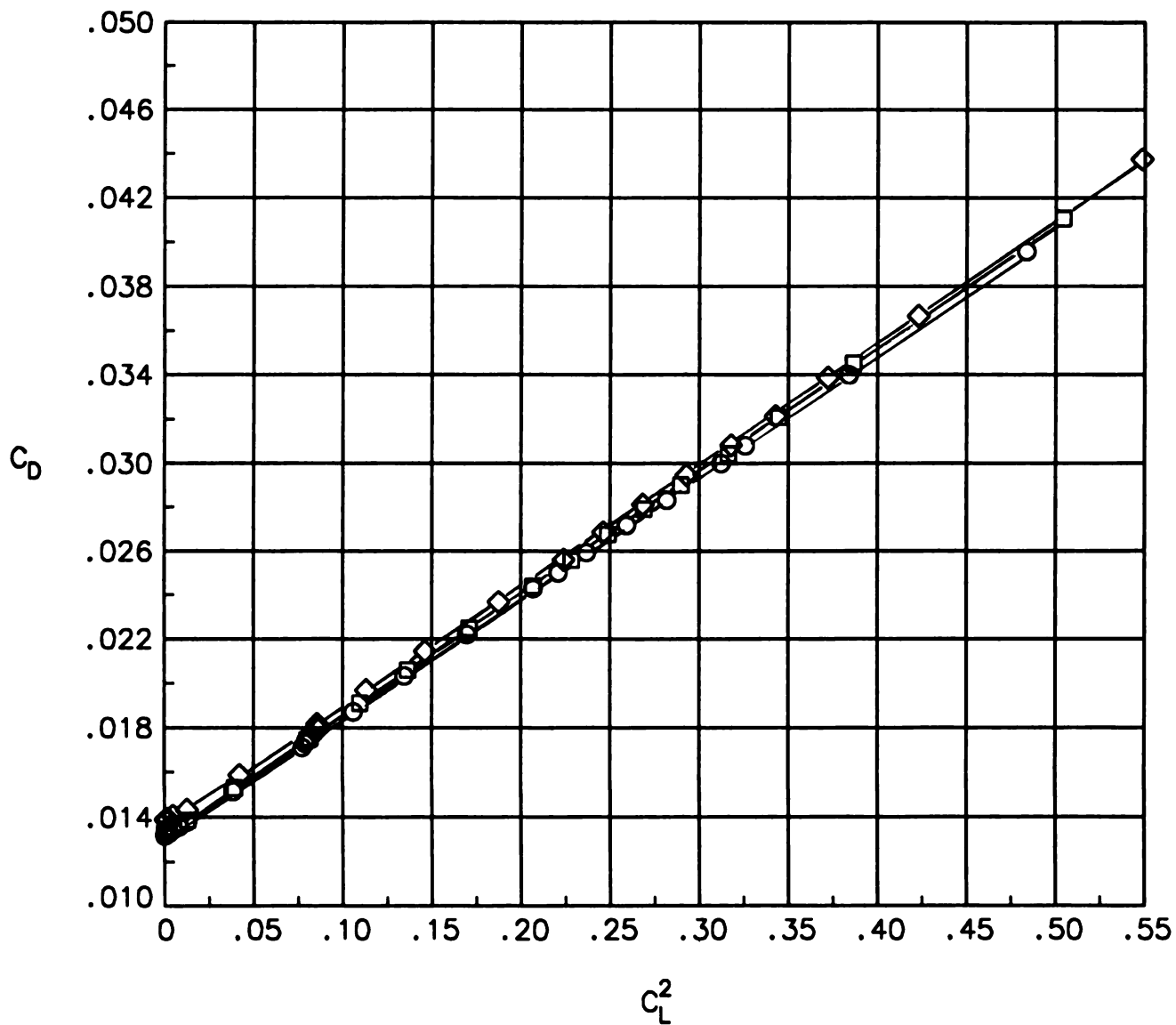
(b) Variation of drag with square of lift.

Figure 18. Continued.
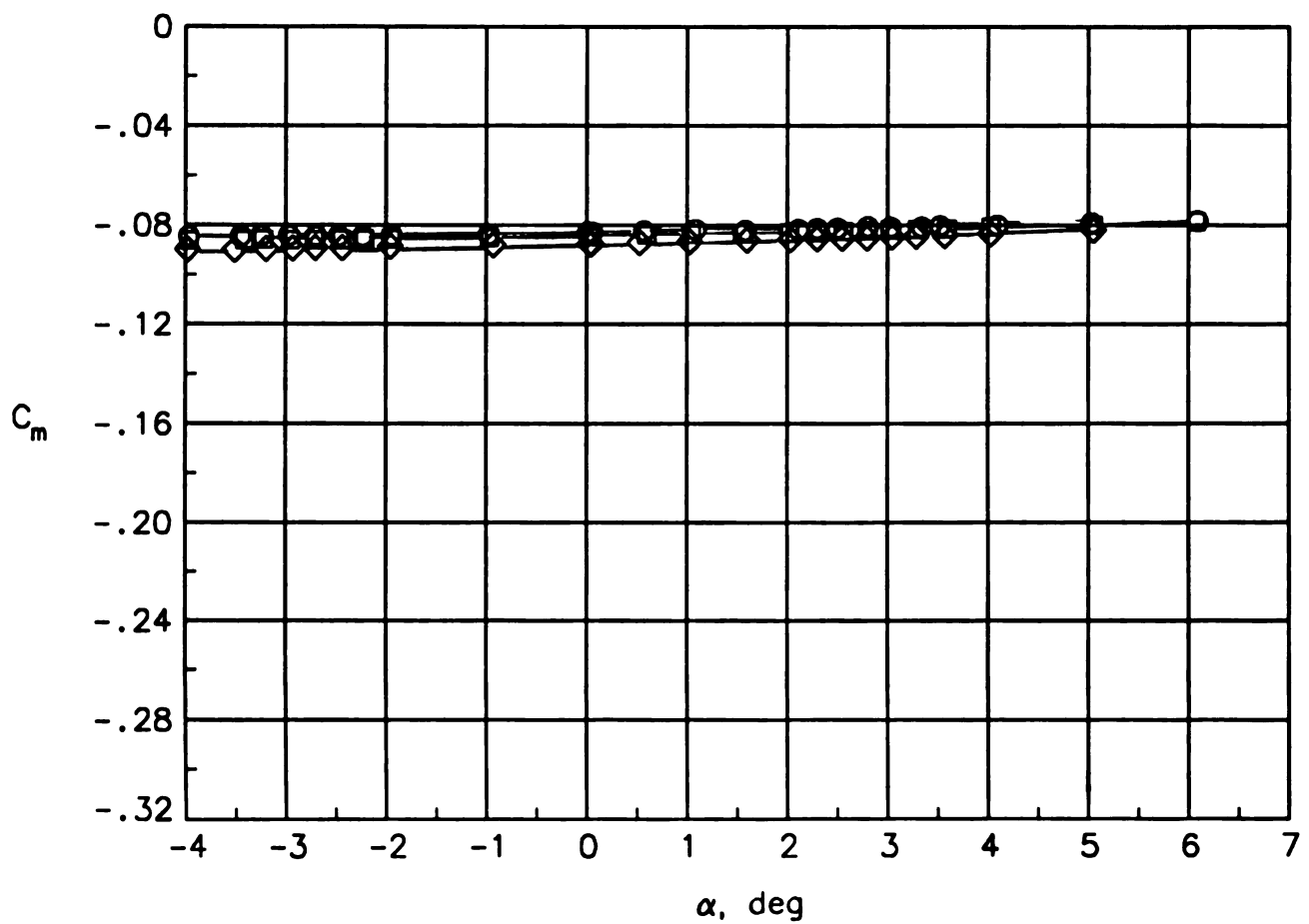
(c) Variation of pitching moment with angle of attack.

Figure 18. Concluded.
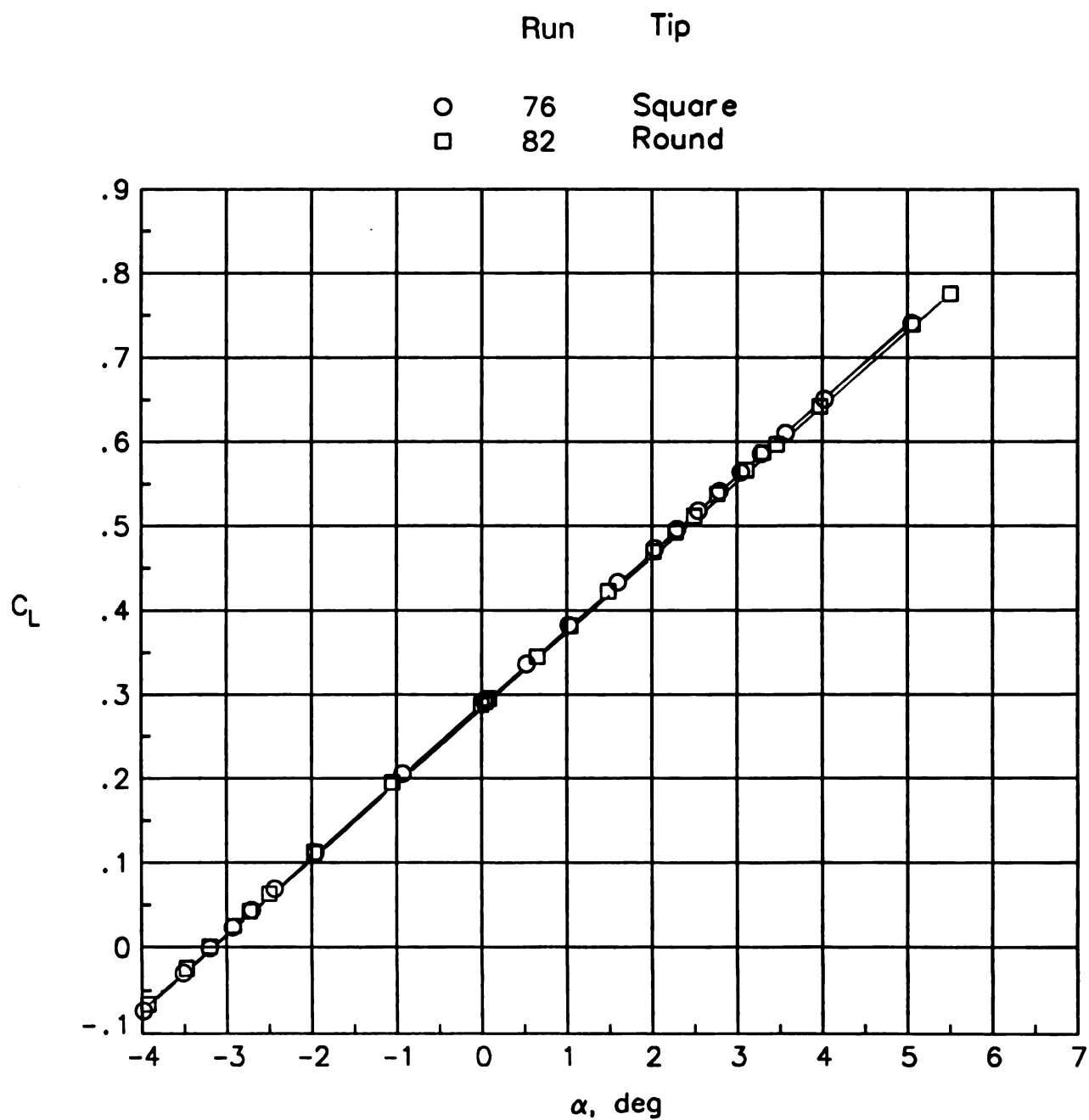
(a) Variation of lift with angle of attack.

Figure 19. Effect of tip shape on aerodynamic characteristics of wing D. $M_\infty = 0.5$; $R_c = 2.1 \times 10^6$.

(b) Variation of drag with lift squared.

Figure 19. Continued.

(c) Variation of pitching moment with angle of attack.

Figure 19. Concluded.

(a) Variation of lift with angle of attack.

Figure 20. Effect of elliptical wing planform shape on aerodynamic characteristics. $M_\infty = 0.5$; $R_c = 2.1 \times 10^6$.

(b) Variation of drag with square of lift.

Figure 20. Continued.
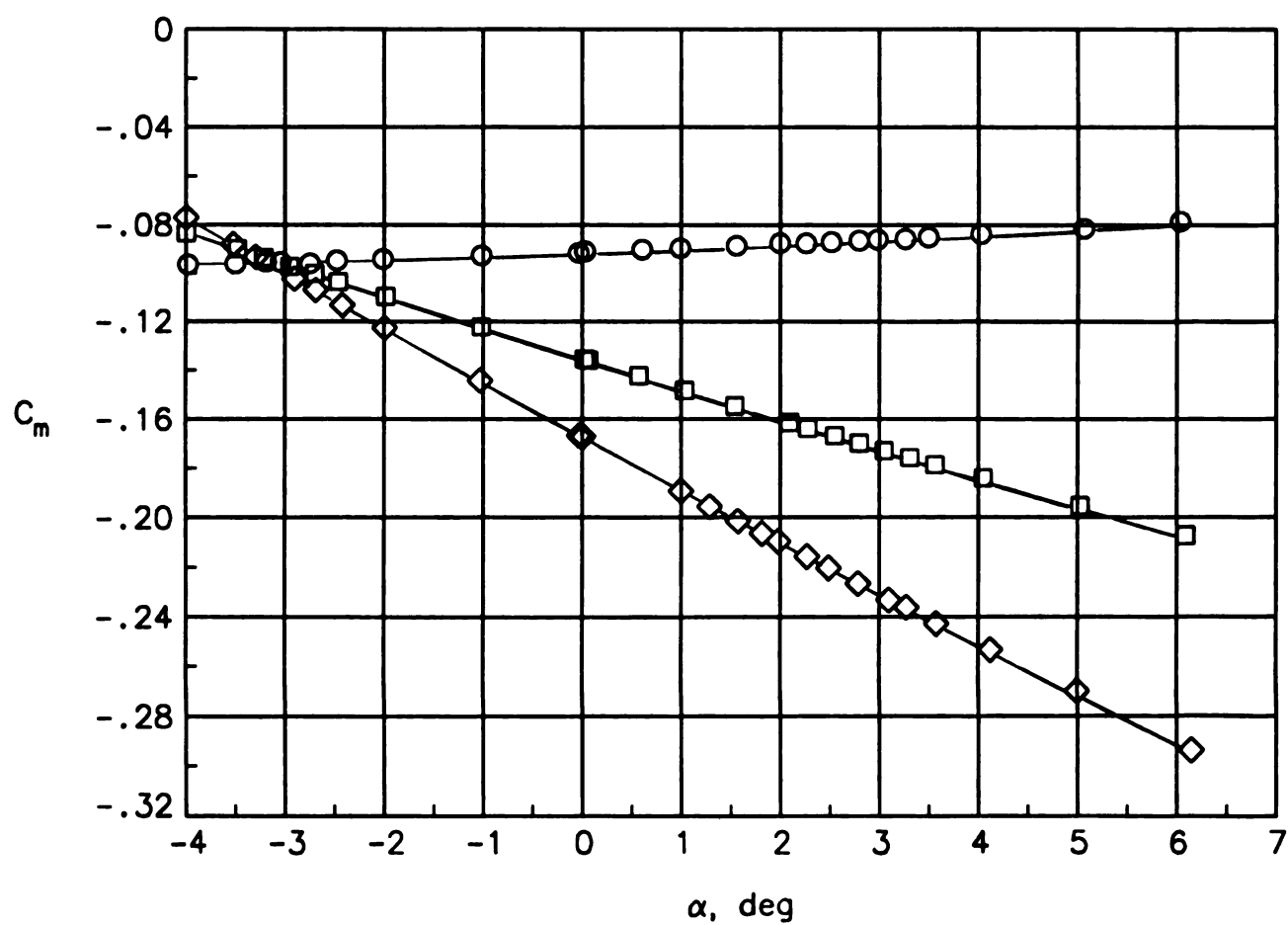
(c) Variation of pitching moment with angle of attack.

Figure 20. Concluded.

Tunnel	α_0, deg	C_{L_α}, deg^{-1}
○ 8-Ft TPT	−3.12	0.0872
□ 7×10 HST	−3.07	.0856

(a) Variation of lift with angle of attack.

Figure 21. Comparison of aerodynamic characteristics from both wind tunnels for wing A with fixed transition. $M_\infty = 0.5$.

(b) Variation of drag with square of lift.

Figure 21. Continued.

(c) Variation of pitching moment with angle of attack.

Figure 21. Concluded.
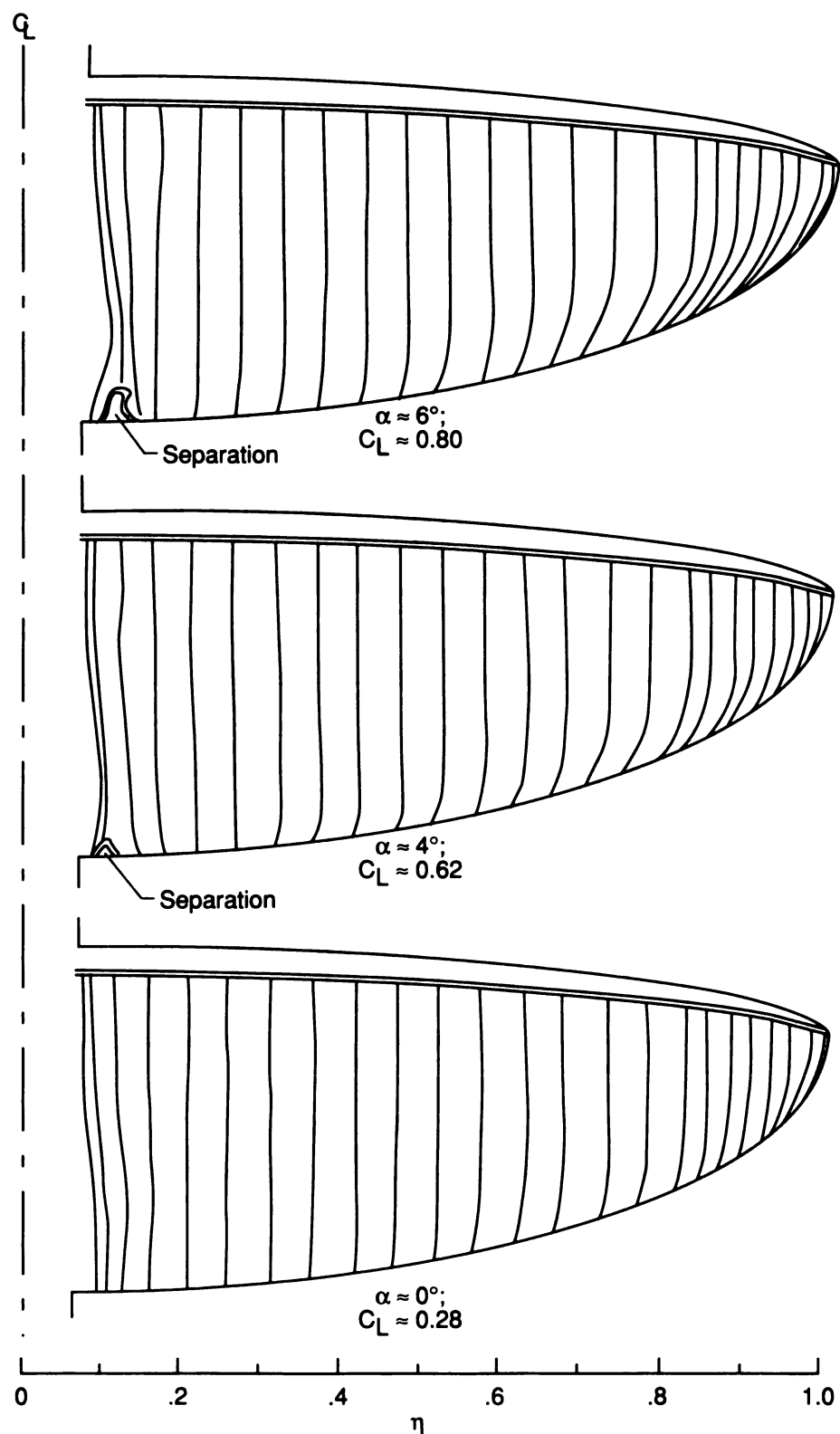
Figure 22. Sketches of oil-flow patterns on upper surface of wing A. $M_\infty = 0.5$.
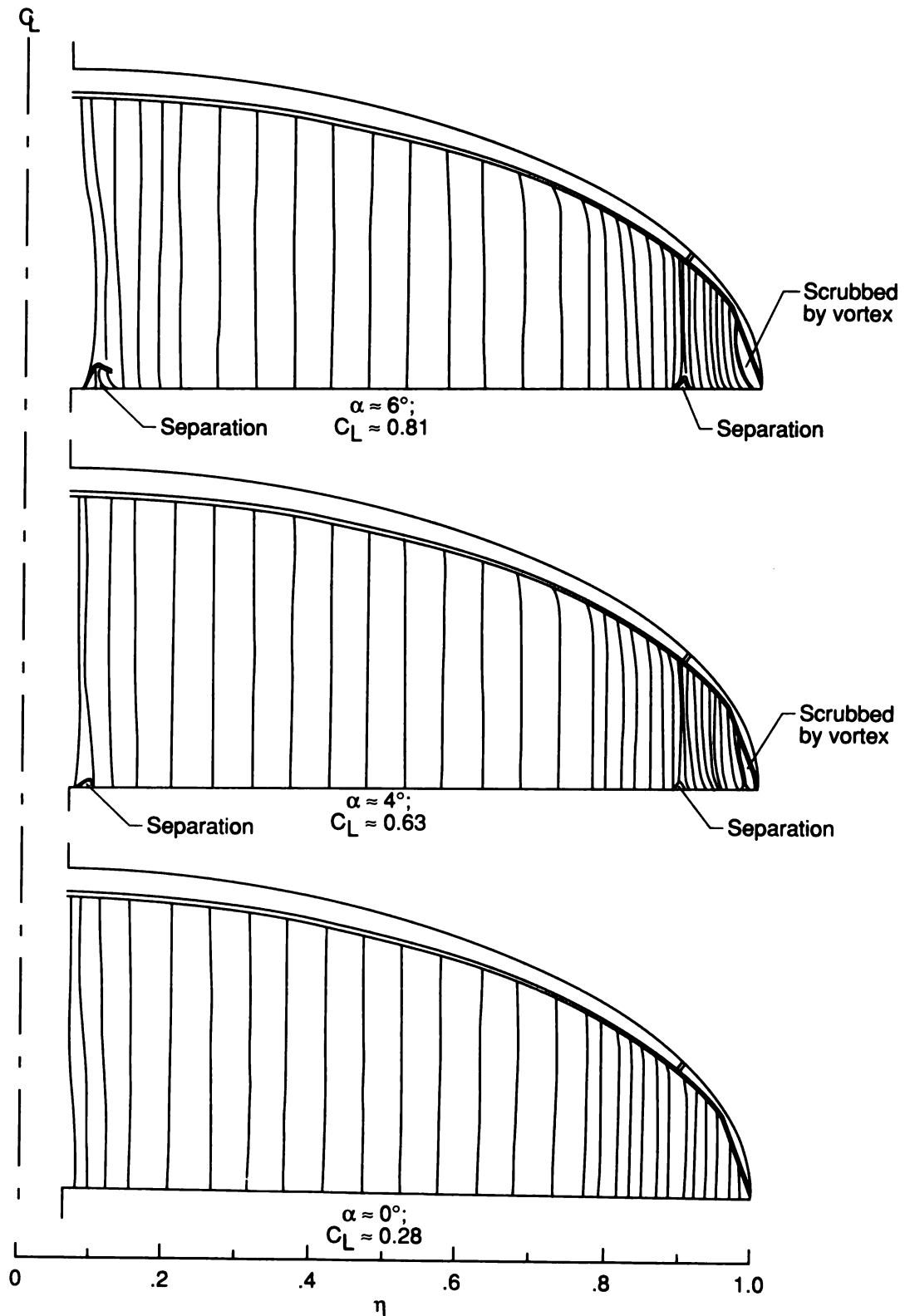
Figure 23. Sketches of oil-flow patterns on upper surface of wing B. $M_\infty = 0.5$.
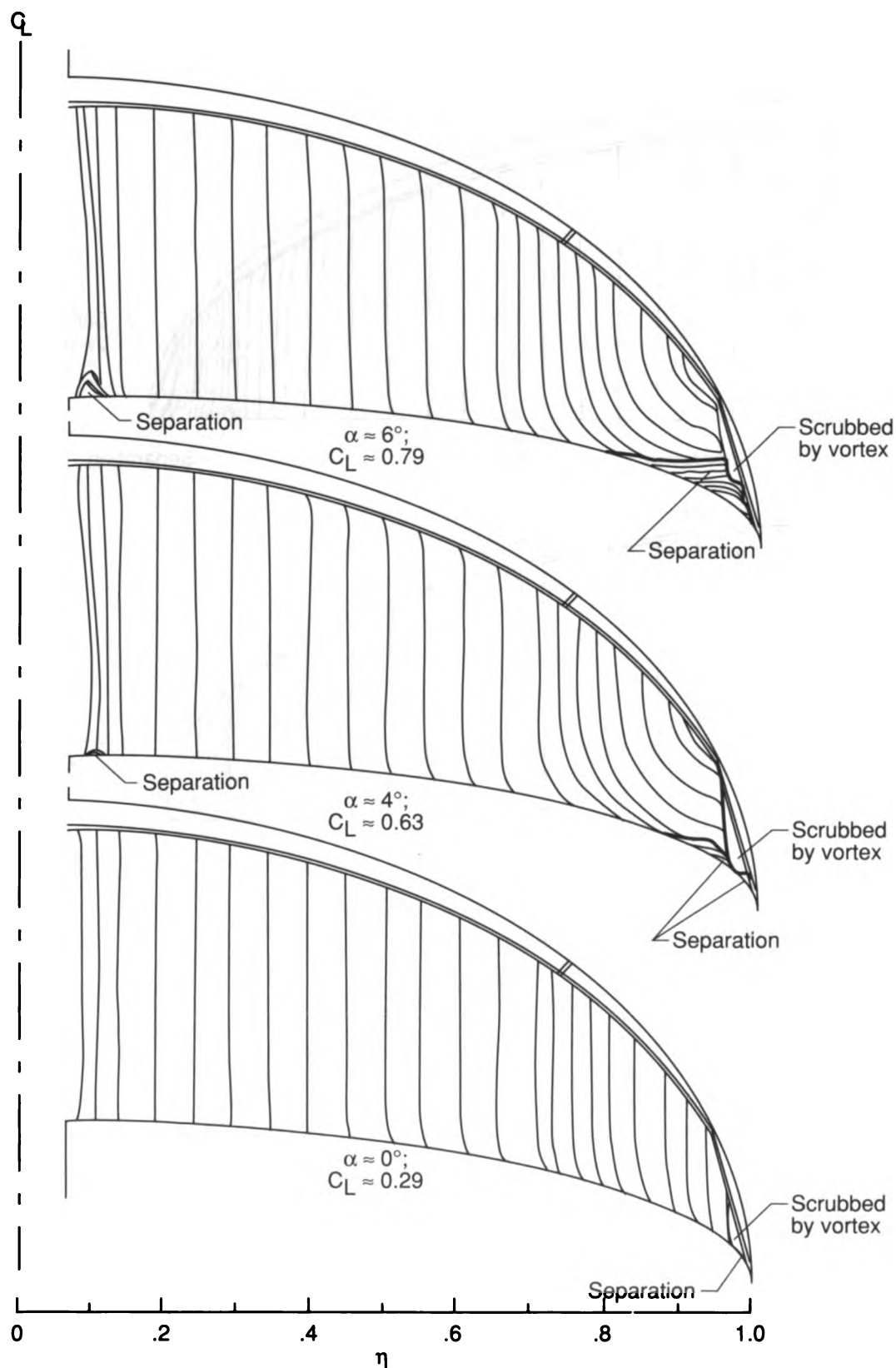
Figure 24. Sketches of oil-flow patterns on upper surface of wing C. $M_\infty = 0.5$.

$\alpha \approx 4°;$
$C_L \approx 0.65$

Separation

$\alpha \approx 0°;$
$C_L \approx 0.29$

Separation
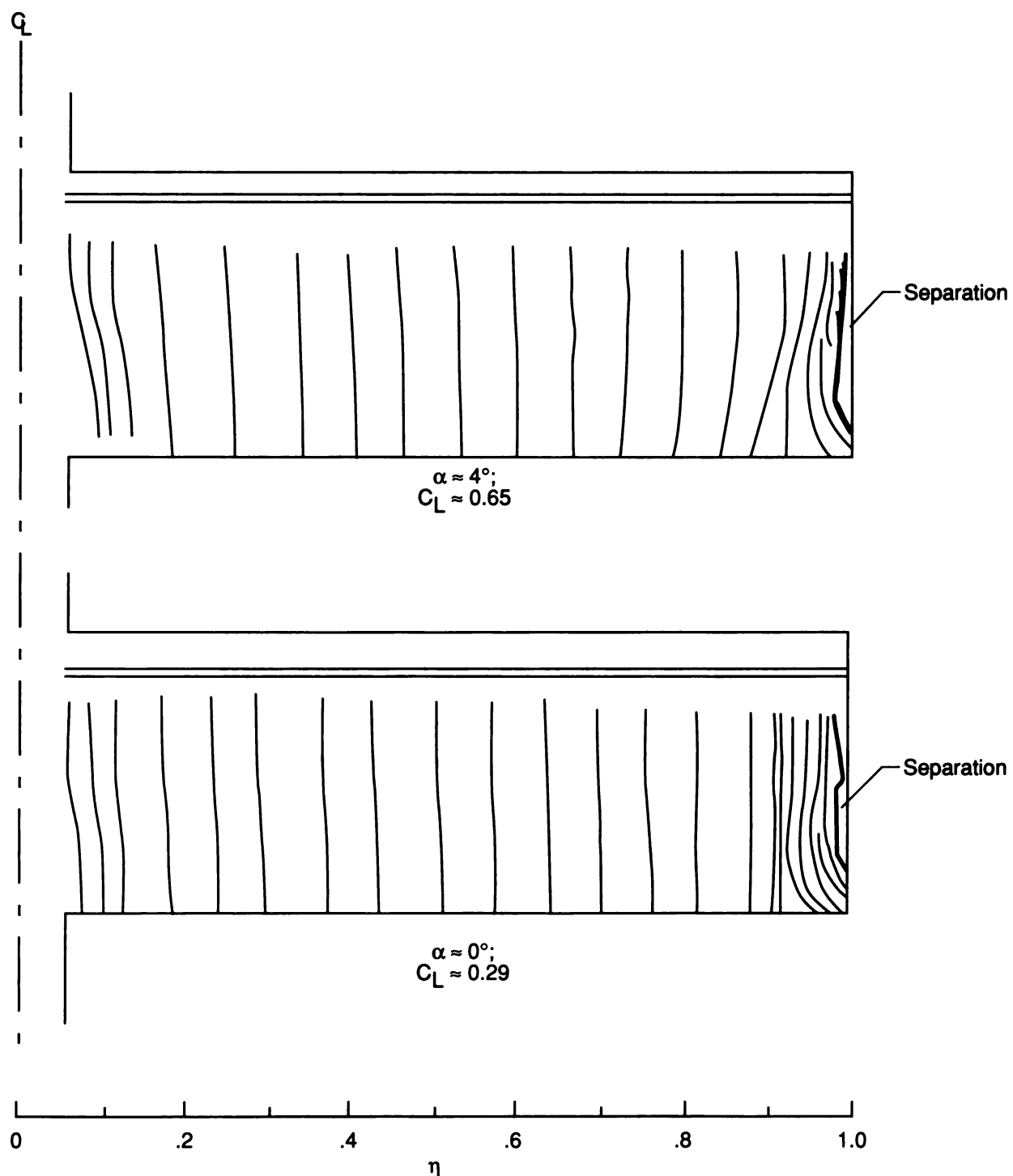
Figure 25. Sketches of oil-flow patterns on upper surface of wing D with square tips. $M_\infty = 0.5$.
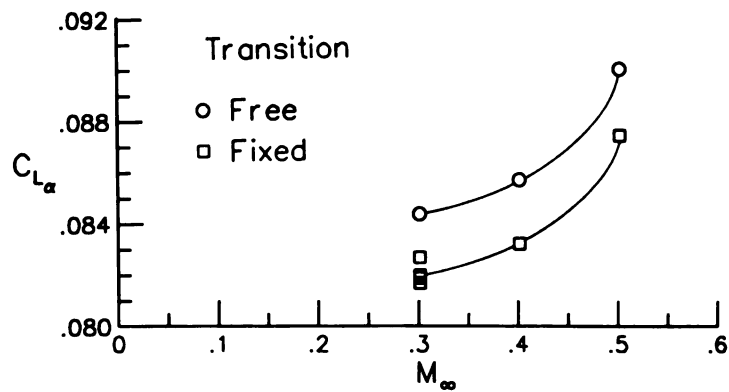
Figure 26. Effect of fixing transition on lift-curve slopes for wing A. $R_c = 2.1 \times 10^6$.
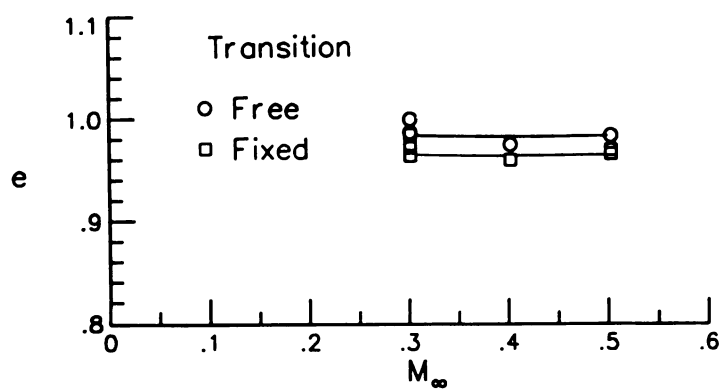
Figure 27. Effect of fixing transition on Oswald efficiency factor for wing A. $R_c = 2.1 \times 10^6$.
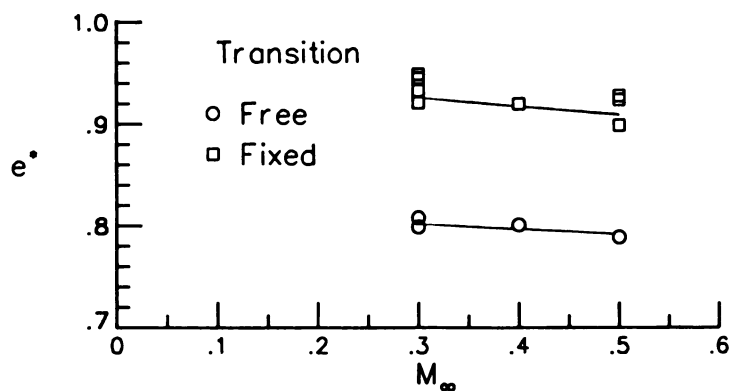
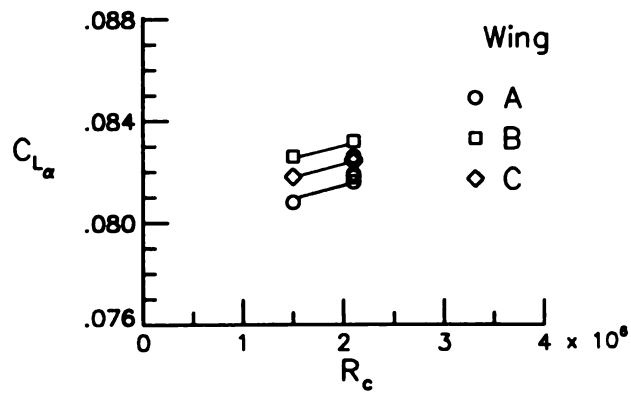Figure 28. Effect of fixing transition on cambered-wing efficiency factor for wing A. $R_c = 2.1 \times 10^6$.

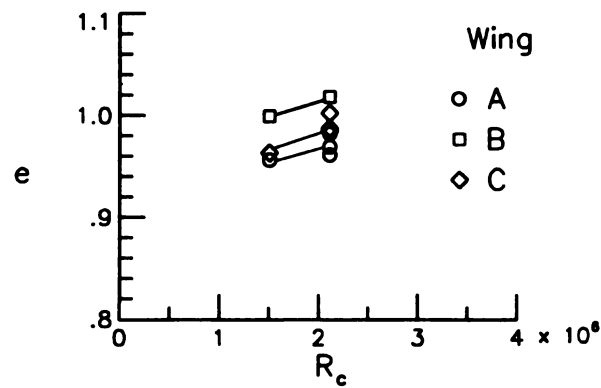Figure 29. Effect of wing planform shape on variation of lift-curve slope with Reynolds number. $M_\infty = 0.3$.

Figure 30. Effect of wing planform shape on variation of Oswald efficiency factor with Reynolds number. $M_\infty = 0.3$.
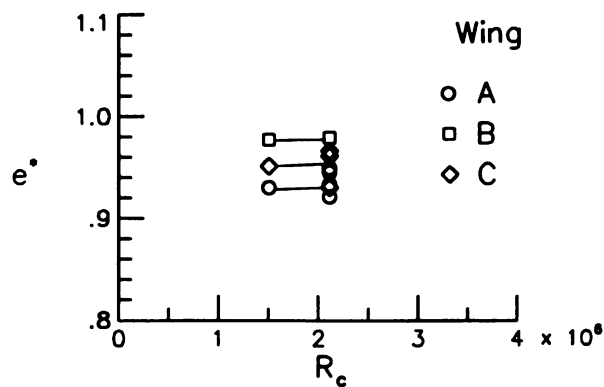

Figure 31. Effect of wing planform shape on variation of cambered-wing efficiency factor with Reynolds number. $M_\infty = 0.3$.
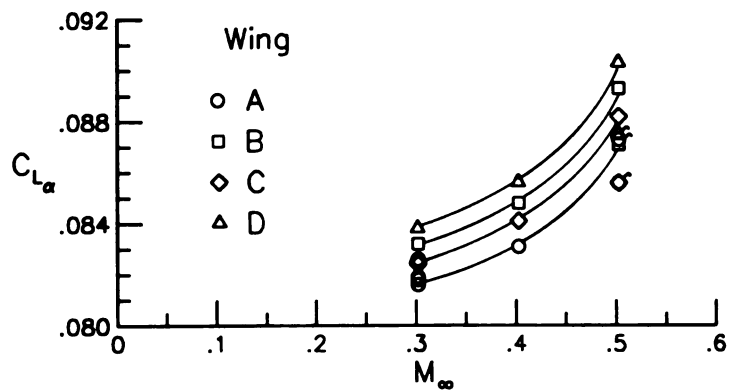
Figure 32. Effect of wing planform shape on variation of lift-curve slope with Mach number. Flagged symbols indicate data from the 7 × 10 HST.
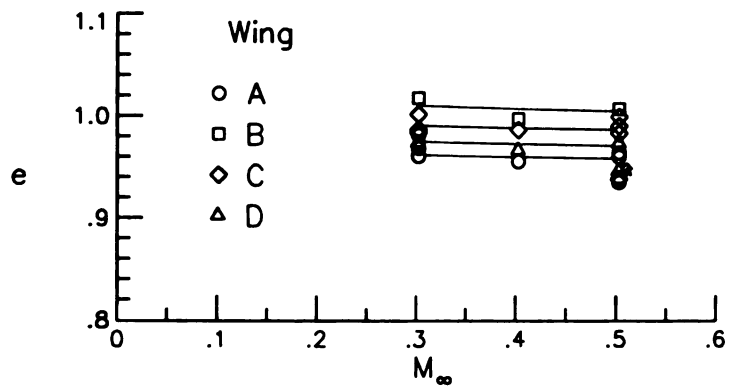

Figure 33. Effect of wing planform shape on variation of Oswald efficiency factor with Mach number. Flagged symbols indicate data from the 7 × 10 HST.
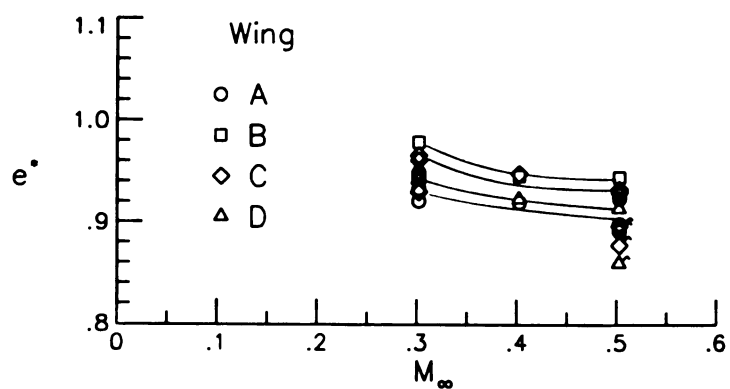

Figure 34. Effect of wing planform shape on variation of cambered-wing efficiency factor with Mach number. Flagged symbols indicate data from the 7 × 10 HST.

REPORT DOCUMENTATION PAGE

Public reporting burden for this collection of information is estimated to average 1 hour per response, including the time for reviewing instructions, searching existing data sources, gathering and maintaining the data needed, and completing and reviewing the collection of information. Send comments regarding this burden estimate or any other aspect of this collection of information, including suggestions for reducing this burden, to Washington Headquarters Services, Directorate for Information Operations and Reports, 1215 Jefferson Davis Highway, Suite 1204, Arlington, VA 22202-4302, and to the Office of Management and Budget, Paperwork Reduction Project (0704-0188), Washington, DC 20503.

1. AGENCY USE ONLY(Leave blank)	2. REPORT DATE October 1993	3. REPORT TYPE AND DATES COVERED Technical Paper

4. TITLE AND SUBTITLE
Wind-Tunnel Investigation of Aerodynamic Efficiency of Three Planar Elliptical Wings With Curvature of Quarter-Chord Line

5. FUNDING NUMBERS
WU 505-59-10-03

6. AUTHOR(S)
Raymond E. Mineck and Paul M. H. W. Vijgen

7. PERFORMING ORGANIZATION NAME(S) AND ADDRESS(ES)
NASA Langley Research Center
Hampton, VA 23681-0001

8. PERFORMING ORGANIZATION REPORT NUMBER
L-17185

9. SPONSORING/MONITORING AGENCY NAME(S) AND ADDRESS(ES)
National Aeronautics and Space Administration
Washington, DC 20546-0001

10. SPONSORING/MONITORING AGENCY REPORT NUMBER
NASA TP-3359

11. SUPPLEMENTARY NOTES
Mineck: Langley Research Center, Hampton, VA; Vijgen: High Technology Corporation, Hampton, VA.

12a. DISTRIBUTION/AVAILABILITY STATEMENT

Unclassified–Unlimited

Subject Categories 02 and 34

12b. DISTRIBUTION CODE

13. ABSTRACT (Maximum 200 words)

Three planar, untwisted wings with the same elliptical chord distribution but with different curvatures of the quarter-chord line were tested in the Langley 8-Foot Transonic Pressure Tunnel (8-Ft TPT) and the Langley 7- by 10-Foot High-Speed Tunnel (7 × 10 HST). A fourth wing with a rectangular planform and the same projected area and span was also tested. Force and moment measurements from the 8-Ft TPT tests are presented for Mach numbers from 0.3 to 0.5 and angles of attack from $-4°$ to $7°$. Sketches of the oil-flow patterns on the upper surfaces of the wings and some force and moment measurements from the 7 × 10 HST tests are presented at a Mach number of 0.5. Increasing the curvature of the quarter-chord line makes the angle of zero lift more negative but has little effect on the drag coefficient at zero lift. The changes in lift-curve slope and in the Oswald efficiency factor with the change in curvature of the quarter-chord line (wingtip location) indicate that the elliptical wing with the unswept quarter-chord line has the lowest lifting efficiency and the elliptical wing with the unswept trailing edge has the highest lifting efficiency; the crescent-shaped-planform wing has an efficiency in between.

14. SUBJECT TERMS
Elliptical wings; Induced drag; Laminar flow airfoil; Transition

15. NUMBER OF PAGES
79

16. PRICE CODE
A05

17. SECURITY CLASSIFICATION OF REPORT Unclassified	18. SECURITY CLASSIFICATION OF THIS PAGE Unclassified	19. SECURITY CLASSIFICATION OF ABSTRACT	20. LIMITATION OF ABSTRACT

National Aeronautics and
Space Administration
Code JTT
Washington, D.C.
20546-0001

NASA